РОССИЙСКИЙ ГОСУДАРСТВЕННЫЙ ПЕДАГОГИЧЕСКИЙ УНИВЕРСИТЕТ им. А. И. ГЕРЦЕНА
HERZEN STATE PEDAGOGICAL UNIVERSITY of RUSSIA

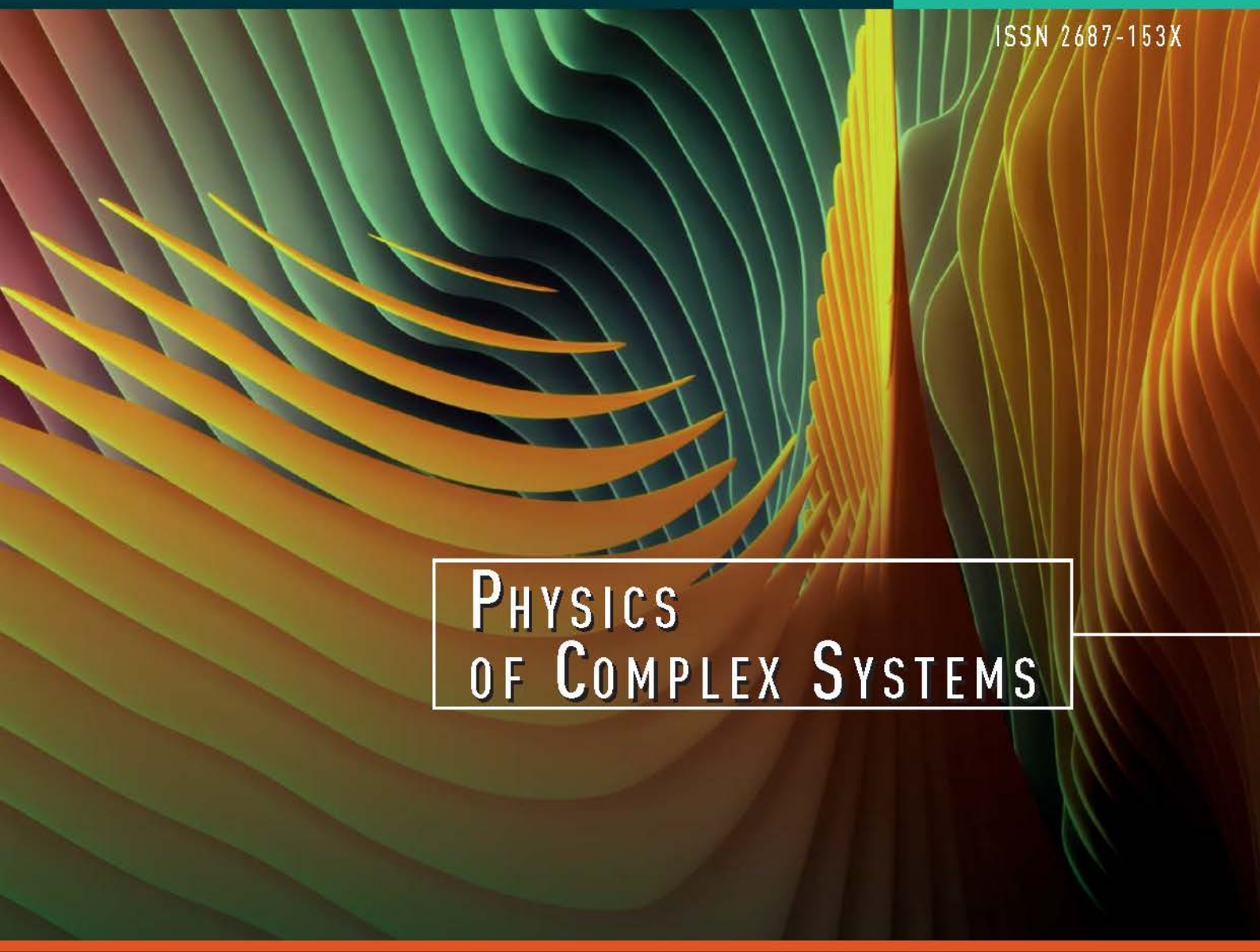

ISSN 2687-153X

Physics of Complex Systems

Т. 5 № 3 2024

Vol. 5 No. 3 2024

Herzen State Pedagogical University of Russia

ISSN 2687-153X (online)
physcomsys.ru
https://www.doi.org/10.33910/2687-153X-2024-5-3
2024. Vol. 5, no. 3

PHYSICS OF COMPLEX SYSTEMS

Mass Media Registration Certificate El No. FS77-77889, issued by Roskomnadzor on 10 February 2020
Peer-reviewed journal
Open Access
Published since 2020
4 issues per year

Publishing house of Herzen State Pedagogical University of Russia
48 Moika Emb., Saint Petersburg 191186, Russia
E-mail: izdat@herzen.spb.ru
Phone: +7 (812) 312-17-41

Data size 9,50 Mbyte
Published at 15.10.2024

Editor of the English text *K. Yu. Rybachuk*
Corrector *M. L. Kurakina*
Cover design by *O. V. Rudneva*
Layout by *D. V. Romanova*

CONTENTS

Condensed Matter Physics.
Physics of thin films.
Surfaces and interfaces

UDC 621.762

EDN JDEKGG
https://www.doi.org/10.33910/2687-153X-2024-5-3-111-123

Research of the protective ability of coatings on steel powder against atmospheric corrosion

I. V. Shakirov ✉[1], A. S. Zhukov [1], V. V. Bobyr' [1], P. A. Kuznetsov [1]

[1] NRC 'Kurchatov Institute' — CRISM 'Prometey', 49 Shpalernaya Str., Saint Petersburg 191015, Russia

Authors

Ivan V. Shakirov, ORCID: 0000-0002-7336-8792, e-mail: i.v.shakirov@yandex.ru

Anton S. Zhukov, ORCID: 0000-0001-6713-1943, e-mail: jouan@mail.ru

Vitaliy V. Bobyr', ORCID: 0000-0002-3343-4791, e-mail: bobyr.vv@gmail.com

Pavel A. Kuznetsov, ORCID: 0000-0002-8330-5365, e-mail: kspavel@mail.ru

For citation: Shakirov, I. V., Zhukov, A. S., Bobyr', V. V., Kuznetsov, P. A. (2024) Research of the protective ability of coatings on steel powder against atmospheric corrosion. *Physics of Complex Systems*, 5 (3), 111–123. https://www.doi.org/10.33910/2687-153X-2024-5-3-111-123 EDN JDEKGG

Received 5 July 2024; reviewed 19 July 2024; accepted 19 July 2024.

Funding: This work was supported by the grant of Russian Scientific Fund, project No. 21-73-30019.

Abstract. Storing the main material for additive technologies, i. e. metal powder compositions made from steels and alloys with low corrosion resistance, is a challenge. We studied the protective ability of coatings applied by chemical heat treatment (CHT) to the surface of a steel powder, which has low resistance against atmospheric corrosion. Long-term two-year tests of powder samples with various coating compositions were carried out at natural atmospheric humidity and ambient temperature in the Northwestern Federal District of the Russian Federation. The chemical composition of the samples was evaluated before and after the test. The chemical composition and morphology of the particles were determined by electron microprobe (EMP) using a scanning electron microscope (SEM). It is shown that coatings applied by the CHT method do not create continuous protection and accelerate corrosion processes in comparison with the heat-treated powder of the initial steel.

Keywords: additive technologies, laser powder bed fusion, direct metal deposition, metal powder compositions, corrosion protection, chemical heat treatment, iodine transport method

Introduction

Additive manufacturing uses metal powders combined into common metal powder compositions (MPCs). Storing MPC steels and alloys is associated with problems due to low corrosion resistance and high chemical activity, which, during the storage of powders, can lead to corrosion damage, reducing the properties of the final products.

There is a technological problem associated with the storage of MPCs, in which partial oxidation of the surface of the powders occurs upon contact with atmospheric air of natural humidity. Corrosion damage to powder particles during production involving additive technologies is contaminated with oxides and other non-metallic inclusions, greatly deteriorating mechanical properties, especially impact strength. As a result of corrosion, the flowability of powders also decreases, meaning degradation of the main technological characteristics of the printing powder — something that is especially important for direct metal deposition (DMD) technology.

Protection of metal powders from corrosion is one of the most important practical problems in powder metallurgy and additive technologies. Due to the high dispersion and chemical activity of powdered metals, corrosion processes occur on them more intensely than on compact metals. In this case, the methods known to protect solid metals from corrosion are either not productive enough or change some properties of the metal powder.

These problems may be solved by modifying the surface of metal powders with various coatings, creating powders of the 'core-shell' type.

Surface modification can both provide protection against corrosion and/or improve other properties of the powder: for example, increase the absorption coefficient of laser radiation, which will reduce the laser power or increase the speed of 3D printing. The cladding of the surface of powder particles creates a uniform distribution of the applied elements in the resulting sample during laser synthesis, without significantly changing the chemical composition of the initial alloy.

One of the possible ways to expand the characteristics of available industrial metal powders for powder metallurgy and additive manufacturing is their surface alloying by chemical heat treatment (CHT) (Borisenok et al. 1981; Lakhtin, Arzamasov 1985; Lobanov et al. 2014; Popov 1962; Solntsev 2009; Xiaowei et al. 2005).

Previous studies have focused on the application of coatings to powder materials using iodine transport and its prospects in terms of diffusion saturation of steel and alloys (Bogdanov 2011a; 2011b; 2012a; 2012b; 2016; Khristyuk et al. 2015). Chromium coatings have been obtained on the surface of powder particles from pure iron, carbon and alloy steels (Bogdanov 2011a; 2011b; 2012a; 2012b).

The most suitable method of obtaining functional coatings on powders, especially micron and nanoscale ones, is deposition from the gas phase, including gas transport (Bogdanov 2016).

To protect the surface of low-alloy steel, it is advisable to use metals with high corrosion resistance which are suitable for application using the chemical treatment method, such as Cr, Ti or Al. To ensure high anticorrosion properties of the surface, a continuous and homogeneous coating layer should be obtained (Lobanov et al. 2014; Solntsev 2009).

Results show that chromium surface treatment improves the corrosion resistance of stainless steel due to the high concentration of chromium in the diffuse coating layer (Lee et al. 2009). Iodine (Bogdanov 2011b) or ammonium chloride has been proposed as a transport agent for a wide range of transported metals.

Corrosion tests of metal powders in various environments have shown that moisture is the decisive factor here and that corrosion processes occur exclusively at the interface between the surface of powder particles and the liquid phase. Thus, a reliable way to protect metal powders against corrosion is to block the access of moisture to the surface of the powder (Likhtman 1954).

Currently, the industry is witnessing the development of additive technologies; the use of clad powders makes it possible to obtain the necessary technological properties. Featuring prominently among them are coatings providing a high level of corrosion resistance.

The purpose of this study was to evaluate the corrosion resistance of steel powders clad with compositions based on chromium, titanium and aluminum for protection against atmospheric corrosion during storage.

Materials and methods

The basis for applying coatings using the CHT method was a steel powder of grade 45ChN2MFA (which has an average composition of 0.42–0.5% C, 0.8–1.15% Cr, 1.3–1.8% Ni, 0.2–0.3% Mo, 0.1–0.18% V), obtained using a HERMIGA 75/3 IV type melt spraying equipment. The resulting steel powder was prepared by sieving the required dispersed composition using LPBF technology (20–63 microns). A completely martensitic structure of powder particles was formed due to high cooling rates during the spraying of steel (Fig. 1a). The morphology of the particles was predominantly spherical, but there was a significant proportion of irregularly shaped particles and particles with surface defects (Fig. 1b).

The microrelief of the surface of powder particles was due to the morphology of the formed structure. A more developed rough surface was created, which may contribute to better adhesion of the coating composition.

The chemical composition from the surface of the powder particles obtained via EMP with indication of the corresponding spectra (Fig. 1) in comparison with rolling is presented in Table 1.

 https://www.doi.org/10.33910/2687-153X-2024-5-3-111-123

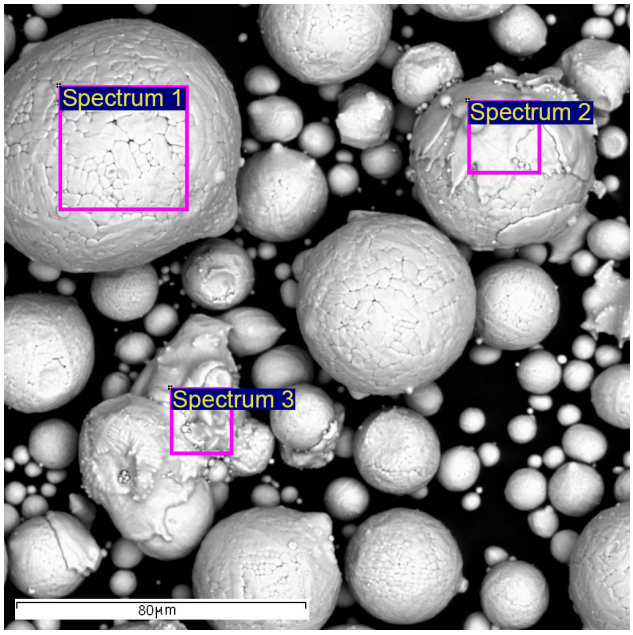

Fig. 1. Particle structure of the initial steel powder — morphology of the powder particles

Table 1. Chemical composition

Sample	Al	Si	S	V	Cr	Mn	Fe	Ni
Rolling	0.13	0.43	–	0.18	1.00	0.68	95.48	1.67
Spectrum 1	0.21	0.37	0.07	–	1.07	0.68	96.07	1.53
Spectrum 2	–	0.32	0.05	–	1.08	0.80	96.26	1.49
Spectrum 3	0.25	0.24	–	0.24	1.04	0.69	96.26	1.27

Cr, Ti and Al were chosen as cladding metals for the 45ChN2MFA steel powder based on their inherent corrosion resistance and the possibility of application by the CHT method. The compositions and parameters for CHT by the gas transport method using iodine and ammonium chloride are shown in Table 2. The optimal CHT modes were selected in order to prevent sintering of the powder. Also, to compare the corrosion resistance of the uncoated 45ChN2MFA steel powder, a powder sample was prepared after heat treatment (HT) in a vacuum furnace at a temperature of 700 °C and a holding time of 4 hours, which corresponds to the thermal cycle at CHT.

Table 2. Receiving modes

Composition of the cladding layer	Element content, mass %	Precipitation method	Temperature, °C	Time, h
Cr	5	I2	600	3
Cr	1	NH4Cl	650	3
Ti/Cr	each 0,5	NH4Cl	650	3
Ti	0,5	NH4Cl	650	6
Al	1	NH4Cl	650	6

The powder compositions were kept in a chamber protecting them from direct precipitation, but under conditions of natural atmospheric humidity and ambient temperature of the Northwestern Federal District of the Russian Federation. The samples of the powder compositions were distributed over the surface with a layer with a thickness of no more than 1 mm, which ensured the contact of the free surface of the powders with the atmosphere. The duration of exposure was two years, with the samples withdrawn for intermediate analysis after the first year of exposure. Thus, this made it possible to assess the impact of atmospheric conditions of all seasons over two years in this region.

The main criterion for assessing the anticorrosion properties of coatings was a comparison of the chemical composition of samples before and after the test. Based on the specifics of coating the surface of powder particles by the CHT-method, the chemical composition was determined by electron microprobe (EMP) using a scanning electron microscope (SEM). Due to the unevenness of the cladding coatings and the formation of locally distributed chemical compounds on the surface of the particles caused by the method of gas transport using iodine and ammonium chloride, the most representative sites were selected during the research to obtain data on the chemical composition. This method allowed us to evaluate the chemical composition of the surface of powder particles, considering its morphology. The morphology of MPC particles was studied using scanning electron microscopy methods as well as energy dispersion analysis of the content of mimic elements. Powder samples were examined before and after the exposure to a corrosive environment.

The flowability of the powders was assessed using a calibrated Hall funnel in accordance with GOST 20899-98, with bulk density determined in accordance with GOST 19440-94.

Diffuse reflection spectra of steel powders were measured. The spectra were captured using an SF-56 spectrophotometer.

The content of the mass fraction of oxygen in the powder was analyzed using a LECO TC-400 gas analyzer.

Results and discussion

Deposition of the cladding metal on the surface of the powder changes the surface roughness of the particles, affecting the flowability and bulk density of the MPC, which are important for the printing process. To assess the preservation of MPC characteristics after coating, the flowability and bulk density of the powder samples were measured (see Fig. 2, 3).

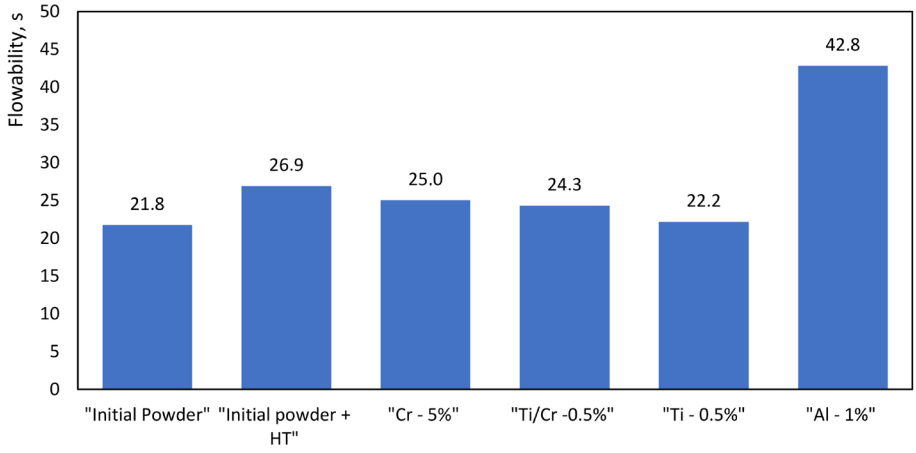

Fig. 2. Flowability of powders

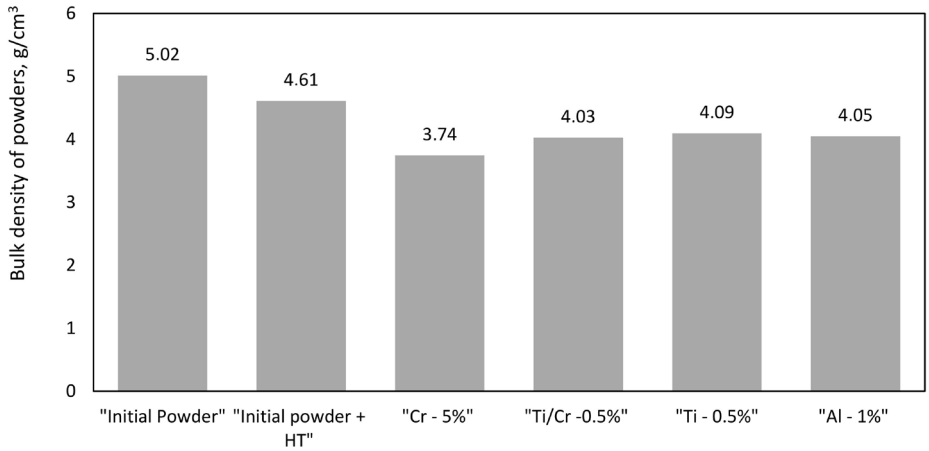

Fig. 3. Bulk density of powders

https://www.doi.org/10.33910/2687-153X-2024-5-3-111-123

The Cr–1% sample did not have flowability according to the GOST 20899-98 method; accordingly, bulk density was not determined for this sample. The Al–1% sample was characterized by a noticeable decrease in flowability in comparison with the initial powder.

After applying cladding coatings, the flowability of the powders and bulk density decreased. MPC flowability values are especially important for direct energy and material deposition, as well as for powder bed fusion equipment with the top-feed MPC. Flowability values characterize the uniformity of application of the cladding composition and the proportion of agglomerated particles during the chemical treatment process. The values of flowability and bulk density measured for clad powders (except for the Cr–1% sample), despite the decrease in the technological qualities of the MPC, satisfy the requirements of the LPBF process and can be used to create experimental samples; however, uneven coating can critically decrease corrosion protection — to a greater extent than reduction in flowability characteristics and bulk density.

The decrease in flowability and bulk density for the powder samples under study occurred in different proportions; for example, for the Al–1% sample, a strong increase in the flow time was established, while bulk density was comparable to other powder samples. This property is determined by the processes of agglomeration of powder particles during chemical treatment, which significantly affects the flow time of the powder through a calibrated funnel, while the bulk density does not decrease significantly.

The results of a qualitative visual analysis of the powder samples with different cladding depending on test duration are presented in Fig. 4.

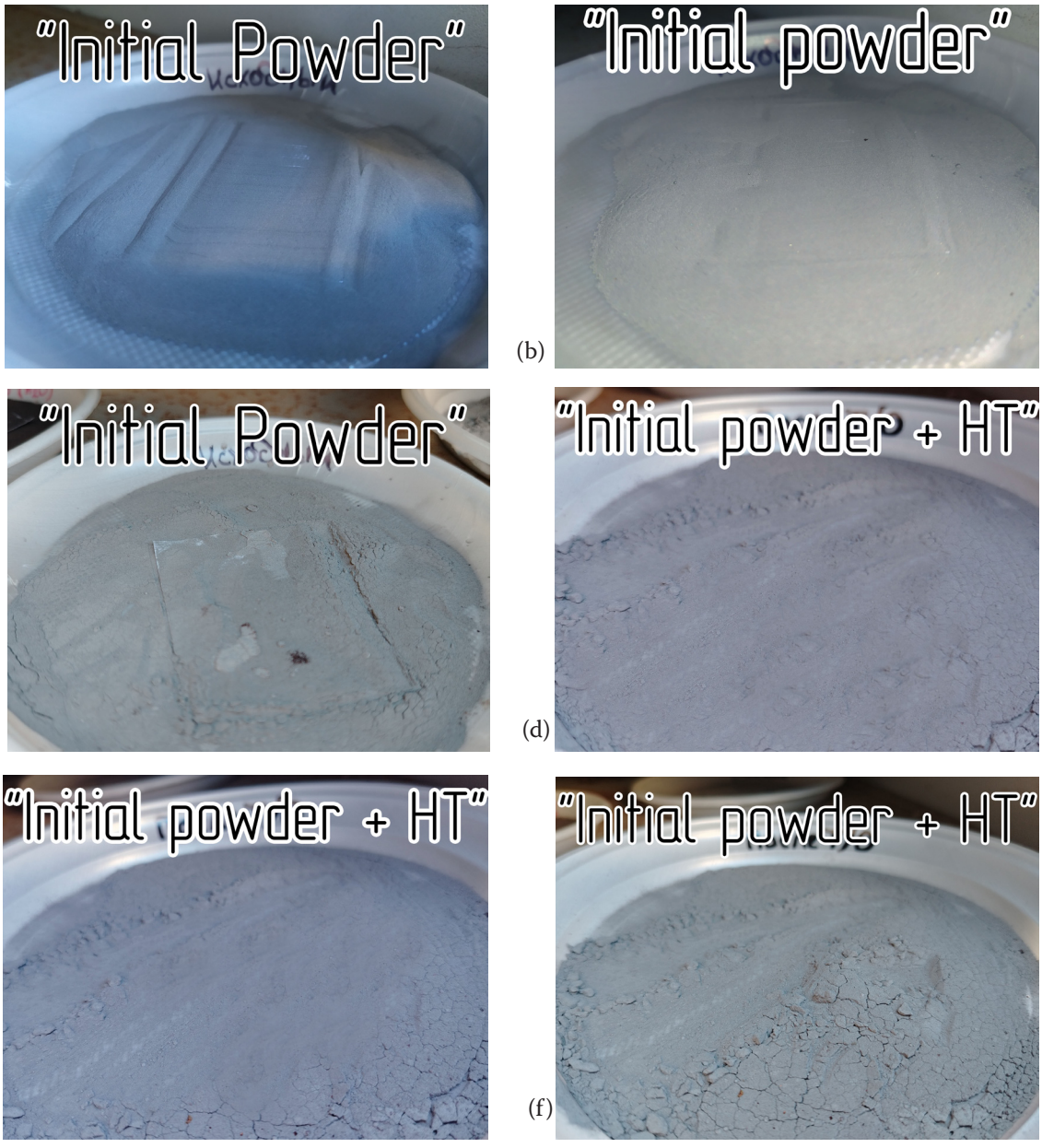

(g)

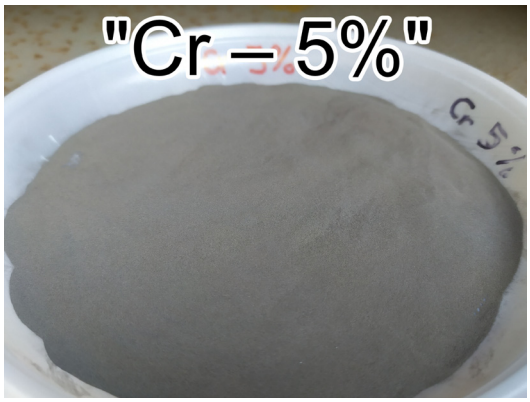

(h)

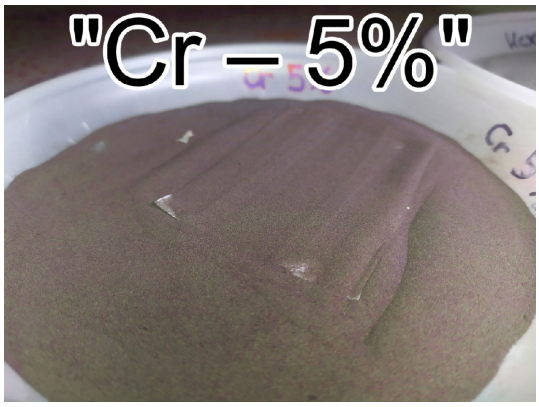

(i)

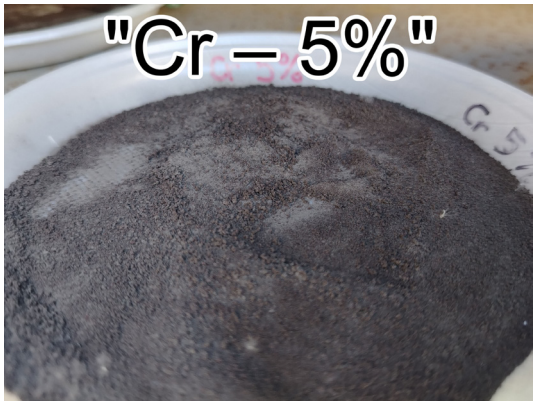

(j)

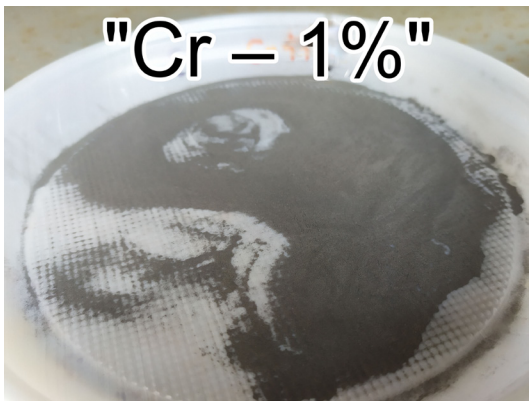

(k)

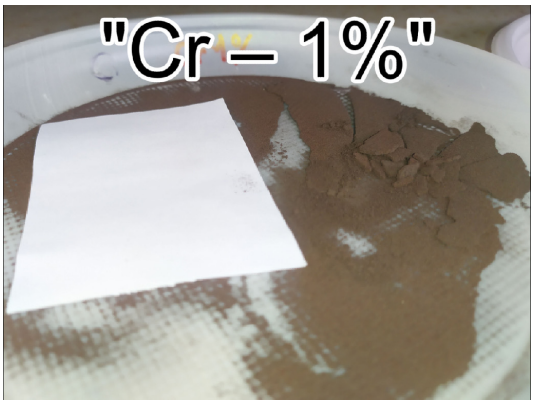

(l)

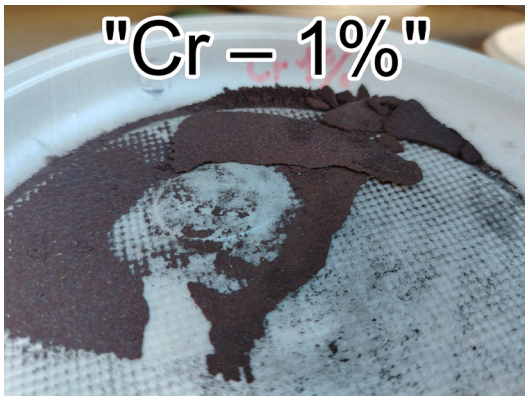

(m)

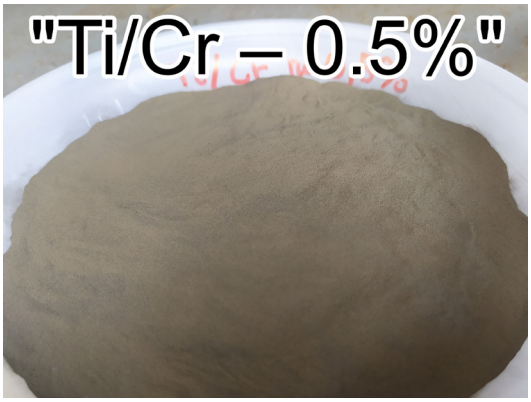

(n)

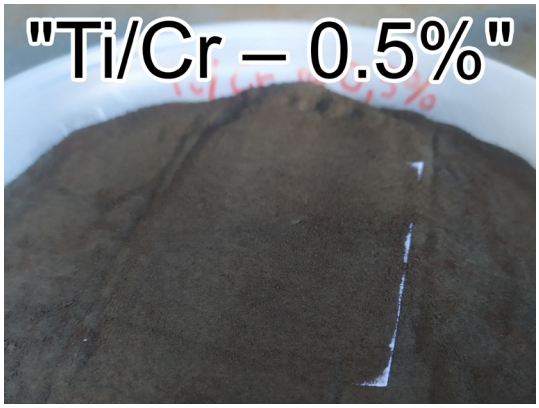

https://www.doi.org/10.33910/2687-153X-2024-5-3-111-123

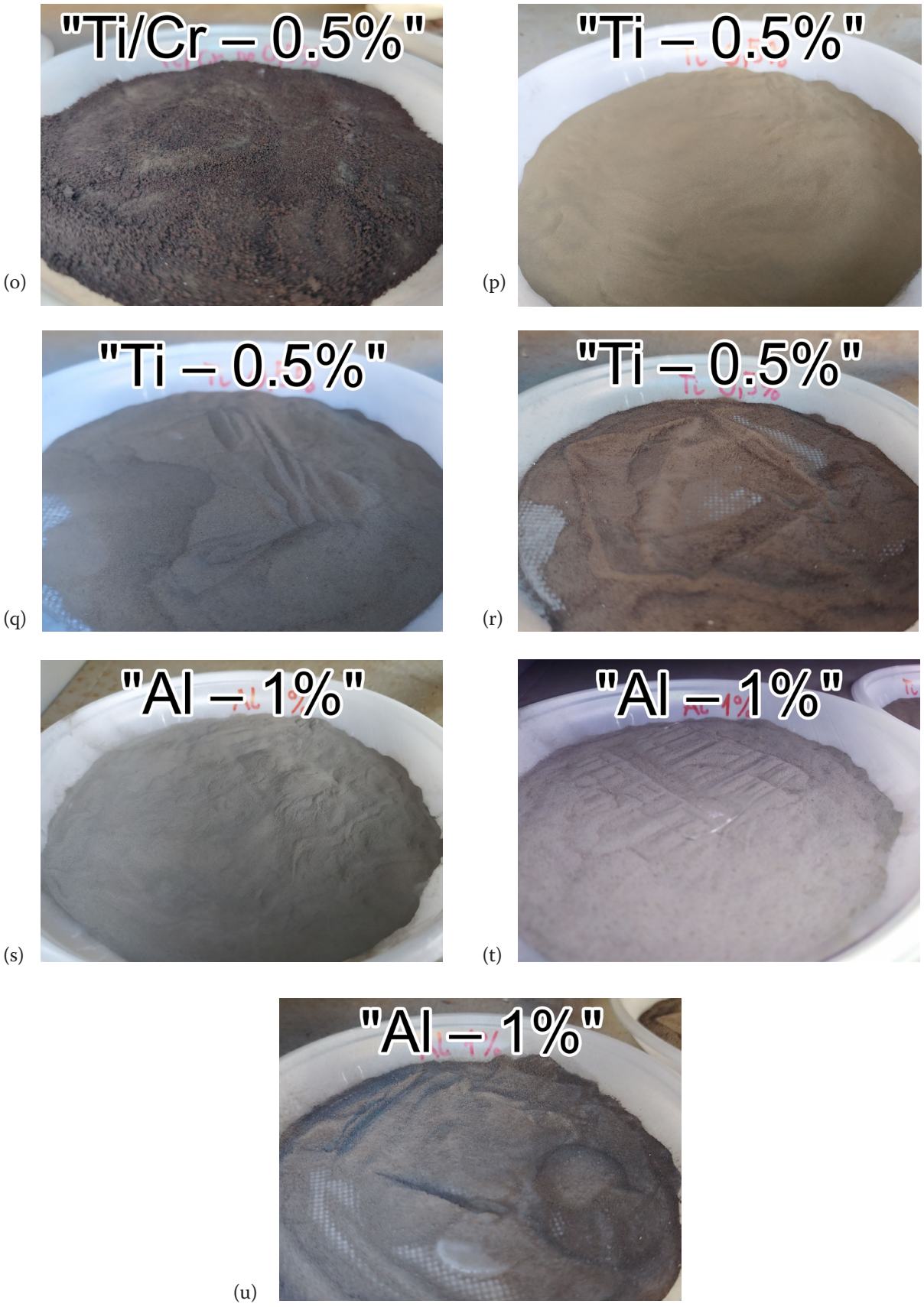

(o) (p) (q) (r) (s) (t) (u)

Fig. 4. Comparison of the appearance of powder samples depending on the test time (initial state, 1 year, 2 years): (a), (b), (c) — initial powder (minor agglomeration); (d), (e), (f) — initial powder + HT (minor agglomeration); (g), (h), (i) — Cr–5% (color change); (j), (k), (l) — Cr–1% (agglomeration, color change); (m), (n), (o) — Ti/Cr–0.5% (color change); (p), (q), (r) — Ti–0.5% (color change); (s), (t), (u) — Al–1% (color change)

The results of flowability and bulk density determined for the powder samples are consistent with their appearance. All the samples of clad powders are characterized by a color change; the powders acquire a red-brown color characteristic of iron oxide. The initial powder without heat treatment and with heat treatment did not change its color after testing. All the powders after the test are characterized by particle agglomeration to varying degrees.

Comparison of surface morphology and chemical composition of powder samples before and after weathering testing

For MPC samples SEM methods were used to obtain images of the surface of the powder particles (Fig. 5) before testing and after, following two years of exposure to natural atmospheric conditions.

(a) 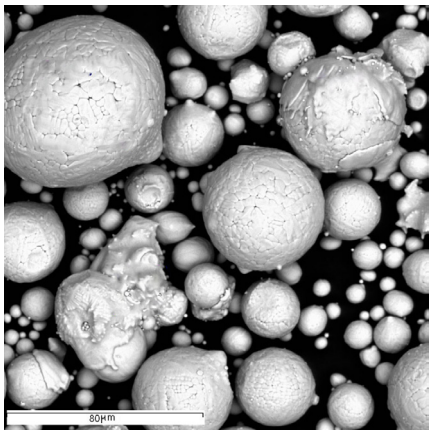

(b) 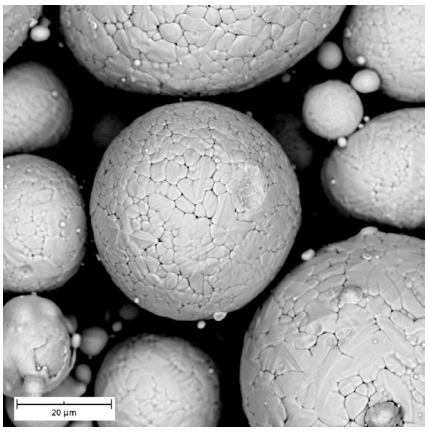

(c) 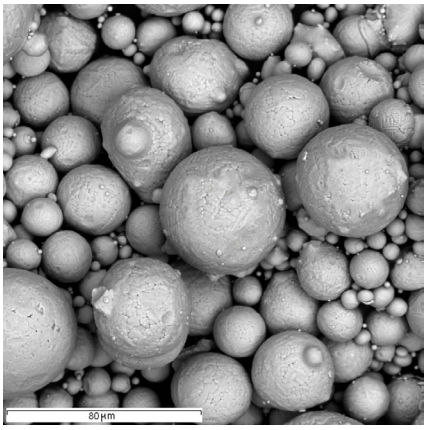

(d) 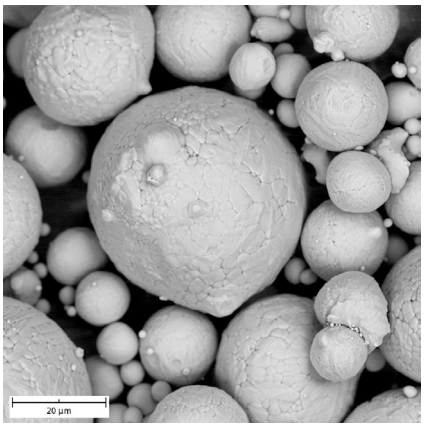

(e) 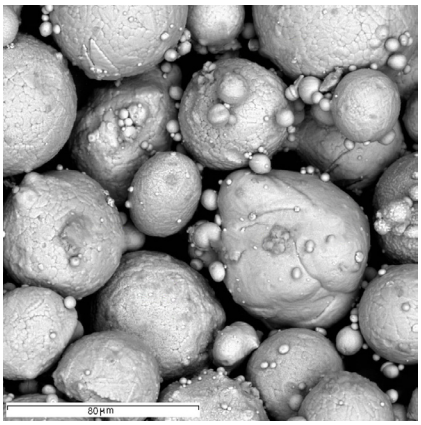

(f) 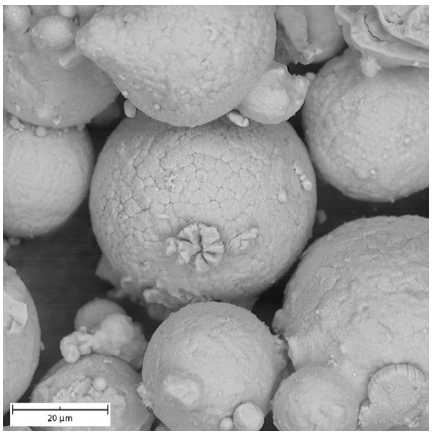

 https://www.doi.org/10.33910/2687-153X-2024-5-3-111-123

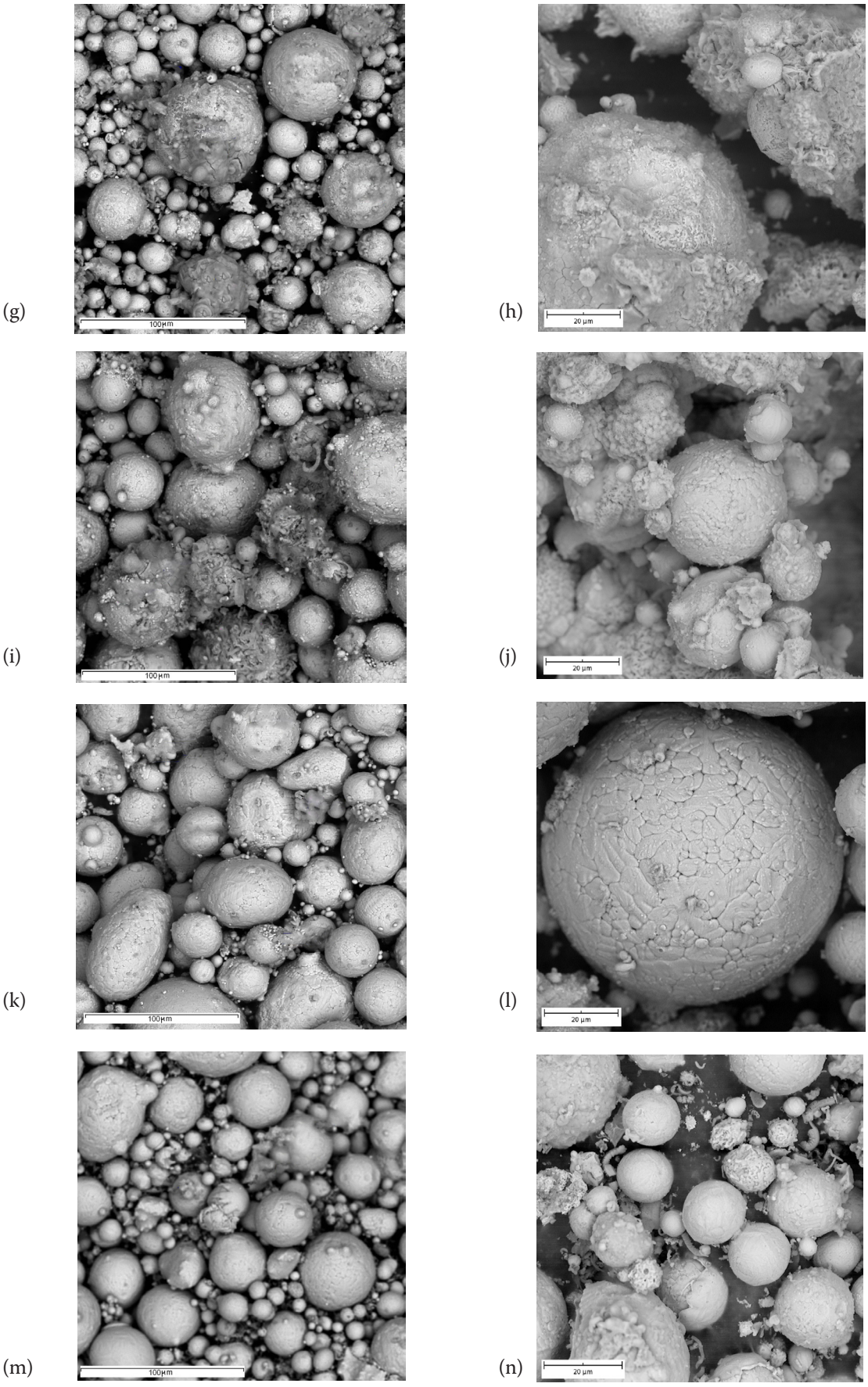

Fig. 5. Initial powder: (a) before testing, (b) after testing; initial powder + HT: (c) before testing, (d) after testing; Cr–5%: (e) before testing, (f) after testing; Cr–1%: (g) before testing, (h) after testing; Ti/Cr–0.5%: (i) before testing, (j) after testing; Ti–0.5%: (l) before testing, (m) after testing, Al–1%: (n) before testing, (o) after testing

Morphology study shows that clad powders have a layer of applied coating on their surface which is unevenly concentrated on the surface of the powder particles. Thus, no protection against corrosion is provided.

Analysis of oxygen content on the surface of the powder particles

To assess the degree of oxidation processes, the oxygen content in the powder samples was measured depending on the test time. A comparison of the oxygen concentration on the surface of the powder particles was made before testing, after 1 year and after 2 years (Fig. 6), making it possible to characterize the intensity of oxidation under test conditions.

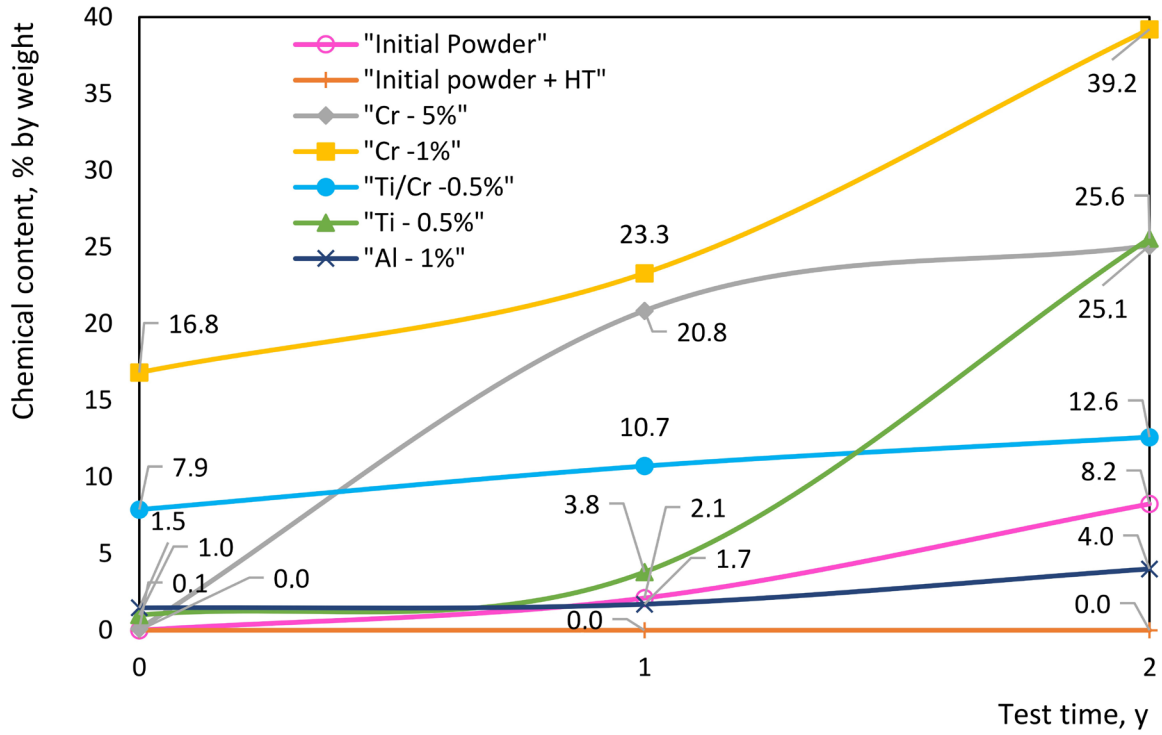

Fig. 6. Maximum oxygen content

The 45ChN2MFA steel contains a small number of alloying elements that can increase corrosion resistance. The degree of corrosion damage can be assessed by the formation of iron oxides on the surface of the powder particles.

Before testing, the powder samples were arranged in the following order according to an increase in the oxygen content: initial powder and initial powder + HT (no oxygen detected), Cr–5% (0.1% O_2), Ti–0,5% (1.0% O_2), Al–1% (1.5% O_2), Ti/Cr–0.5% (7.9 O_2) and Cr–1% (16.8% O_2). A significant mass fraction of oxygen in some of the studied powder samples before testing can characterize the quality of coating application. Apparently, when applying the compositions Ti/Cr–0.5% and Cr–1%, due to high temperatures and the presence of residual oxygen in the gas environment during chemical treatment, the powder received corrosion damage.

After testing, the samples were arranged in the following order according to an increase in the oxygen content and therefore intensity of corrosion damage: initial powder + HT (no oxygen detected), Al–1% (4.0% O_2), initial powder (8.2% O_2), Ti/Cr–0.5% (12.6% O_2), Cr–5% (25.1% O_2), Ti–0.5% (25.6% O_2) and Cr–1% (39.2% O_2). This series characterizes the ability of the powder samples under study to resist atmospheric corrosion.

Thus, the steel powder showed the best weather resistance after heat treatment; after testing, oxygen was not detected, which may apparently indicate the formation of a passivated layer on the surface of the powder particles.

For clad powders, the lowest oxygen content after testing corresponded to the Al–1% sample; the remaining powder samples were characterized by atmospheric corrosion resistance lower than that of the initial steel powder.

 https://www.doi.org/10.33910/2687-153X-2024-5-3-111-123

It is worth noting that the samples of all the clad powders did not have a continuous surface coating of the corresponding composition; thus, the CHT method was unable to create a continuous protective layer against corrosion on the surface of the powder particles, which was confirmed by visual inspection and measurement of the oxygen concentration on the surface.

Optical properties of core-shell powders on the 45ChN2MFA steel

The absorption capacity of laser radiation with a wavelength of 1,064 nm is an important characteristic for laser synthesis technologies, as it increases the laser power utilization rate during 3D printing with these MPC powders.

After coating, the MPCs increased their absorption capacity compared to the initial powder (Fig. 7), which would allow a more efficient absorption of laser radiation power during the laser synthesis process.

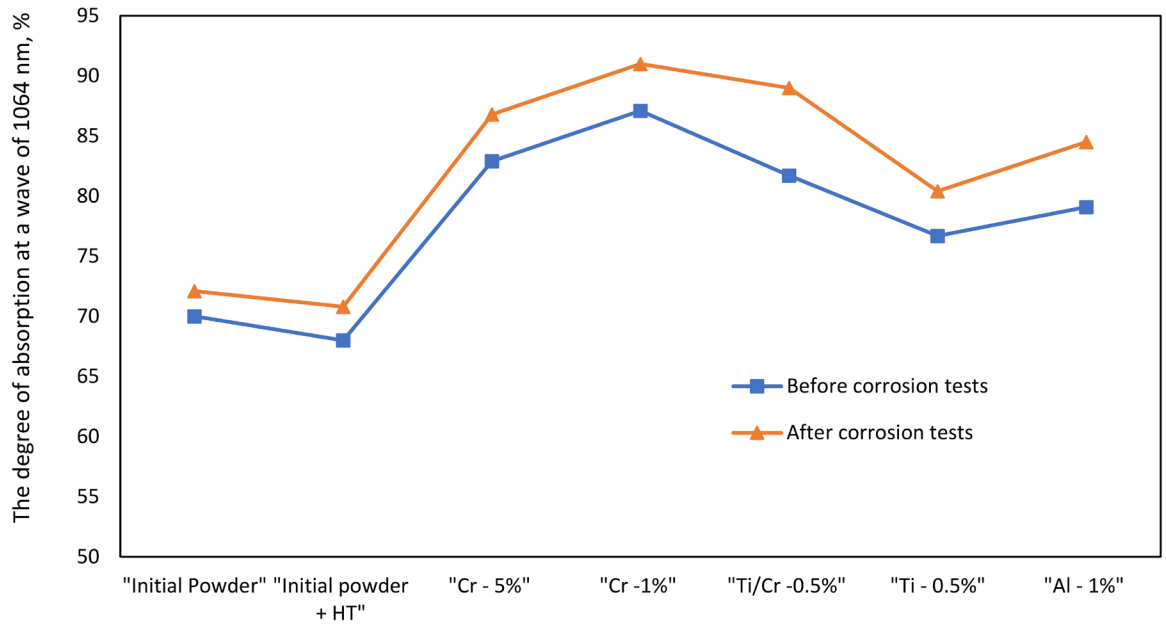

Fig. 7. Degree of absorption of clad powders before and after testing

Also, the optical properties of the clad powders indirectly characterize the formation of oxides on the surface of particles after corrosion tests. By comparing the degree of absorption of laser radiation before and after the corrosion resistance tests, we can see an increase in absorption capacity in all the powders. The absorption capacity increases with a different proportion for each composition: for clad powders this increase is more intense than for the initial and heat-treated powder.

According to test results, all clad powders have lower resistance to atmospheric corrosion than the 45ChN2MFA steel powder in the initial and heat-treated state. Of all the clad powders, the Ti/Cr–0.5%, Ti–0.5% and Al–1% samples are the most capable of resisting corrosion damage.

The high corrosion resistance of the MPC steel 45ChN2MFA in the initial and heat-treated state can be explained by the formation of a thin passivating film and slight segregation of alloying elements. The low corrosion resistance of clad powders can be explained by the uneven distribution of the cladding composition and compounds formed during the technological process of applying these coatings using the gas transport method. Thus, the surface of clad powders during chemical treatment (Khristyuk, Bogdanov 2018) experiences damage to the passivated layer obtained by spraying the initial powder due to its high chemical activity; iodine easily reacts with many metals, while their iodides are unstable compounds (Bogdanov 2012b; Rolsten 1968). Coatings do not create continuous protection and, in natural humidity, accelerate corrosion processes since the activity of metal films in the form of a coating on a substrate powder is higher than the activity of the metal powder used to obtain the coating. Films obtained by iodine transport oxidize and react with the surrounding atmosphere when the initial metal powder is still inert (Bogdanov 2012a). It is assumed that when the 45ChN2MFA steel powder is heat-treated, a thin film is created on the surface, the passivating ability of which is sufficient to provide protection against atmospheric corrosion under the test conditions.

Conclusions

1. Powders clad with various compositions have a developed porous surface with an uneven distribution of the cladding composition and compounds formed during the technological process of applying these coatings using the gas transport method. Thus, the surface of clad powders during chemical treatment experiences damage to the passivated layer obtained by spraying the initial powder or its heat treatment. The coatings do not create continuous protection and, in an atmosphere of natural humidity, accelerate corrosion processes.

2. Powders in the initial and heat-treated state during the production process — spraying the melt and subsequent heat treatment in a vacuum furnace — acquire a thin passivated layer on the surface of the particles, which is quite effective against atmospheric corrosion and does not disturb the shape of the particles.

3. After cladding, MPCs have better energy efficiency during laser melting due to a larger proportion of laser radiation absorbed by the powder.

4. Cladding of powder materials for additive technologies with various elements can be used for microalloying finished MPCs in order to change the chemical composition or uniform distribution of alloying elements prone to segregation.

Conflict of Interest

The authors declare that there is no conflict of interest, either existing or potential.

Author Contributions

All the authors discussed the final work and took part in writing the article.

References

Bogdanov, S. P. (2011a) Polucheniye pokrytij na poroshkakh metodom jodnogo transporta [Preparation of coatings on powders by iodine transport method]. *Fizika i khimiya stekla*, 37 (2), 229–237. (In Russian)

Bogdanov, S. P. (2011b) Preparation of coating on powders by the iodine transport method. *Glass Physics and Chemistry*, 37 (2), 172–178. https://doi.org/10.1134/S1087659611020040 (In English)

Bogdanov, S. P. (2012a) Jodotransportnyj metod polucheniya pokrytij na poroshkakh [Iodine transport method for producing coatings on powders]. *Izvestiya Sankt-Peterburgskogo gosudarstvennogo tekhnologicheskogo instituta (Tekhnicheskogo universiteta) — Bulletin of the Saint Petersburg State Institute of Technology (Technical University)*, 16 (42), 24–28. (In Russian)

Bogdanov, S. P. (2012b) Khimicheskaya aktivnost' pokrytij, poluchennykh metodom jodotransporta [Chemical activity of coatings obtained by the iodine transport method]. *Fizika i khimiya stekla*, 38 (6), 750–754. (In Russian)

Bogdanov, S. P. (2016) Poluchenie funktsional'nykh pokrytij metodom jodnogo transporta [Production of functional coatings by the iodine transport method]. In: *Innovatsionnyye materialy i tekhnologii v dizajne: Materialy II Vserossijskoj nauchno-tekhnicheskoj konferentsii (s uchastiem molodykh uchenykh) [Innvative materials and technologies in design: Proceedings of the II All-Russian scientific and technical conference (with the participation of young scientists)]*. Saint Petersburg: Saint Petersburg State University of Film and Television Publ., pp. 21–27. (In Russian)

Borisenok, G. V., Vasiliev, L. A., Voroshnin, L. G. et al. (1981) *Khimiko-termicheskaya obrabotka metallov i splavov: Spravochnik [Chemical-thermal processing of metals and alloys: A reference book]*. Moscow: Metallurgy Publ., 424 p. (In Russian)

Khristyuk, N. A., Bogdanov, S. P. (2018) Fazovye prevrashcheniya v khromsoderzhashchikh pokrytiyakh na stalyakh, poluchennykh metodom yodnogo transporta [Phase transformations in chromium-containing coatings on steels obtained by the iodine transport method]. In: *Aktual'nye problemy fizicheskogo metallovedeniya stalej i splavov: Materialy XXIV Ural'skoj shkoly metallovedov-termistov [Current problems of physical metal science of steels and alloys: Proceedings of the XXIV Ural school of metalurgists and thermists]*. Magnitogorsk: Nosov Magnitogorck State Technical University Publ., pp. 177–179. (In Russian)

Khristyuk, N. A., Bogdanov, S. P., Sychev, M. M. (2015) Sovremennye sposoby polucheniya khromsoderzhashchikh pokrytij na stalyakh gazotransportnymi metodami [Actual methods of preparing of the chromium-containing coatings on steel by means of gas transportation method]. *Izvestiya Sankt-Peterburgskogo gosudarstvennogo tekhnologicheskogo instituta (Tekhnicheskogo universiteta) — Bulletin of the Saint Petersburg State Institute of Technology (Technical University)*, 29 (55), 10–14. (In Russian)

Lakhtin, Yu. M., Arzamasov, B. N. (1985) *Khimiko-termicheskaya obrabotka metallov [Chemical and thermal processing of metals].* Moscow: Metallurgiya Publ., 256 p. (In Russian)

Lee, S. B., Cho, K. H., Lee, W. G., Jang, H. (2009) Improved corrosion resistance and interfacial contact resistance of 316L stainless-steel for proton exchange membrane fuel cell bipolar plates by chromizing surface treatment. *Journal of Power Sources*, 187, 318–323. https://doi.org/10.1016/j.jpowsour.2008.11.064 (In English)

Likhtman, V. I. (1954) *Vliyaniye poverkhnostno-aktivnoj sredy na protsessy deformatsii metallov [Effect of surface-active environment on metal deformation processes]*. Moscow: USSR Academy of Sciences Publ., 208 p. (In Russian)

Lobanov, M. L., Kardonina, N. I., Rossina, N. G., Yurovskikh, A. S. (2014) *Zashchitnyye pokrytiya [Protective coatings]*. Ekaterinburg: Ural Federal University Publ., 200 p. (In Russian)

Popov, A. A. (1962) *Teoreticheskiye osnovy khimiko-termicheskoj obrabotki stali [Theoretical foundations of chemical-thermal processing of steel]*. Moscow: Metallurgizdat Publ., 120 p. (In Russian)

Rolsten, R. F. (1968) *Jodidnye metally i jodidy metallov [Iodide metals and metal iodides].* Moscow: Metallurgiya Publ., 524 p. (In Russian)

Solntsev, S. S. (2009) *Zashchitnye pokrytiya metallov pri nagreve: Sspravochnoye posobiye [Protective coatings of metals during heating: Reference manual]*. 2nd ed. Moscow: Librokom Publ., 248 p. (In Russian)

Xiaowei, Y., Gotman, I., Klinger, L., Gutmanas, E. Y. (2005) Formation of titanium carbide on graphite via powder immersion reaction assisted coating. *Materials Science and Engineering: A*, 396 (1–2), 107–114. https://doi.org/10.1016/j.msea.2005.01.011 (In English)

Condensed Matter Physics.
Dielectrics

UDC 538.9

EDN LZFLTK
https://www.doi.org/10.33910/2687-153X-2024-5-3-124-128

The effect of ionizing radiation and etching time on low-temperature relaxation in polyvinylidene fluoride

E. A. Volgina ✉[1], D. E. Temnov [1], U. V. Pinaeva [2]

[1] Herzen State Pedagogical University of Russia, 48 Moika Emb., Saint Petersburg 191186, Russia
[2] Joint Institute for Nuclear Research, 6 Joliot-Curie Str., Dubna 141980, Russia

Authors

Elena A. Volgina, ORCID: 0000-0002-1536-5841, e-mail: volgina.elena.1999@mail.ru

Dmitry E. Temnov, ORCID: 0000-0002-9560-4346, e-mail: detem@yandex.ru

Uliana V. Pinaeva, ORCID: 0000-0003-1724-6149, e-mail: pinaeva@jinr.ru

For citation: Volgina, E. A., Temnov, D. E., Pinaeva, U. V. (2024) The effect of ionizing radiation and etching time on low-temperature relaxation in polyvinylidene fluoride. *Physics of Complex Systems*, 5 (3), 124–128. https://www.doi.org/10.33910/2687-153X-2024-5-3-124-128 EDN LZFLTK

Received 3 July 2024; reviewed 17 July 2024; accepted 17 July 2024.

Funding: This study was supported by the Ministry of Education of the Russian Federation as a part of the Government Assignment (project No. VRFY-2023-0005).

Abstract. This study examined the relaxation behavior of the semi-crystalline polymer polyvinylidene fluoride (PVDF) using the thermally stimulated depolarization (TSD) method. Experimental measurements were performed on thin PVDF films irradiated with heavy ions Ne^{4+}, $Xe^{26+,}$ and Bi^{52+} with energies of about 1.2 MeV/nucleon for Ne^{4+} and Xe^{26+}, and about 3.1 MeV/nucleon for Bi^{52+}. Analysis of the obtained TSD spectra revealed the presence of three main relaxation processes at temperatures of around –45 °C, 20 °C and 40 °C. The subsequent chemical etching of the films was found to lead to the emergence of a new relaxation process at a temperature of about –10 °C, which may be due to the appearance of a new type of relaxers on the surface of the tracks.

Keywords: polyvinylidene fluoride, thermal activation spectroscopy, thermostimulated depolarization, track membranes, swift heavy ions (SHI)

Introduction

Polyvinylidene fluoride (PVDF) has gained widespread recognition in the field of micro-sensor and actuator development due to its outstanding mechanical, pyroelectric, ferroelectric and piezoelectric properties, as well as its exceptional biocompatibility (Kawai 1969; Pei et al. 2015). Thanks to these characteristics, PVDF films are actively used in the creation of skin sensors, implantable medical devices and microactuators (Ryu et al. 2005).

However, the performance of sensors and actuators based on PVDF can be significantly influenced by various types of radiation, such as ultraviolet, γ-rays, X-rays, low-energy ions and high-energy heavy ions. The interaction of these radiations with the polymer matrix of the sensor can alter various dielectric relaxation processes in PVDF.

Previous studies (Chailley et al. 1995) focusing on the behavior of PVDF under the influence of high-energy particles revealed that the degree of crystallinity of irradiated α-PVDF decreases depending on the

dose (or fluence) and the magnitude of the specific energy loss dE/dx of ionizing particles. A difference was noted between the rates of crystallinity loss for low-energy particles and high-energy ions. At low doses of irradiation with light particles, such as electrons, oxygen ions and neon ions, amorphization progresses more slowly compared to irradiation with heavier ions.

It is known that crystallinity is an important parameter that determines the piezoelectric, mechanical, optical, electrical and even thermal properties of polymers (Calcagno et al. 1994). However, the influence of high-energy heavy ions (SHI) on the dielectric relaxation properties of PVDF has been insufficiently studied. In polymers, charge accumulation and decay processes are primarily due to various dielectric relaxation processes, such as the orientation of permanent dipoles (orientational polarization), interfacial polarization and bulk charge polarization.

In this study, polyvinylidene fluoride (PVDF) films with a thickness of 9 μm were subjected to irradiation with various heavy ions, such as Ne^{4+}, Xe^{26+} and Bi^{52+}, with energies of approximately 1.2 MeV/nucleon for Ne and Xe and around 3.1 MeV/nucleon for Bi, as well as to etching with different exposure times. The fluence for each type of ion remained constant at approximately 10^9 cm^{-2}. At these specified energies, the ion ranges for Ne, Xe and Bi in PVDF are 13, 19 and 42 μm, respectively.

Thermally stimulated depolarization (TSD) current spectra were used for the analysis. TSD spectra provide a substantial amount of information about dielectric relaxation processes in the studied samples (Bhardwaj et al. 1983; Gorokhovatsky, Temnov 2007; Quamara et al. 2004; Sessler 1980).

Experimental results and discussion

The influence of ionizing radiation on relaxation processes in PVDF

Fig. 1 shows the TSD spectra of a thin polyvinylidene fluoride (PVDF) film irradiated with heavy ions Ne^{4+}, Xe^{26+} and Bi^{52+}, obtained under a polarizing electric field strength of 100 V/mm and a polarization temperature of 70 °C.

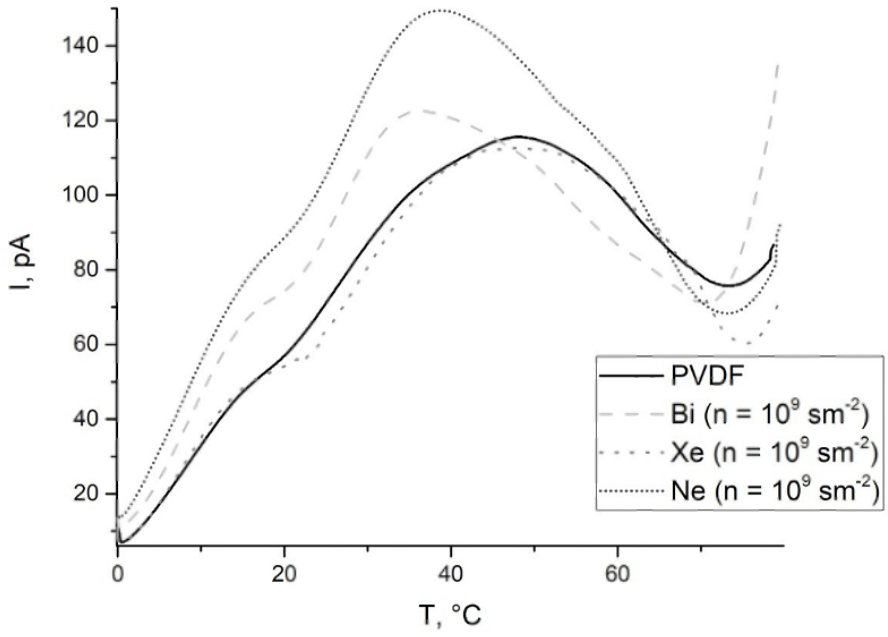

Fig. 1. TSD spectra for PVDF irradiated with heavy ions Ne^{4+}, Xe^{26+} and Bi^{52+} at a heating rate of 9 °C/min and a polarization temperature of 70 °C

Within the temperature range of 0–60 °C, two relaxation processes are observed, typically attributed to αc-relaxation. This relaxation is associated with the dipole-segmental mobility that develops in the intermediate region between the amorphous and crystalline phases. The unfreezing of dipole mobility can occur near defects in the molecular chain (presumably around 20 °C) as well as due to oscillations relative to the C-C chain in the crystalline phase of the polymer (presumably around 40 °C) (Dmitriev et al. 2008).

Polarization of samples at 20 °C allows us to distinguish the relaxation process associated with defect formation within the volume of the polymer during its irradiation with ions of various types.

Fig. 2 shows the dielectric spectra (TSD spectra) for PVDF films obtained at a polarizing electric field intensity of 100 V/mm and a polarization temperature of 20 °C.

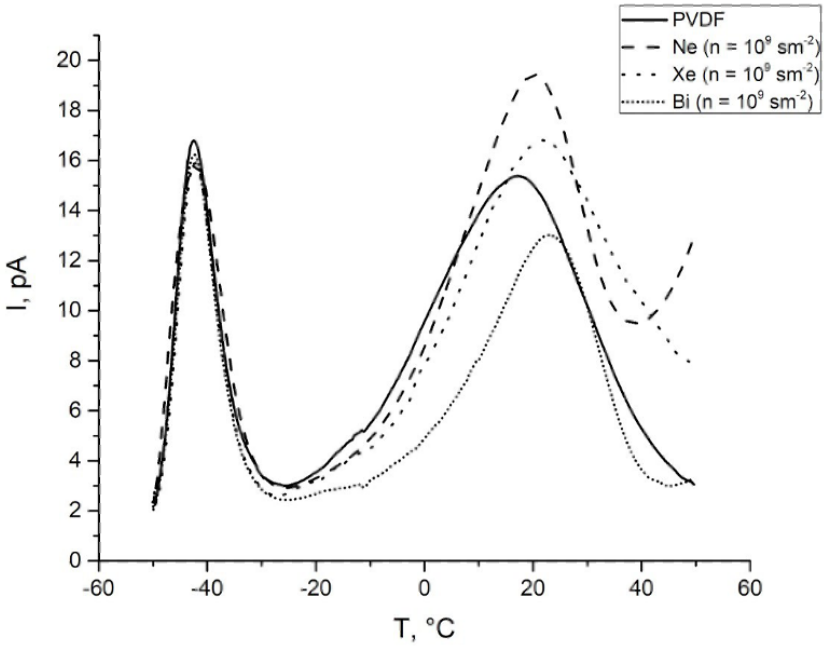

Fig. 2. TSD spectra for PVDF irradiated with heavy ions Ne^{4+}, Xe^{26+} and Bi^{52+} at a heating rate of 9 °C/min and a polarization temperature of 20 °C

It is evident that the maximum of the relaxation process around 20 °C, under Bi ion irradiation, shifts towards higher temperatures, while the intensity of the corresponding TSD peak decreases compared to both the pristine polymer and polymers irradiated with Ne^{4+} or Xe^{26+} ions. This indicates a reduction in the number of mobile molecular segments along with an impediment to their molecular mobility. Indeed, regardless of its crystalline phase, PVDF occupies an intermediate position between polymers that crosslink and those that degrade under irradiation. As the irradiation dose increases and approaches the so-called gel fraction Dg, which ranges from 10 to 35 kGy for PVDF, the dominant chain scission process begins to compete with the crosslinking process, ultimately leading to reduced mobility of molecular chains at lower irradiation doses.

In Fig. 3, the values of the activation energy of the relaxation process are presented as a function of ion charge, calculated using the method of varying the heating rate (Karulina et al. 2024). For irradiation with Bi ions, the activation energy is determined as 0.87 eV, which exceeds the activation energy of this relaxation process in the original unirradiated polymer by 0.2 eV.

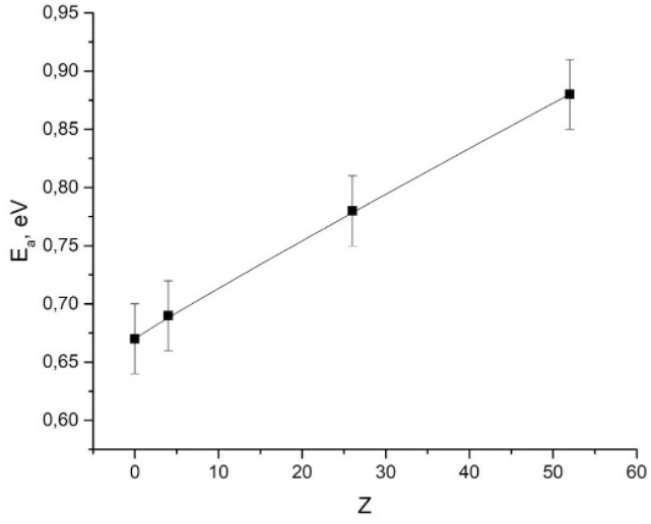

Fig. 3. Dependence of the activation energy on the charge of the incoming ion

 https://www.doi.org/10.33910/2687-153X-2024-5-3-124-128

The influence of etching on relaxation processes in PVDF

Fig. 4 shows the TSD spectra for PVDF films irradiated with Xe^{26+} ions and subjected to chemical etching for varying durations.

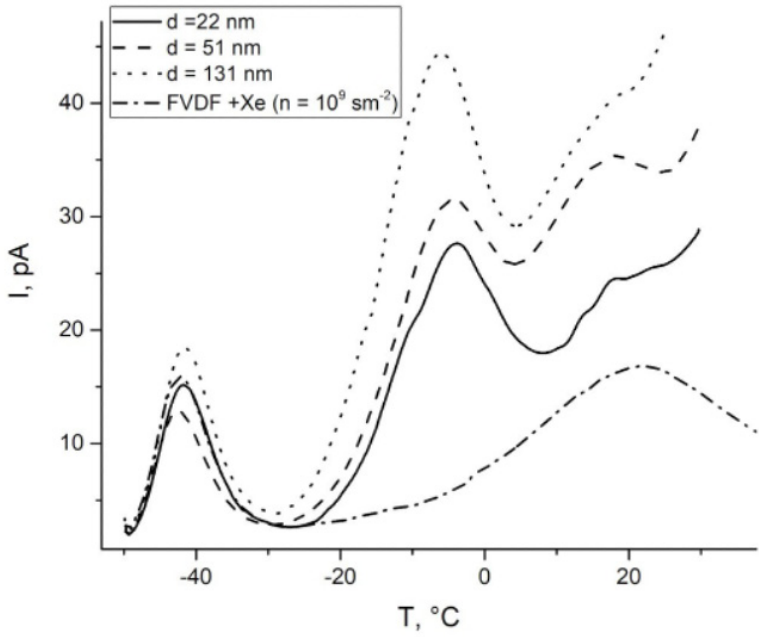

Fig. 4. TSD spectra for PVDF irradiated with heavy ions Xe^{26+} and subjected to etching of various durations at a heating rate of 9 °C/min and a polarization temperature of 20 °C

Etching involves the penetration of small-sized etchant molecules into the core of ion tracks and selective cleavage of chemical bonds within the degraded core through chemical reactions (Apel, Fink 2004). This can lead to the formation of new relaxors in the vicinity of the track walls. In the TSD spectra, this manifests itself as the emergence of a new peak at around –10 °C, absent in the films not subjected to etching. Its intensity increases with prolonged etching time, correlating with the increased surface area of tracks. The activation energy of this process, calculated using the method of varying the heating rate, was determined as 0.81 eV.

Conclusions

1. In the temperature range of 0–20 °C, two relaxation processes were identified using the TSD method: α_1 at around 20 °C (observed in both etched and non-etched irradiated films) and α_2 at around 10 °C, observed only after etching.

2. Increased mass and energy of ionizing ions lead to reduced molecular mobility near forming molecular chain defects and a decrease in the number of mobile chain elements, consequently reducing the intensity of the TSD peak associated with the α_1 relaxation process. The activation energy of the α_1 relaxation process varies from 0.67 eV for the pristine polymer to 0.88 eV for the polymer irradiated with Bi ions.

3. The α_2 relaxation process is linked to the appearance of a new type of relaxors on the track surfaces resulting from chemical etching of the samples. Accordingly, its intensity increases with prolonged etching time. The activation energy of the α_2 relaxation process is 0.81 eV.

Conflict of Interest

The authors declare that there is no conflict of interest, either existing or potential.

Author Contributions

All the authors discussed the final work and took part in writing the article.

References

Apel, P. Y., Fink, D. (2004) Ion-track etching. In.: D. Fink (ed.). *Transport processes in ion-irradiated polymers. Springer Series in Materials Science*, vol. 65. Berlin, Heidelberg: Springer Publ, pp. 147–202. https://doi.org/10.1007/978-3-662-10608-2 (In English)

Bhardwaj, R. P., Quamara, J. K., Nagpaul, K. K., Sharma, B. L. (1983) Field-induced thermally stimulated currents in Kapton-H polyimide films. *Physica status solidi (a)*, 80 (2), 559–566. https://doi.org/10.1002/pssa.2210800219 (In English)

Calcagno, L., Musumeci, P., Percolla, R., Foti, G. (1994) Calorimetric measurements of MeV ion irradiated polyvinylidene fluoride. *Nuclear Instruments and Methods in Physics Research Section B: Beam Interactions with Materials and Atoms*, 91 (1–4), 461–464. https://doi.org/10.1016/0168-583X(94)96269-3 (In English)

Chailley, V., Balanzat, E., Dooryhee, E. (1995) Amorphization kinetics of poly (vinylidene fluoride) on high-energy ion irradiation. *Nuclear Instruments and Methods in Physics Research Section B: Beam Interactions with Materials and Atoms*, 105 (1-4), 110–114. https://doi.org/10.1016/0168-583X(95)00530-7 (In English)

Dmitriev, I. Yu., Gladchenko, S. V., Afanas'eva, N. V., et al. (2008) Molekulyarnaya podvizhnost' polivinilidenftorida v anizotropnom sostoyanii [Molecular mobility of poly(vinylidene fluoride) in the anisotropic state]. *Vysokomolekulyarnye soedineniya. Seriya A*, 50 (3), 424–433. (In Russian)

Gorokhovatski, Yu. A., Temnov, D. E. (2007) Termostimulirovannaya relaksatsiya poverkhnostnogo potentsiala i termostimulirovannye toki korotkogo zamykaniya v predvaritel'no zaryazhennom dielektrike. [Thermally stimulated relaxation of surface potential and thermally stimulated short circuit currents in the charged dielectric.] *Izvestiya Rossijskogo gosudarstvennogo pedagogicheskogo universiteta im. A. I. Gertsena — Izvestia: Herzen University Journal of Humanities & Sciences*, 8 (38), 24–34. (In Russian)

Karulina, E. A., Volgina, E. A., Kulemina, S. M. et al. (2024) The effect of the montmorillonite-based filler on the electret properties of polypropylene. *Saint Petersburg State Polytechnical University Journal. Physics and Mathematics*, 17 (1), 29–37. https://doi.org/10.18721/JPM.17103 (In English)

Kawai, H. (1969) The Piezoelectricity of Poly(vinylidene fluoride). *Japanese Journal of Applied Physics*, 8, 975–983. https://doi.org/10.1143/JJAP.8.975 (In English)

Pei, S., Ai, F., Qu, S. (2015) Fabrication and biocompatibility of reduced graphene oxide/poly (vinylidene fluoride) composite membranes. *RSC Advances*, 5 (121), 99841–99847. https://doi.org/10.1039/c5ra19228e (In English)

Quamara, J. K., Garg, M., Prabhavathi, T. (2004) Effect of high-energy heavy ion irradiation on dielectric relaxation behaviour of kapton-H polyimide. *Thin Solid Films*, 449 (1–2), 242–247. https://doi.org/10.1016/j.tsf.2003.10.099 (In English)

Ryu, J., Park, J., Kim, B., Park, J-O. (2005) Design and fabrication of a largely deformable sensorized polymer actuator. *Biosensors and Bioelectronics*, 21 (5), 822–826. https://doi.org/10.1016/j.bios.2005.01.019 (In English)

Sessler, G. M. (ed.). (1980) *Electrets*. Berlin: Springer Publ., 404 p. (In English)

Condensed Matter Physics.
Physics of atoms and molecules

UDC 533.932

EDN JQUJTT
https://www.doi.org/10.33910/2687-153X-2024-5-3-129-134

Decay of metastable atoms in the afterglow of single-electrode breakdown

V. V. Zaletov ✉[1], A. I. Shishpanov [1], Yu. Z. Ionikh [1]

[1] Saint-Petersburg State University, 7-9-11 Universitetskaya Emb., Saint Petersburg 199034, Russia

Authors

Vladislav V. Zaletov, e-mail: vlad.zaletov@mail.ru

Aleksander I. Shishpanov, ORCID: 0000-0001-5869-3207, e-mail: a.shishpanov@spbu.ru

Yury Z. Ionikh, ORCID: 0000-0003-4817-7174, e-mail: y.ionikh@spbu.ru

For citation: Zaletov, V. V., Shishpanov, A. I., Ionikh, Yu. Z. (2024) Decay of metastable atoms in the afterglow of single-electrode breakdown. *Physics of Complex Systems*, 5 (3), 129–134. https://www.doi.org/10.33910/2687-153X-2024-5-3-129-134 EDN JQUJTT

Received 25 June 2024; reviewed 06 July 2024; accepted 17 July 2024.

Funding: The study did not receive any external funding.

Abstract. This paper deals with experimental studies of ionization waves igniting the breakdown in long discharge tubes in neon at low pressures. Ionization waves were produced by rectangular voltage pulses applied to the high-voltage electrode of the discharge tube. Our research focused on concentration measurements of neon excited atoms at the metastable $1s_5(^3P_2)$ level after the ionization wave passage and the breakdown termination. We also found the characteristic decay times of these states and the most significant elementary processes responsible for metastable atom deactivation.

Keywords: gas discharge, gas breakdown, ionization wave, afterglow, neon plasma, low pressure, metastable atoms, elementary processes

Introduction

Ionization wave (IW) is an electric field solitary wave formed by volume and surface charges and propagated along a gas discharge tube in the form of an ionization front (Lagarkov, Rutkevich 1994; Vasilyak et al. 1994). Due to high field strength at the IW front, high-energy electrons produce intensive ionization and excitation of the gas atoms in the time interval of 10^{-9} – 10^{-6}s, which eliminates heating. That is why IWs are used in longitudinally pumped lasers and fast gas discharge switches (Ashurbekov et al. 2000).

Atoms in metastable states play a significant role in the gas discharge. Some papers (Ashurbekov et al. 2000; 2015; Shakhsinov, Ramazanov 2013) analyze their influence on the dynamics of high-speed IWs ($v > 10^9$ *cm/s*) in long capillary tubes. The movement of the IW front is accompanied by inelastic collisions of high energy electrons with atoms, which leads to the population of metastable levels in addition to ionization. High metastable atom concentration leads to the production of a significant number of high-energy electrons due to second-kind collisions (Raizer 1991). This process affects the radial profile of the IW radiation and the distribution of ionized particles at the front.

The characteristic decay time of the metastable state is much lower than the diffusion one according to the measurements that have been made immediately after the IW passage through the discharge

gap in (Ashurbekov et al. 2000; 2015; Shakhsinov, Ramazanov 2013). This fact indicates the predominance of other channels of their deexcitation. Inelastic collisions with electrons whose concentration is high after the IW passage could be one of them.

Usually, the second electrode of the discharge tube is grounded, which leads to glow discharge ignition after the breakdown. Thus, it becomes impossible to observe plasma decay after the propagation of the pre-breakdown IW only. This motivates us to work with a single-electrode discharge (Shishpanov et al. 2020). It consists of only repetitive passages of IWs with a frequency of that of high-voltage pulses applied to the tube electrode. A glow discharge does not occur in this case, and all excited atoms form at the breakdown stage only. Such discharge mode provides new information about the IW due to enhancement of its observability. A single-electrode breakdown creates a short current pulse, the duration of which is equal to the movement and IW disintegration time (< 10 μs). The beginning of the breakdown afterglow was determined by the IW registration at the opposite tube end using oscillograms of optical signals.

These features of the single-electrode mode motivated us to measure neon metastables' density in the breakdown afterglow, averaged over the tube cross section. We created breakdowns by a positive polarity voltage and chose the pressure range such that the IW front propagates most uniformly across the tube cross section (Starikovskaya 2000). The observation point was taken at a 20-cm distance from the initiating electrode in order to reduce the influence of the possible ring structure of the IW front near the high-voltage anode on the measurements, as was previously observed, for example, in helium at pressures over 10 Torr (Asinovskii et al. 1984). In this research we measured the metastables' densities at different breakdown voltages and several gas pressures after IW propagation.

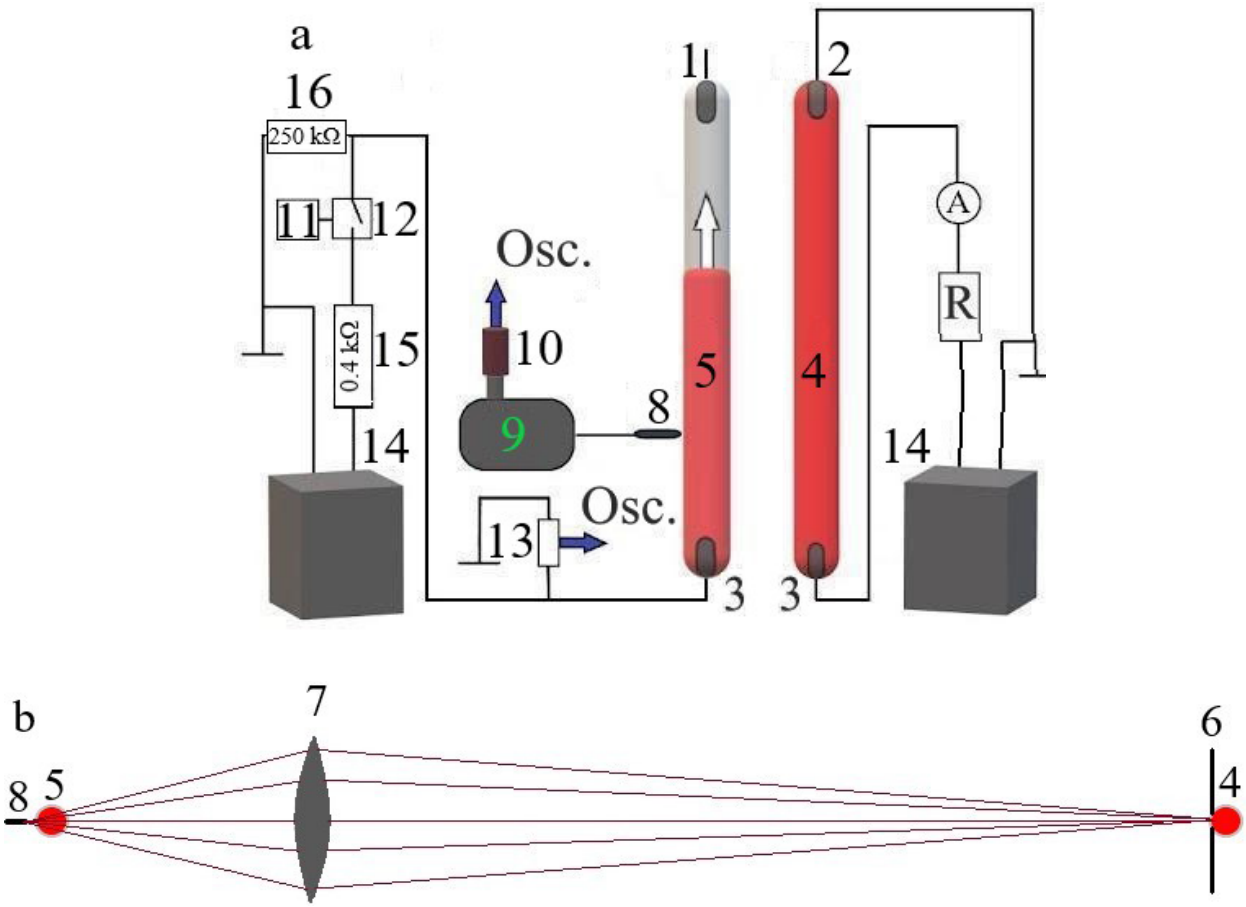

Fig. 1. a — schematic diagram of the experimental setup; b — optical scheme. 1 — unconnected electrode, 2 — grounded electrode, 3 — high voltage electrodes, 4 — radiating tube, 5 — absorbing tube, 6 — diaphragm, 7 — lens, 8 — optical fiber, 9 — monochromator, 10 — PMT, 11 — pulse generator, 12 — switch, 13 — compensated high voltage divider, 14 — high voltage power supply, 15 — resistor (0.4 kΩ), 16 — resistor (0.25 MΩ)

 https://www.doi.org/10.33910/2687-153X-2024-5-3-129-134

Experiment

Fig. 1a shows a schematic diagram of the setup for measuring radiation absorption using the 'two tubes' method (Huddlestone, Leonard 1965). The aim of the diagnostics is to obtain data on the concentration of atoms in metastable states after the IW propagation through the discharge tube. Two parallel discharge tubes with neon, spaced by 40 cm, were used. The inner diameter of each tube was 1.5 cm, and the interelectrode distance was 60–80 cm. The tube electrodes (1–3) were made of aluminum and had the shape of a hollow cylinder, whose edges were covered with ceramic rings to prevent metal sputtering. One of the tube contained DC discharge in neon (p = 0.6 Torr, i = 3–3.5 mA) without stratification and was used as a radiation source (4). The decaying plasma in the afterglow of a single-electrode breakdown in the parallel tube (5) with neon at pressures from 0.6 to 10 Torr was used as the absorbing medium. Light from the source passed through the 0.5 cm diaphragm (6) and was then focused by the lens (7) onto a tube with an absorbing medium according to the diagram in Fig. 1b. Then, the light was collected by an optical fiber (8), aligned perpendicular to the tube axes and transmitted to the monochromator (9) with a photomultiplier (10).

To obtain reliable data, optical signals from different breakdown pulses were accumulated. It was necessary to generate identical IWs to use such recording scheme. We ensured the same initial conditions in every discharge pulse, the main of which was the exciting voltage. The IW and subsequent breakdown were initiated by a rectangular voltage pulse of positive polarity applied to the tube electrode. The pulse rise time (≈50 ns) was shorter than the average breakdown delay time. Thus, the IW appeared after the moment when the pulse voltage reached a constant U_0 value which could be varied in the range of 0.6–4.5 kV. 10 ms pulses were produced at frequencies of 1–5 Hz by the circuit consisting of a generator (Tektronix AFG3022C control oscillator (11)) and a fast switch (12). A compensated high-voltage divider (13) was connected to the oscilloscope showing the voltage behavior at the high-voltage electrode during the breakdown. When a triggering pulse from the generator was applied, the switch connected the high DC voltage power supply (14) with the electrode through a ballast resistor (15). The resistor (16) 0.25 MΩ connected in parallel to the tube provided the appropriate trailing edge of the high voltage pulse (pulse decay time ≈ 200 ns) due to the tube charge removal to the ground after switch disconnection.

The concentration of neon excited atoms at the metastable $1s_5(^3P_2)$ level has been measured by the spectrum line absorption method. For this purpose, we used neon spectral lines λ = 640.2 nm and λ = 614.3 nm. The light source was the plasma of the positive column of the neon glow discharge at low pressure, and the absorber was the afterglow plasma. The emission and absorption line profiles have been chosen Doppler with the gas temperature of T_a = 300 K. Collisional (van der Waals) broadening $\Delta\nu_c$ was estimated as follows. According to (Ochkin 2009),

$$\Delta\nu_c = 1.30 \times N C_6^{2/5} v^{3/5}$$

where N — concentration of unexcited atoms, v — average particle velocity and C_6 — van der Waals interaction constant, for which estimates and analysis of experimental data give the value in the range of $10^{-30} - 10^{-32}\ \frac{cm^6}{s}$. Then, the upper estimate for the $\Delta\nu_c$ value taken for the largest pressure of 10 Torr turned out to be $\Delta\nu_c \approx 3 \times 10^8\ s^{-1}$, whereas the Doppler width is $\Delta\nu_D \approx 1.3 \times 10^9\ s^{-1}$. In the experiment, the absorbed proportion of radiation was ≈ 0.8–0.95, which indicates a low absorption coefficient and hence, a small possible role of Lorentzian collisional wings. From these considerations, we considered the line profile as the Gaussian (Doppler) one.

For calculations the radial concentration distribution of metastable atoms was considered to be: $M(r) = M(0) \times J_0\left(\frac{r}{R}\mu\right)$, where J_0 is the first kind Bessel function of zero order, R is the tube radius and $\mu \approx 2.405$ is the first root of the Bessel function. It is worth noting that this assumption did not significantly affect the result which was the M value averaged over the tube cross section.

Experimental results

The peculiarity of the single-electrode breakdown mode is that the current pulse duration (< 10 μs) associated with the IW passage is much shorter than that of the discharge afterglow. Thus, the decay of metastable states was observed with no sources of their population, except for the IW. Fig. 2(a) shows

the time dependence of concentrations at fixed pressure for different breakdown voltages. By fitting them to the exponential function, the metastable densities at the moment of breakdown M_0 and their characteristic decay times τ have been measured. The relative error for τ was ≲ 10% and for M_0 ≲ 15%. The main result of this experiment is the fact that an increase in the breakdown voltage leads to an increase in the number of metastable atoms remaining after the IW passage. It should be noted that the curves can be approximated by a linear dependence in a logarithmic scale, confirming that the concentration decreases exponentially with the same τ for all voltages. The curves obtained at a fixed breakdown voltage but various pressures are shown in Fig. 2 (b), while the results of their processing are in Table 1. One can see that τ depends on pressure non-monotonically with the maximum at p = 3 Torr. The concentration M_0 grows with increasing pressure, which agrees with the results of other works (Ashurbekov et al. 2000; 2015; Shakhsinov, Ramazanov 2013).

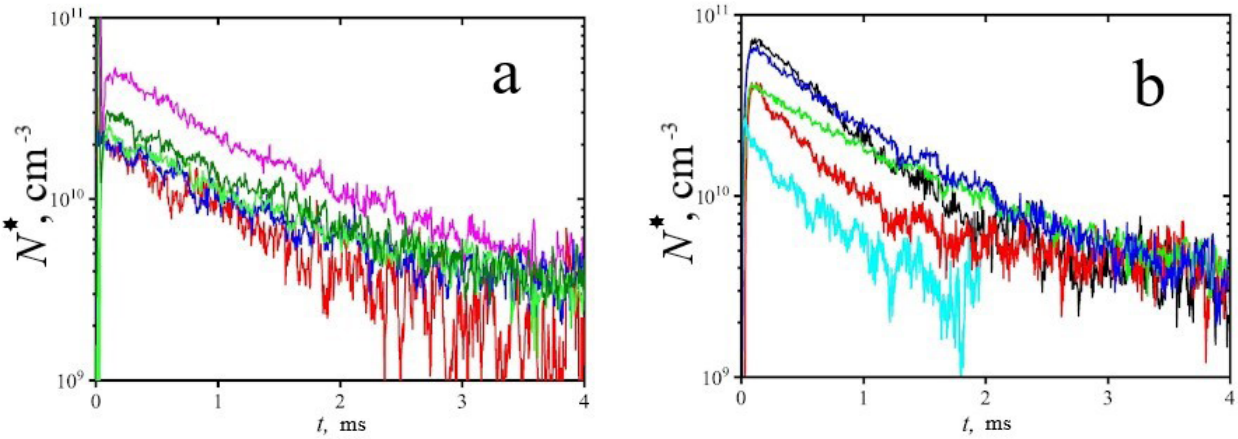

Fig. 2. Time dependences of concentrations of metastable ($1s_5$) neon atoms
(a) at different U_0. p = 3 Torr; pulse frequency is 1 Hz; voltage pulse duration is 10 ms
– 2.5 kV, – 3 kV, – 3.5 kV, – 4 kV, – 4.5 kV.
(b) at different p. U_0 = 3 kV, for 1 Hz and 10 ms.
– 10 Torr, – 5 Torr, – 3 Torr, – 1 Torr, – 0.6 Torr

Table 1. Results of approximation of the experimental time dependence of the metastable atom concentration and results of theoretical calculations

p, Torr	τ_T, ms	τ_{exp}, ms	M_0, $cm^{-3} \times 10^{10}$
0.6	0.30	0.33 ± 0.03	2.0 ± 0.3
1	0.46	0.45 ± 0.05	4.2 ± 0.5
3	0.87	1.0 ± 0.1	4.5 ± 0.6
5	0.74	0.74 ± 0.07	7.0 ± 1.0
10	0.54	0.65 ± 0.05	9.0 ± 1.5

Results and conclusions

We examined the possible channels of the metastable atom decay under the studied conditions. One of them is the diffusion to the discharge tube wall with subsequent deexcitation on it. This process is the most significant at low pressures. The excited atom diffusion lifetime can be expressed in the following way (Raizer 1991): $\frac{\Lambda^2}{D}$, where $\Lambda = R/2.405$ is the effective diffusion length for a cylindrical tube, and D is the diffusion coefficient. Another channel of the excited atoms' decay is the mixing of excited states by atom collisions:

$$Ne(1s_5) + Ne \rightarrow Ne(1s_4) + Ne$$

Since the $1s_4$ level is resonance, its concentration is substantially less than that of metastable atoms, so the reverse process was not factored into the calculations.

 https://www.doi.org/10.33910/2687-153X-2024-5-3-129-134

The dimer formation by collisions and ionization by collisions with other metastable atoms (chemo-ionization) were also taken into account.

$$Ne(1s_5) + Ne + Ne \rightarrow Ne_2^* + Ne \rightarrow Ne + Ne + Ne + h\upsilon$$

$$Ne(1s_5) + Ne(1s_5) \rightarrow Ne^+ + Ne + e$$
$$\rightarrow Ne_2^+ + e$$

The analysis of the obtained data as part of the proposed model was limited only to the above-mentioned processes. Therefore, the balance equation for the metastable atom concentration can be written as follows:

$$\frac{dM}{dt} = -(\frac{(DN)}{\Lambda^2 N} M + K_1 NM + K_2 N^2 M + K_3 M^2),$$

where M is the concentration of atoms at the metastable $1s_5$ level averaged over the tube cross section

N — concentration of unexcited atoms,

$DN = 6.2 \times 10^{18} \frac{1}{cm \cdot s}$ (these and subsequent data are taken from (Dyatko et al. 2006)),

$K_1 = 4.9 \times 10^{-15} \frac{cm^3}{s}$ is the rate constant of excited states' mixing,

$K_2 = 5 \times 10^{-34} \frac{cm^6}{s}$ is the rate constant of three body quenching,

$K_3 = 3.8 \times 10^{-10} \frac{cm^3}{s}$ is the rate constant of chemo-ionization.

Since the contribution of chemo-ionization appears to be negligible, the solution can be represented in the exponential form:

$$M = M_0 \, exp \, [-\frac{t}{\tau}] = M_0 \, exp \, [-t(\frac{(DN)}{\Lambda^2 N} + K_1 N + K_2 N^2 + K_3 M_0)], \quad (1)$$

where M_0 is the concentration of metastable atoms at the moment of time just after the IW passage.

It is important to note that one more process of the metastable $1s_5$ level quenching, *viz.* collisions with thermal electrons

$$Ne(1s_5) + e \rightarrow Ne(1s_4) + e$$

should be considered. The rate constant for it is $K_4 \approx 1 \times 10\text{^}7 \times \text{cm}^3/\text{s}$ (Dyatko et al. 2006). Unfortunately, we have no information on the electron number density n_e in the afterglow. However, it was shown under similar conditions for the IW in argon (Dyatko et al. 2021) that the n_e value varies strongly with the voltage pulse amplitude (two-fold increase in the voltage results in an order of magnitude growth in n_e). So, this reaction should lead to dependence of the decay curves on the pulse voltage, which is not the case (Fig. 2a). Hence, this process can be considered unnoticeable.

The decay times for different pressures were calculated according to (1), and their comparison with experimental data is given in Table 1. Note that the τ dependence on pressure is non-monotonic. For low pressures, the experimental and calculated τ values are close to each other. In these conditions, diffusion to the tube walls is the predominant decay channel. Despite the discrepancies in the measured and estimated values for the higher pressures, the $\tau(p)$ dependence is qualitatively the same in the theoretical calculation and in the experiment. This confirms the correctness of the proposed model. It also follows from the above estimations that the diffusion and mixing of excited states by atom collisions in the investigated pressure range are the dominant metastable atom decay processes.

Conflict of Interest

The authors declare that there is no conflict of interest, either existing or potential.

Authors contributions

All the authors discussed the final work and took an equal part in writing the article.

Acknowledgements

The authors are grateful to A. Z. Devdariani for the preparation of this paper.

References

Ashurbekov, N. A., Iminov, K. O., Shakhsinov, G. S., Ramazanov, A. R. (2015) The role of high-energy electrons during the formation of nonstationary optical emission and transmission spectra of plasma behind the edge of high-velocity ionization waves. *High Temperature*, 53 (5), 627–637. https://doi.org/10.1134/S0018151X15030025 (In English)

Ashurbekov, N. A., Kurbanismailov, V. S., Omarov, O. A., Omarova, N. O. (2000) The kinetics of excited atoms and optical radiation under conditions of wave mechanism of breakdown in inert gases. *High Temperature*, 38 (5), 795–810. https://doi.org/10.1007/BF02755936 (In English)

Asinovskii, E. I., Markovets, V. V., Ul'yanov, A. M. (1984) Elektonno-opticheskie issledovaniya volnovogo proboya v dlinnoj razryadnoj trubke. [Electrooptical studies of wave breakdown in a long discharge-tube]. *Teplofizika vysokikh temperatur*, 22 (4), 667–671. (In Russian)

Dyatko, N. A., Latyshev, F. E., Mel'nikov, A. S., Napartovich, A. P. (2006). Study of the dark phase in the initial stage of the positive column formation in a neon glow discharge. *Plasma Physics Reports*, 32, 158–169. https://doi.org/10.1134/S1063780X06020140 (In English)

Dyatko, N. A., Ionikh, Y. Z., Meshchanov, A. V. (2021) Estimation of plasma parameters in a pre-breakdown ionization wave at the glow discharge ignition in argon. *Plasma Sources Science and Technology*, 30 (5), article 055015. https://doi.org/10.1088/1361-6595/abda9e (In English)

Huddlestone, R. H., Leonard, S. L. (eds.). (1965) *Plasma diagnostics techniques*. Cambridge: Academic Press, 627 p. (In English)

Lagarkov, A. N., Rutkevich, I. M. (1994) *Ionization waves in electrical breakdown of gases*. Berlin: Springer Publ., 231 p. (In English)

Ochkin, V. N. (2009). *Spectroscopy of low temperature plasma*. Weinheim: Wiley-VCH Publ., 609 p. (In English)

Raizer, Y. P. (1991) *Gas discharge physics.* Berlin: Springer Publ., 449 p. (In English)

Shakhsinov, G. Sh., Ramazanov, A. R. (2013) Nestatsionarnye opticheskie spektry izlucheniya vysokoskorostnykh voln ionizatsii v smesyakh inertnykh gazov [Transient optical spectra of high-speed ionization waves in inert gases mixtures]. *Herald of Dagestan State University*, 1 (6), 10–14. (In Russian)

Shishpanov, A. I., Bazhin, P. S., Ivanov, D. O., Meschanov, A. V. (2020) Low-frequency one-electrode discharge in long tubes at low gas pressure. *Plasma Research Express*, 2 (1), article 015012. https://doi.org/10.1088/2516-1067/ab7e83 (In English)

Starikovskaya S. M. (2000) *Impul'snyj razryad pri vysokih perenapryazheniyakh (Osobennosti razvitiya i vozbuzhdenie vnutrennikh stepenej svobody gaza) [Pulse discharge at high overvoltages (Features of development and excitation of internal degrees of freedom of gas)]. DrSci dissertation (Physics and Mathematics)*. Moscow, Moscow Institute of Physics and Technology Publ., 346 p. (In Russian)

Vasilyak, L. M., Kostyuchenko, S. V., Kudryavtsev, N. N., Filyugin, I. V. (1994) Fast ionisation waves under electrical breakdown conditions. *Physics-Uspekhi*, 37 (3), 247–268. https://doi.org/10.1070/PU1994v037n03ABEH000011 (In English)

Theoretical physics.
Physics of atoms and molecules

UDC 530.182

EDN FNIIBG
https://www.doi.org/10.33910/2687-153X-2024-5-3-135-145

Quasienergy of chaotic states in problems of nonlinear dynamics. Degeneration of states due to the symmetry of the system

A. V. Liaptsev ✉[1]

[1] Herzen State Pedagogical University of Russia, 48 Moika Emb., Saint Petersburg 191186, Russia

Authors

Alexander V. Liaptsev, ORCID: 0000-0002-8702-9062, e-mail: lav@herzen.spb.ru

For citation: Liaptsev, A. V. (2024) Quasienergy of chaotic states in problems of nonlinear dynamics. Degeneration of states due to the symmetry of the system. *Physics of Complex Systems*, 5 (3), 135–145. https://www.doi.org/10.33910/2687-153X-2024-5-3-135-145 EDN FNIIBG

Received 20 June 2024; reviewed 5 July 2024; accepted 5 July 2024.

Funding: The study did not receive any external funding.

Abstract. In this paper we analyse chaotic states in a system of coupled Duffing oscillators. The concept of quasienergy of a system is introduced in a way similar to the concept of quasienergy of a quantum mechanical system driven by an external periodic field. We show that in the absence of a connection between the oscillators in the system under consideration, chaotic states with the same value of quasienergy, but different values of the angular momentum are realized when the external influence changes. This fact can be interpreted as the existence of degenerate chaotic states of the system. A numerical experiment shows that taking into account the interaction between oscillators leads to the splitting of quasienergy, similar to the splitting of the quasienergy level in a quantum mechanical system.

Keywords: nonlinear dynamics, chaotic states, chaotic attractor, probability density, quasienergy, degenerate states, numerical experiment

Introduction

Chaotic states in dissipative systems described by equations of nonlinear dynamics have a number of features specific to systems whose states are determined by linear equations. This is explained by the fact that over time, the chaotic states of dissipative systems tend towards a certain set in the phase space called a 'strange attractor' or 'chaotic attractor' (Loskutov 2007). The state described by the chaotic attractor can be characterized by the probability density, which determines the probability of finding a system in a given region of phase space (Sagdeev et al. 1988). The average values of various quantities characterizing these systems can be calculated using probability density, just as it is done for other systems described by probability density: for example, for systems with a large number of particles or quantum mechanical systems.

The equation for the probability density of a system characterized by a chaotic attractor is a linear equation, similar, for example, to the Schrodinger equation for a wave function, the modulus square of which also determines the probability density (Liaptsev 2019). The linearity of the equation for probability density implies a number of properties characteristic of systems described by linear equations. In particular, the response of the system to small perturbations is small and proportional to the small parameter characterizing the perturbation (Liaptsev 2020). This makes it possible to apply perturbation theory in the same way as it is applied to systems described by the equations of quantum mechanics.

It should be noted, however, that when considering a quantum mechanical system in an external field, it is necessary to consider a more general equation for the density matrix instead of the Schrodinger equation (Blum 2012). With sufficiently strong external fields, the system of equations becomes nonlinear. For external fields of optical frequency, such effects are widely studied in a variety of works on nonlinear optics (Allen, Eberly 1987; Andreev et al. 1993; Bayramdurdiyev et al. 2020; 2021; Benedict et al. 1996; Ryzhov et al. 2016; 2017; Ryzhov et al. 2019; 2021a; 2021b).

Other features of the chaotic states of dissipative systems described by the equations of nonlinear dynamics are properties reflecting the symmetry of such systems. These properties are manifested, for example, in the polarization of radiation from such systems (Liaptsev 2014; 2015). The polarization properties, characterized in particular by the Stokes parameters, are similar to the polarization properties of symmetric quantum mechanical systems in degenerate states. This allows us to make the assumption that the chaotic states of dissipative systems can also be degenerate in a certain sense.

For systems whose description is based on the laws of quantum mechanics, degeneracy is defined as the existence of several states having the same energy. It should be noted, however, that systems whose state tends towards a chaotic attractor are open systems, so that the energy of such systems, if any can be determined, is not conserved over time. However, in most cases, chaotic states in such systems arise when the system is subjected to external periodic influence. These systems include, in particular, such model systems as a nonlinear oscillator and a mathematical pendulum located in an external periodic field (Duffing 1918; Grinchenko et al. 2007; Hacken 1978; Kuznetsov et al. 2002; Moon 1987; Sagdeev et al. 1998). These physical systems have one degree of freedom, and the corresponding equations of nonlinear dynamics in an external periodic field are reduced to a system of 3 differential equations of the 1st order. Therefore, such systems are sometimes called systems with 1.5 degrees of freedom. In the problems considered by quantum theory, when describing systems that are driven by an external periodic field, the concepts of quasienergy and, accordingly, quasienergetic states are used (Bordo et al. 1984; Delone, Krainov 1999; Kiselev, Liapzev 1990; Lyaptsev 1994; Zel'dovich 1973). The time-dependent Schrodinger equation for such systems has the following form:

$$i\hbar\frac{\partial\Psi}{\partial t}=(H_0+V(t))\Psi\ , \tag{1}$$

where H_0 is a Hamiltonian in the absence of an external field, and $V(t)$ is a periodic function of time. According to Bloch's theorem, the solution of this equation can be represented as a superposition of solutions of the form:

$$\Psi(t)=\exp\left(-\frac{iEt}{\hbar}\right)\psi(t)\ , \tag{2}$$

where ψ(t) is a wave function that periodically depends on time with the period of the external field. By definition, the E value is called quasienergy, and ψ(t) is the wave function of a quasienergetic state (QES) (Zel'dovich 1973). As in the case of stationary states, QES can be degenerate, that is, several different wave functions can correspond to one value of quasienergy.

When considering dissipative systems described by equations of nonlinear dynamics, the density matrix corresponding to the chaotic attractor also turns out to be periodically time-dependent. This means that for such systems it is also possible to define the concept of quasienergy, using, for example, the limiting transition from quantum mechanics to classical theory. Below, we will apply a similar approach to describe a model system of coupled Duffing oscillators and show that degenerate chaotic states can occur in this case. As it will be shown, the degeneracy in this case is due to the symmetry of the problem, and with a decrease in symmetry, an effect similar to splitting energy levels with a decrease in symmetry in a quantum mechanical problem may occur.

Quasienergies of chaotic states of systems driven by an external periodic field

Let us consider, for simplicity's sake, the case of one-dimensional motion of a single particle in a field with potential energy $U(x,t)$, which depends on the coordinates of the particle x and also periodically depends on time. The Hamiltonian included in the Schrodinger equation (1) can be written as:

 https://www.doi.org/10.33910/2687-153X-2024-5-3-135-145

$$H = -\frac{\hbar^2}{2m}\frac{\partial^2}{\partial x^2} + U(x,t) \ .$$

Substitution of a solution of the form (2) into the Schrodinger equation leads to the equation for the QES:

$$\frac{\hbar^2}{2m}\psi'' + (E-U)\psi + i\hbar\dot{\psi} = 0 \ .$$

Here and further, the strokes indicate the derivatives of x, and the dot above the symbol is the derivative of t. The limiting transition to the classical description is carried out by defining the function $\sigma(x,t)$ (Landau, Lifshitz 1977):

$$\psi = \exp\left(\frac{i\sigma}{\hbar}\right) \ .$$

The equation for the function $\sigma(x,t)$ has the following form:

$$\frac{1}{2m}(\sigma')^2 - \frac{i\hbar}{2m}\sigma'' + \dot{\sigma} = E - U \ .$$

The transition to the classical description is carried out by the representation of the function $\sigma(x,t)$ in the form of a power expansion of the Planck constant:

$$\sigma = \sigma_0 + \frac{\hbar}{i}\sigma_1 + \left(\frac{\hbar}{i}\right)^2 \sigma_2 + \dots \ .$$

In zero approximation, we obtain the equation:

$$\frac{1}{2m}\left(\sigma_0'\right)^2 + \dot{\sigma}_0 = E - U \ .$$

This equation coincides with the Hamilton–Jacobi equation for the action function:

$$\frac{1}{2m}\left(S'\right)^2 + U + \dot{S} = 0 \ ,$$

if you put:

$$S = \sigma_0 - Et \ . \tag{3}$$

According to the periodicity of the function $\psi(x,t)$, the function $\sigma_0(x,t)$ must also be periodic. This is fulfilled within the classical limit if the classical solution $x(t)$ is a periodic function. Indeed, the Lagrangian:

$$L(x,t) = \frac{\dot{x}^2}{2m} - U(x,t)$$

is in this case a periodic function of time. The action is determined by an integral, which, in accordance with expression (3), can be represented as:

$$S = \int_{t_0}^{t} L(t_1)dt_1 = -Et + \sigma_0(t) \ .$$

It can be seen from this expression that in the case of a periodic solution $x(t)$, quasienergy can be defined by the following expression:

$$E = -\frac{1}{T}\int_{t_0}^{t_0+T} L(t_1)dt_1 = -\langle L(t)\rangle\,, \tag{4}$$

where T is the period of the function $U(x,t)$, and the symbol $\langle ...\rangle$ indicates the average value of the Lagrangian over the period.

Note that the explicit calculation of quasienergy can be carried out analytically, for example, in the case of a harmonic oscillator with attenuation driven by an external periodic field. The corresponding equation for the oscillator can be written as:

$$\ddot{x} + \gamma\dot{x} + \omega_0^2 x = f\cos(\omega t)\,.$$

The calculation of quasienergy using formula (4) in this case leads to the expression:

$$E = \frac{f^2}{4\left(\omega_0^2 - \omega^2\right)}\,.$$

This expression corresponds to the quasienergy for an atom in a strong electromagnetic field. The corresponding corrections due to the periodic field are called the dynamic Stark effect (Delone, Krainov 1999).

This expression obtained for a periodic solution can be generalized to chaotic solutions of one-dimensional dissipative systems in a periodic field (a Duffing oscillator, a pendulum in a periodic field). The dynamic system of equations for such systems has the form (Grinchenko et al. 2007):

$$\begin{aligned}\dot{x} &= v,\\ \dot{v} &= F(x) - \gamma v + f(x)\cos(\varphi),\\ \dot{\varphi} &= \omega.\end{aligned} \tag{5}$$

In these equations, $F(x)$ is the force acting on the oscillator, γ is the dissipation coefficient, $f(x)$ is the amplitude of the external field, depending on x, ω is the frequency of the external field, the variables x and v correspond to the coordinate and velocity, and the variable φ is cyclic with a period of 2π. The chaotic state corresponding to the strange attractor can be described using the probability density $\rho(x,v,\varphi)$, which satisfies the partial differential equation (see, for example, (Liaptsev 2020)):

$$\omega\frac{\partial\rho}{\partial\varphi} + v\,\frac{\partial\rho}{\partial x} + (F - \gamma v + f\cos(\varphi))\frac{\partial\rho}{\partial v} = 0\,. \tag{6}$$

It is convenient to represent the three-dimensional phase space of the system under consideration in the form of a torus with the closure of the variable φ. The probability density determined by equation (6) must be normalized by one. Averaging over the time variable in expression (4) in the presence of a chaotic attractor should be replaced by averaging over the entire phase space:

$$E = -\langle L\rangle = -\int L(x,v,\varphi)\rho(x,v,\varphi)dxdvd\varphi\,. \tag{7}$$

Note that when performing calculations, it is not necessary to calculate the density matrix. An equivalent result can be obtained by calculating the average value of L for each of the time periods, followed by averaging over a large number of periods.

Finally, the expression for quasienergy (7) can be easily generalized to the case of more complex systems, for example, coupled oscillators (Liaptsev 2023). In this case, the averaging is simply carried out over the whole phase space, which has dimension $2n+1/2$, where n is the number of degrees of freedom of the system in question.

A model of coupled Duffing oscillators

In systems described by quantum theory, the degeneracy of states with a given energy (also with a given quasienergy) can be due to the symmetry of the system. In this case, the symmetry group must

 https://www.doi.org/10.33910/2687-153X-2024-5-3-135-145

contain non-commuting transformations (Landau, Lifshitz 1977; Petrashen, Trifonov 2009). One of the simplest of such groups is the symmetry group C_{3v}. The simplest model having such symmetry, the solutions of which can be chaotic, is the model of coupled Duffing oscillators. We will consider three symmetrically arranged oscillators with a nonlinear dependence of force on displacement, connected in pairs by an elastic force. The periodic forces acting on each of the oscillators have the same frequency ω, but may differ in phase. The scheme of such a model is shown in Fig. 1.

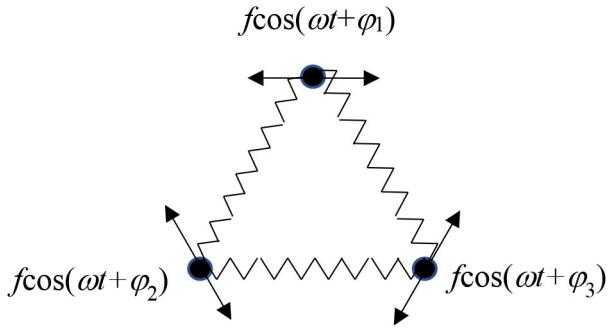

Fig. 1. A model of three coupled Duffing oscillators

The system of dynamic equations for such a model has the form:

$$\begin{aligned}
&\dot{x}_1 = v_1,\\
&\dot{x}_2 = v_2,\\
&\dot{x}_3 = v_3,\\
&\dot{v}_1 = F(x_1) - \gamma v_1 - k(2x_1 - x_2 - x_3) + f\cos(\varphi + \varphi_1),\\
&\dot{v}_2 = F(x_2) - \gamma v_2 - k(2x_2 - x_1 - x_3) + f\cos(\varphi + \varphi_2),\\
&\dot{v}_3 = F(x_3) - \gamma v_3 - k(2x_3 - x_2 - x_1) + f\cos(\varphi + \varphi_3),\\
&\dot{\varphi} = \omega.
\end{aligned} \tag{8}$$

The coefficient k in the equations characterizes the magnitude of the interaction between the oscillators. In the special case, at $k = 0$, there is a system of oscillators not connected by elastic forces.

Harmonic approximation

The system of equations (8) can be solved in the special case when the force $F(x)$ linearly depends on the displacement: $F(x) = -\omega_0^2 x$. The general solution corresponds to a superposition of forced harmonic oscillations. The normal modes of free undamped oscillations (solution of the system of equations (8) at $f = \gamma = 0$) can be classified by irreducible representations of the symmetry group C_{3v}. The displacements corresponding to these fluctuations are shown in Fig. 2.

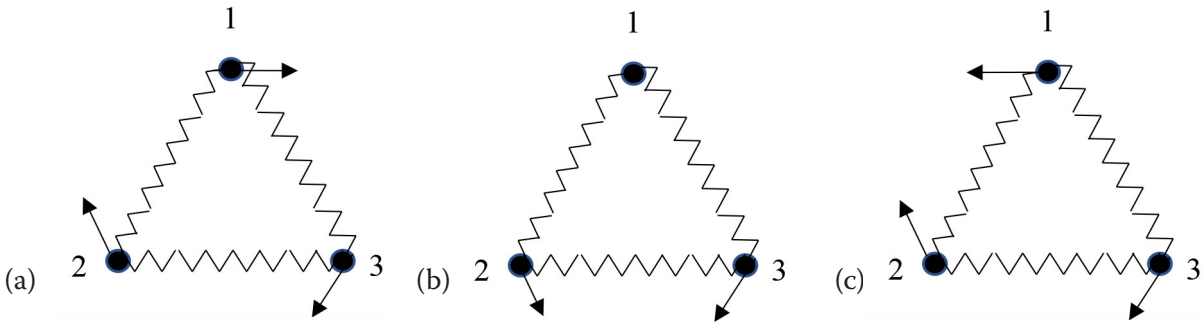

Fig. 2. Displacements corresponding to normal modes of oscillation

The displacements in Fig. 2a correspond to a full-symmetric oscillation (representation A_1), and the displacements in Figs. 2b–2c are oscillations with one natural frequency (representation E). In this case, the vibrations of u_s and u_a are symmetrical and asymmetrical with respect to the reflection in the plane, which is projected onto a vertical line in the figure. Normal coordinates can be expressed in terms of displacements x_1, x_2 and x_3:

$$u_0 = \frac{1}{\sqrt{3}}\left(x_1 + x_2 + x_3\right),$$
$$u_s = \frac{1}{\sqrt{2}}\left(x_2 - x_3\right),$$
$$u_a = \frac{1}{\sqrt{6}}\left(2x_1 - x_2 - x_3\right).$$

Note that for $k = 0$, the considered model consists of three unconnected oscillators. As it is easy to show, in this case all three frequencies of free normal oscillations coincide.

In the new variables, the system of equations (8) is reduced to the form:

$$\begin{aligned}
&\dot{u}_0 = w_0,\\
&\dot{u}_s = w_s,\\
&\dot{u}_a = w_a,\\
&\dot{w}_0 = -\omega_0^2 u_0 - \gamma w_0 +\\
&+\frac{f}{\sqrt{3}}\left(\cos\varphi\left(\cos\varphi_1 + \cos\varphi_2 + \cos\varphi_3\right) - \sin\varphi\left(\sin\varphi_1 + \sin\varphi_2 + \sin\varphi_3\right)\right),\\
&\dot{w}_s = -\omega_0^2 u_s - \gamma w_s - 3k u_s +\\
&+\frac{f}{\sqrt{2}}\left(\cos\varphi\left(\cos\varphi_2 - \cos\varphi_3\right) - \sin\varphi\left(\sin\varphi_2 - \sin\varphi_3\right)\right),\\
&\dot{v}_a = -\omega_0^2 u_a - \gamma w_a - 3k u_a +\\
&+\frac{f}{\sqrt{6}}\left(\cos\varphi\left(2\cos\varphi_1 - \cos\varphi_2 - \cos\varphi_3\right) - \sin\varphi\left(2\sin\varphi_1 - \sin\varphi_2 - \sin\varphi_3\right)\right),\\
&\dot{\varphi} = \omega.
\end{aligned} \tag{9}$$

As can be seen from the resulting system of equations, the amplitude of steady-state oscillations of different symmetry depends on the phase φ_1, φ_2 and φ_3. In particular, at $\varphi_1 = \varphi_2 = \varphi_3$, only full-symmetric oscillations are excited. On the contrary, with ratios $\varphi_2 = -\varphi_3 = \varphi_1 \pm 2\pi/3$, only oscillations with coordinates u_s and u_a are excited.

The normal oscillations of u_s and u_a can be considered as oscillations of a two-dimensional harmonic oscillator. In quantum theory, the excited state of such an oscillator is completely determined by two constants: the energy of the state E and the angular momentum M (Messiah 1999). In general, several states with different values of M can correspond to one energy level. Free oscillations with coordinates u_s and u_a have the same natural frequency; however, the phases of these oscillations may not coincide, which is analogous to the degeneracy of a quantum two-dimensional oscillator. In this case, an additional parameter that determines the state of the excited system of oscillators is the angular momentum, which in this case can be determined as follows:

$$M = u_s w_a - u_a w_s.$$

Since the choice of coordinates u_s and u_a depends on the choice of the plane of symmetry, it is convenient to convert the angular momentum to the original coordinates and velocities, resulting in the expression:

$$M = \frac{1}{6}\left((v_3 - v_2)x_1 + (v_1 - v_3)x_2 + (v_2 - v_1)x_3\right). \tag{10}$$

 https://www.doi.org/10.33910/2687-153X-2024-5-3-135-145

The magnitude of the angular momentum depends both on the parameters that determine the free oscillations of the system (ω_0, k, γ) and on the parameters of external forces ($f, \omega, \varphi_1, \varphi_2, \varphi_3$). When studying the dependence of the angular momentum on the phases of external forces, one of the values can be set to zero without loss of generality, for example, $\varphi_1 = 0$. Then, away from resonance, when $\left|\omega_0^2 - \omega^2 + 3k\right| >> \gamma\omega$ the dependence on the phases and amplitude of external forces takes a simple form:

$$M = Cf^2\left(\sin\varphi_2 - \sin\varphi_3 - \sin(\varphi_2 - \varphi_3)\right), \tag{11}$$

where the constant C depends on the parameters ω_0, ω, γ.

A system of Duffing oscillators in the absence of coupling

Numerical solutions of equations (8) were obtained for a specific type of oscillator forces depending on the displacements:

$$F(x) = x - x^3. \tag{12}$$

Numerical calculation shows that the system of equations (8), as for a single Duffing oscillator, can have chaotic solutions in a certain range of the parameter k. These solutions can be described in terms of probability using the probability density $\rho(x_1, x_2, x_3, v_1, v_2, v_3, \varphi)$, which is determined by an equation similar to equation (6):

$$\omega\frac{\partial\rho}{\partial\varphi} + v_1\frac{\partial\rho}{\partial x_1} + (x_1 - x_1^2 - k\left(2x_1 - x_2 - x_3\right) - \gamma v_1 + f\cos(\varphi + \varphi_1))\frac{\partial\rho}{\partial v_1} +$$
$$+v_2\frac{\partial\rho}{\partial x_2} + (x_2 - x_2^2 - k\left(2x_2 - x_1 - x_3\right) - \gamma v_2 + f\cos(\varphi + \varphi_2))\frac{\partial\rho}{\partial v_2} +$$
$$+v_3\frac{\partial\rho}{\partial x_3} + (x_3 - x_3^2 - k\left(2x_3 - x_2 - x_1\right) - \gamma v_3 + f\cos(\varphi + \varphi_3))\frac{\partial\rho}{\partial v_3} = 0.$$

Let us first consider the case when the oscillators are not connected by elastic forces ($k = 0$). In this case, probability density can be expressed in terms of probability densities for each of the oscillators:

$$\rho(x_1, x_2, x_3, v_1, v_2, v_3, \varphi) = \frac{1}{2\pi}\rho_0(x_1, v_1, \varphi + \varphi_1)\rho_0(x_2, v_2, \varphi + \varphi_2)\rho_0(x_3, v_3, \varphi + \varphi_3), \tag{13}$$

where $\rho_0(x, v, \varphi)$ is the solution of equation (6) for the function $F(x)$ defined by expression (12).

When calculating the average values using the expression (12), it should be taken into account that probability densities are normalized by one for any value φ:

$$\int dxdv\rho(x, v, \varphi) = 1.$$

As a result of these conditions, the average value of a function that depends only on the variables of one oscillator $\left\langle A(x_i, v_i)\right\rangle$ does not depend on the parameters φ_1, φ_2, φ_3. It follows that the quasienergy defined by expression (7) for oscillators not coupled by elastic forces does not depend on phases φ_1, φ_2, φ_3 either.

On the contrary, the average values of the quantities, which are products of variables related to different oscillators, turn out to depend on the parameters φ_1, φ_2, φ_3. In particular, for the average value of the angular momentum, we obtain:

$$\bar{M}(\varphi_1, \varphi_2, \varphi_3) = \frac{1}{6}\int\frac{d\varphi}{2\pi}(\bar{x}(\varphi + \varphi_1)(\bar{v}(\varphi + \varphi_3) - \bar{v}(\varphi + \varphi_2)) +$$
$$+\bar{x}(\varphi + \varphi_2)(\bar{v}(\varphi + \varphi_1) - \bar{v}(\varphi + \varphi_3)) + \bar{x}(\varphi + \varphi_3)(\bar{v}(\varphi + \varphi_2) - \bar{v}(\varphi + \varphi_1))). \tag{14}$$

Here, the average values of coordinates and velocities are calculated using the probability density $\rho_0(x, v, \varphi)$:

$$\overline{x}(\varphi+\varphi_i)=\int dxdv\rho_0(x,v,\varphi+\varphi_i)x,\quad \overline{v}(\varphi+\varphi_i)=\int dxdv\rho_0(x,v,\varphi+\varphi_i)v\,.$$

Thus, two different methods can be used to calculate the average value of the angular momentum in this case. In the first method, calculations are performed directly by solving the system of equations (8) over a sufficiently large time interval, followed by time averaging. In the second method, by solving a system of equations for one oscillator over a sufficiently large time interval, the probability density $\rho_0(x,v,\varphi)$ is determined and then the formula (14) is used.

In a numerical experiment, the dependence of the average value of the angular momentum was studied at $\varphi_1=0,\quad \varphi_2=\frac{2\pi}{3}s,\quad \varphi_3=-\frac{2\pi}{3}s$, at $s\in[-1,1]$. The corresponding dependence graphs $\overline{M}(\sigma)$, where $\sigma=\text{sign}(s)\sqrt{|s|}$, are shown in Fig. 3.

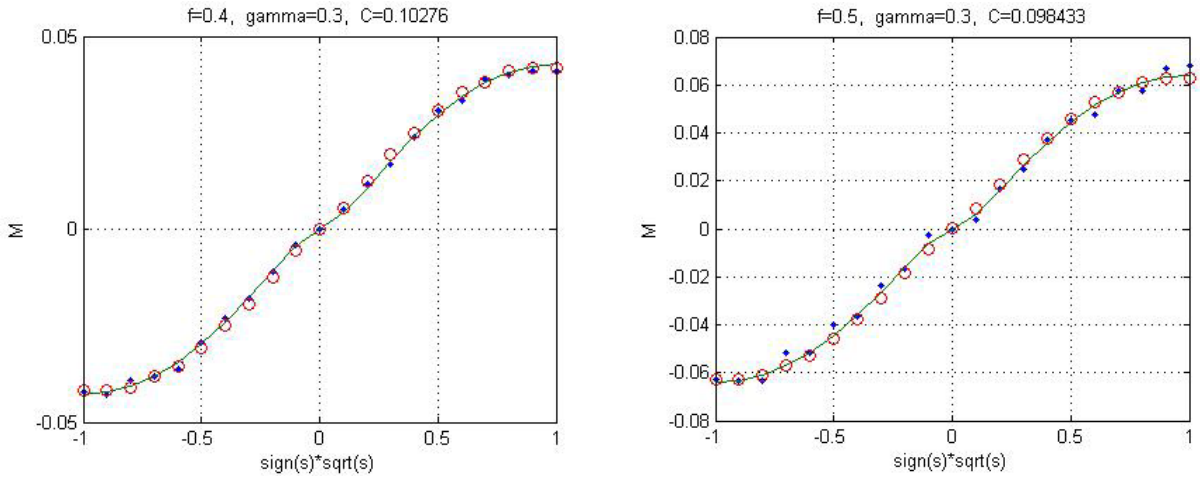

Fig. 3. The average values of the angular momentum when changing the parameters φ_1, φ_2, φ_3

Dots on the graphs indicate the values obtained by the first method (averaging over time when solving equations for three oscillators), and circles indicate the values obtained by the second method (averaging with the density matrix of one oscillator according to formula (14)). To compare with the results of the dependence for the case of harmonic oscillators, formula (11) was used, where the constant *C* was determined by the least squares method. The corresponding curve is represented by a solid line. It should be noted that the values of the constants *C* for different values of the parameters *f* turn out to be close.

The results show that the numerical calculations made by various methods coincide quite well, and the dependence on phases φ_1, φ_2, φ_3 and amplitude *f* is similar to the dependence obtained by analytical methods for the case of a harmonic oscillator.

In this case, states with a different set of phases correspond to the same value of quasienergy; we can therefore point out degenerate states, similar to what takes place in systems described by quantum theory. However, comparing the results with the quantum mechanical description, we should note that chaotic states are equivalent to mixed states described using the density matrix in quantum theory. Unlike quantum theory, where the density matrix can be constructed as a bilinear function of stationary states (see, for example, (Landau, Lifshitz 1977)), in the case of chaotic states of nonlinear classical dynamics, the principle of superposition of states is inapplicable. Therefore, it is impossible to represent the probability density as a superposition of functions that transform according to some irreducible representation of the symmetry group. Nevertheless, it can be argued that at a value $s=0$, the density matrix $\rho(x_1,x_2,x_3,v_1,v_2,v_3,\varphi)=\frac{1}{2\pi}\rho_0(x_1,v_1,\varphi)\rho_0(x_2,v_2,\varphi+\frac{2\pi s}{3})\rho_0(x_3,v_3,\varphi-\frac{2\pi s}{3})$ corresponds to a fully symmetric state in which the average value of the angular momentum is zero.

As the modulus of the value *s* increases, the modulus of the value of the average angular momentum increases, which means that a component appears in the mixture of states that transforms according to the representation *E* of the symmetry group C_{3v}. In the harmonic approximation, as follows from equations (8), a full-symmetric oscillation with zero angular momentum is not excited at the phase ratio

 https://www.doi.org/10.33910/2687-153X-2024-5-3-135-145

$\varphi_2 = -\varphi_3 = \varphi_1 \pm 2\pi/3$. In a chaotic regime, it can only be argued that the proportion of a full-symmetric oscillation in the probability density takes on a minimum value at the phase ratio $\varphi_2 = -\varphi_3 = \varphi_1 \pm 2\pi/3$.

Splitting of the average values of quasienergy at $k \neq 0$

As follows from equations (8), the three natural oscillation frequencies of the system for a harmonic oscillator coincide. When the value $k \neq 0$, the frequency of the full-symmetric oscillation becomes different from the frequency of the symmetry oscillation E, thus having a degeneracy equal to two. The difference in frequency values increases with the growth of the parameter k. In quantum theory, the corresponding phenomenon is called splitting of the energy level (or quasienergy level under external periodic influence). In this case, with a chaotic oscillation, there can be no discreteness of quasienergy values, of course. However, it is possible to investigate the change in the average value of quasienergy with an increase in the value of k, starting from zero. The results of the corresponding numerical experiment are shown in Fig. 4.

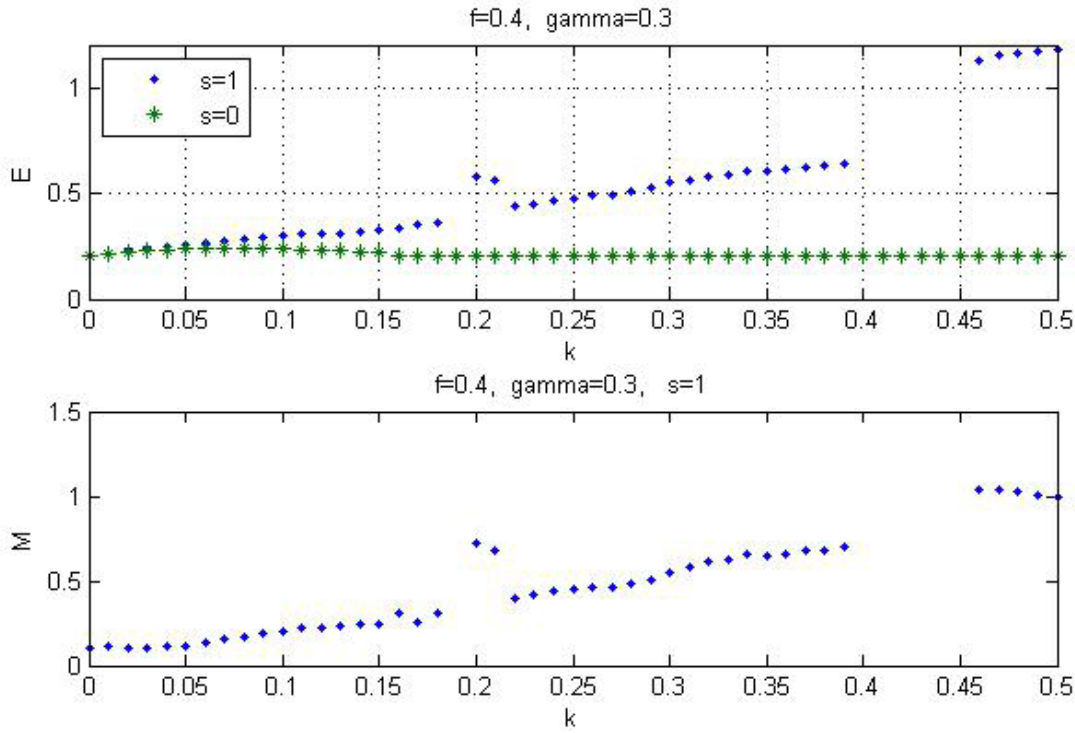

Fig. 4. Quasienergy and angular momentum depending on the magnitude of the interaction of the oscillators k

The upper figure shows the quasienergy values at the phase ratio $\varphi_1 = \varphi_2 = \varphi_3$ ($s = 0$), which corresponds to the zero value of the angular momentum, and the quasienergy values at the phase ratio $\varphi_2 = -\varphi_3 = \varphi_1 \pm 2\pi/3$ ($s = 1$), which corresponds to the maximum value of the average angular momentum. The lower figure shows the values of the average angular momentum at $s = 1$ and the corresponding values of the parameter k. Discontinuities in the graphs arise due to the fact that in the regions of the corresponding values of the parameter k, the solutions of the equations are not chaotic but regular (periodic).

Conclusion

It may seem strange that the results obtained for regular solutions in the case of interaction of an external field with a system of harmonic oscillators turn out to be similar in the case of nonlinear Duffing oscillators with chaotic solutions. In fact, this is largely due to the properties of the symmetry of the system. Similar conclusions can be obtained, for example, by examining a quantum mechanical system of three nonlinear oscillators located in an external field similar to the one discussed above. The density matrix of such a system, which determines the population of an excited degenerate level, turns out to be proportional to the square of the matrix element $\langle 0|V|i\rangle$, where V is the operator of interaction with an external field, 0 corresponds to a non-degenerate ground state, and i corresponds to one of the

degenerate excited states due to symmetry. The corresponding equations for the density matrix are derived, for example, in the monograph (Blum 2012). For the case considered here, the operator of interaction with an external field can be written as:

$$V(t) = \sum_j d_j f \cos(\omega t + \varphi_j),$$

where d_j is the operator of the dipole moment of the j-th oscillator. Further calculation of the density matrix using symmetry properties leads to an average value of the angular momentum, with a dependence similar to (11).

Conflict of Interest

The authors declare that there is no conflict of interest, either existing or potential.

Author Contributions

All the authors discussed the final work and took part in writing the article.

References

Allen, L., Eberly, J. H. (1987) *Optical resonance and two-level atoms*. New York: Dover Publ., 233 p. (In English)

Andreev, A., Emel'ianov, V. I., Il'inskii, Yu. A. (1993) *Cooperative Effects in Optics*. Bristol: IOP Publ., 470 p. (In English)

Bayramdurdiyev, D. Y., Malikov, R. F., Ryzhov, I. V., Malyshev, V. A. (2021) Nonlinear optical dynamics of two-dimensional super-lattices of quantum V-emitters. *Journal of Physics: Conference Series*, 2103, article 012225. https://doi.org/10.1088/1742-6596/2103/1/012225 (In English)

Bayramdurdiyev, D. Ya., Malikov, R. F., Ryzhov, I. V., Malyshev, V. A. (2020) Nelinejnaya opticheskaya dinamika i vysokaya otrazhatel'naya sposobnost' monosloya trekhurovnevykh kvantovykh izluchatelej s dubletom v vozbuzhdennom sostoyanii [Nonlinear optical dynamics and high reflectance of a monolayer of three-level quantum emitters with a doublet in the excited state]. *Zhurnal eksperimental'noj i teoreticheskoj fiziki — Journal of Experimental and Theoretical Physics*, 158, 2 (8), 269–281. https://doi.org/10.31857/S0044451020080040 (In Russian)

Benedict, M. G., Ermolaev, A. M., Malyshev, V. A. et al. (1996) *Super-Radiance: Multiatomic Coherent Emission*. New York: CRC Press, 338 p. https://doi.org/10.1201/9780203737880 (In English)

Blum, K. (2012) *Density matrix theory and applications*. Berlin: Springer Publ., 327 p. https://doi.org/10.1007/978-3-642-20561-3 (In English)

Bordo, V. G., Kiselev, A. A., Liapzev, A. V. (1984) Hyperfine structure of Stark sublevels in a resonant electromagnetic field. *Journal of Physics B: Atomic and Molecular Physics*, 17, article 3455. https://doi.org/10.1088/0022-3700/17/17/016 (In English)

Delone, N. B., Krainov, V. P. (1999) AC-Stark shift of atomic levels. *Physics-Uspekhi*, 42 (7), 669–687. http://dx.doi.org/10.1070/PU1999v042n07ABEH000557 (In English)

Duffing, G. (1918) *Erzwungene Schwingungen bei Veränderlicher Eigenfrequenz und ihre Technische Bedeutung [Forced oscillations with variable natural frequencies and their technical significance]*. Braunschweig: Vieweg Publ., 134 p. (In German)

Grinchenko, V. T., Matsipura, V. T., Snarskij, A. A. (2007) *Vvedenie v nelinejnuyu dinamiku. Khaos i fraktaly [Introduction to Nonlinear dynamics. Chaos and fractals]*. 2nd ed. Moscow: URSS Publ., 283 p. (In Russian).

Hacken, H. (1978) *Synergetics: An introduction nonequilibrium phase transitions and self-organization in physics, chemistry and biology*. Berlin: Springer Publ., 376 p. https://doi.org/10.1007/978-3-642-96469-5 (In English)

Kiselev, A. A., Liapzev, A. V. (1990) Effects of crossings and quasi-crossings of quasi-energy levels in spectra of molecules placed in a strong resonant field. *Journal of Molecular Structure*, 218, 339–343. https://doi.org/10.1016/0022-2860(90)80290 (In English)

Kuznetsov, A. P., Kuznetsov, S. P., Ryskin, N. M. (2002) *Nelinejnye kolebaniya [Nonlinear oscillations]*. Moscow: Fizmatlit Publ., 292 p. (In Russian)

Landau, L. D., Lifshitz, E. M. (1977) *Quantum mechanics: Non-relativistic theory*. Oxford: Pergamon Press, 688 p. (In English)

Liaptsev, A. V. (2014) Simmetriya v zadachakh nelinejnoj dinamiki. Proyavlenie svojstv simmetrii v polyarizatsii izlucheniya [Symmetry in problems of nonlinear dynamics. The manifestation of the properties of the symmetry in the polarization of radiation] *Izvestiya Rossijskogo gosudarstvennogo pedagogicheskogo universiteta im. A. I. Gertsena. — Izvestia: Herzen University Journal of Humanities & Sciences*, 168, 16–28. (In Russian)

Liaptsev, A. V. (2015) Proyavlenie svojstv simmetrii v zadachakh nelinejnoj dinamiki. Effekty, analogichnye vyrozhdeniyu v kvantovomekhanicheskikh zadachakh [Manifestation of symmetry properties in problems of nonlinear dynamics. Effects analogous to degeneration in quantum mechanical problems] *Izvestiya Rossijskogo gosudarstvennogo pedagogicheskogo universiteta im. A. I. Gertsena — Izvestia: Herzen University Journal of Humanities & Sciences,* 173, 64–77. (In Russian)

Liaptsev, A. V. (2020) Linear properties of chaotic states of systems described by equations of nonlinear dynamics: Analogy with quantum theory. *Physics of Complex Systems*, 1 (4), 150–157. https://doi.org/10.33910/2687-153X-2020-1-4-150-157 (In English)

Liaptsev, A. V. (2023) Interaction of subsystems in nonlinear dynamics problems. Various phases of chaos. *Physics of Complex Systems*, 4 (3), 103–111. https://www.doi.org/10.33910/2687-153X-2023-4-3-103-111 (In English)

Liaptsev, A. V. (2019) The calculation of the probability density in phase space of a chaotic system on the example of rotator in the harmonic field. *Computer Assisted Mathematics*, 1, 55–65. (In English)

Loskutov, A. Yu. (2007) Dynamical chaos: Systems of classical mechanics. *Physics-Uspekhi*, 50 (9), 939–964. https://doi.org/10.1070/PU2007v050n09ABEH006341 (In English)

Lyaptsev, A. V. (1994) Resonance fluorescence upon interference of quasi-energy atomic states caused by the dynamic Stark effect. *Optics and Spectroscopy,* 77 (5), 627–632. (In English)

Messiah, A. (1999) *Quantum Mechanics. Vol. 2*. New York: Dover Publ., 1136 p. (In English)

Moon, F. C. (1987) *Chaotic Vibrations: An introduction for applied scientists and engineers*. New York: Wiley-Interscince Publ., 322 p. (In English)

Petrashen, M. I., Trifonov, E. D. (2009) *Applications of Group Theory in Quantum Mechanics*. New York: Dover publications Publ., 330 p. (In English)

Ryzhov, I. V., Malikov, R. F., Malyshev, A. V., Malyshev, V. A. (2019) Nonlinear optical response of a two-dimensional quantum-dot supercrystal: Emerging multistability, periodic and aperiodic self-oscillations, chaos, and transient chaos. *Physical Review A*, 100 (3), article 033820. https://doi.org/10.1103/PhysRevA.100.033820 (In English)

Ryzhov, I. V., Malyshev, V. A., Malikov, R. F., Malyshev, A. V. (2021a) Quantum metasurfaces of arrays of Λ-emitters for photonic nano-devices. *Journal of Optics*, 23 (11), article 115102. https://doi.org/10.1088/2040-8986/ac2788 (In English)

Ryzhov, I. V., Malyshev, V. A., Malikov, R. F., Malyshev, A. V. (2021b) Nonlinear optical dynamics of 2D supercrystals of quantum Λ-emitters. *Journal of Physics: Conference Series*, 2103 (1), article 012226. https://doi.org/10.1088/1742-6596/2103/1/012226 (In English)

Ryzhov, I. V., Vasil'ev, N. A., Kosova, I. S. et al. (2016) Bezynversionnoe sverhizluchenie i model' Duffinga [Inversion-free superradiance and the Duffing model] *Optika i spektroskopiya — Optics and Spectroscopy*, 120 (3), 462–469. (In Russian)

Ryzhov, I. V., Vasil'ev, N. A., Kosova, I. S. et al. (2017) Cooperative emission from an ensemble of three-level Λ radiators in a cavity: An insight from the viewpoint of dynamics of nonlinear systems. *Journal of Experimental and Theoretical Physics*, 124 (5), 683–700. https://doi.org/10.1134/S1063776117050053 (In English)

Sagdeev, R. Z., Usikov, D. A, Zaslavskii, G. M. (1988) *Nonlinear physics: From the pendulum to turbulence and chaos.* New York: Harwood Academic Publ., 675 p. (In English)

Zel'dovich, Ya. B. (1973) Scattering and emission of a quantum system in a strong electromagnetic wave. *Soviet Physics Uspekhi*, 16 (3), 427–433. https://doi.org/10.1070/PU1973v016n03ABEH005192 (In English)

Physics of Complex Systems, 2024, vol. 5, no. 3
www.physcomsys.ru

Theoretical physics.
Theory of condensed matter

UDC 538.9

EDN WTEGLX
https://www.doi.org/10.33910/2687-153X-2024-5-3-146-153

Information in complex physical systems: Kolmogorov complexity plane of interacting amplitudes

D. T. Mihailović ✉[1], V. P. Singh [1]

[1] University of Novi Sad, 3 Dositeja Obradovica Sq., Novi Sad 21000, Serbia
[2] Texas A&M University, 400 Bizzell Str., Texas 77843, USA

Authors

Dragutin T. Mihailović, ORCID: 0000-0002-8380-1844, e-mail: guto@df.uns.ac.rs

Vijay P. Singh, ORCID: 0000-0003-1299-1457, e-mail: vsingh@tamu.edu

For citation: Mihailović, D. T., Singh, V. P. (2024) Information in complex physical systems: Kolmogorov complexity plane of interacting amplitudes. *Physics of Complex Systems*, 5 (3), 146–153. https://www.doi.org/10.33910/2687-153X-2024-5-3-146-153 EDN WTEGLX

Received 23 May 2024; reviewed 6 July 2024; accepted 6 July 2024.

Funding: The study did not receive any external funding.

Abstract. One of the most challenging tasks in studying complex physical systems is determining the contributions of complexities of individual components to the complexity of the entire system. To investigate these contributions, this paper proposed the Kolmogorov complexity plane (the KC plane) based on the Kolmogorov complexity. We applied both the Kolmogorov complexity plane and the Kolmogorov complexity to daily (measured) and monthly (simulated by a climate model) values of precipitation representing a complex physical system, and temperature and water vapor pressure as individual components of that system. From the KC plane, we determined the intervals of interacting amplitudes in which the contributions of the complexities of individual components to the overall complexity could be observed.

Keywords: physical complex systems, Kolmogorov complexity, Kolmogorov complexity spectrum, Kolmogorov complexity plane, overall complexity, complexity of components

Introduction

It took almost half a century after the publication of Nobel Laureate Philip Anderson's pioneering and visionary work 'More is different: Broken symmetry and the nature of the hierarchical structure of science' (Anderson 1972) for complex systems, including the climate system, to receive formal recognition from the scientific community. In 2021, three scientists were awarded the Nobel Prize 'for groundbreaking contributions to our understanding of complex systems': Syukuro Manabe and Klaus Hasselmann 'for the physical modelling of Earth's climate, quantifying the variability and reliably predicting global warming' and Giorgio Parisi 'for the discovery of the interplay of disorder and fluctuations in physical systems from atomic to planetary scales' (The Nobel Prize in Physics 2021… 2021).

When it comes to a complex system, there is no clear formal definition that describes it in terms of its properties. Many papers have been written on this topic (for example, (Estrada 2023)); however, in this paper, we do not deal with this issue but discuss only the two most discriminating features of complex systems — emergence and complexity. Emergence is loosely considered as a behavior of a system that is more than the sum of its parts (De Wolf, Holvoet 2005). The behavior of a complex system is referred to as *weak emergence*, or simply *emergence*, when interactions between components at lower levels

create new properties at higher levels. Weak emerging properties are scale-dependent. On the other hand, the behavior when high-level characteristics cannot be inferred from low-level properties is called *strong emergence*. A system exhibits complexity when we cannot explain its behavior by examining its components. We can only use various complexity measures to compute complexity as the only way to obtain information about the complex systems' nature through measured time series. Emergence and complexity *cannot* be modeled due to various reasons, such as the boundaries of our knowledge and computational power. That is why one resorts to 'model' complexity and emergence with more or less sophisticated models (Mihailović et al. 2023).

In physics, emergence describes a property, law or phenomenon occurring spatially or temporally at macroscopic scales, but not at microscopic scales, although a macroscopic system can be viewed as a very large ensemble of microscopic systems (Girvin, Yang 2019). Complex physical systems follow fixed physical laws, usually described by differential equations, and exhibit properties such as self-organized criticality, self-similarity, scaling and power laws. Also, the majority of complex systems in physics are complicated, while the opposite is not true (Gell-Mann, Lloyd 1996). What do emergent phenomena look like in complex physical systems? Spontaneously broken symmetries that characterize distinct phases of matter are weakly emergent. Thus, according to (Bedau 1997), some phase transitions can be classified as weak emergence. Quantum mechanics is one promising area of physics that can be considered a candidate for strong emergence (Mihailović et al. 2023). Except for the mentioned phase transition, the superconductivity, granular materials are typical physical systems characterized by a weak emergency. Physical complex systems consist of many interconnected components whose interactions produce emergent behavior that cannot be easily predicted from the behavior of individual components. Here are several examples across different domains: weather systems, ecosystems, wildfires, oil spills, human brain, financial markets, traffic systems, social networks, cellular systems, power grids, internet and communication networks, supply chains, galaxies and stellar systems and biochemical pathways.

What is the situation regarding information in the physics of complex systems? It is more complicated to extract information from other complex systems in nature than from systems in physics. A favorable circumstance for physical systems is that they possess some characteristics that are not inherent in other systems (Hanel, Thurner 2013; Thurner et al. 2018). For physical systems that are described algorithmically, in general, we can obtain information about how their internal states (interactions) and the states of components evolve over time. There are several approaches to studying complex physical systems. Some of those include physical approaches, computational approaches, network approaches, statistical approaches (statistical methods, statistical physics, information theory and nonlinear dynamics) and interdisciplinary approaches. In general, methods for obtaining information from complex systems can be divided into methods for (1) analyzing data, (2) constructing and evaluating models and (3) computing complexity. Here we focus only on algorithmic information theory.

Perhaps one of the most challenging tasks in studying complex physical systems is determining the contributions of the complexities of individual components to the complexity of the entire system. Some of the methods attempting to meet this challenge include: (1) analyzing interconnectedness; (2) assessing feedback loops; (3) mapping out dependencies; (4) conducting sensitivity analysis; (5) using network theory; and (6) simulating scenarios. In this paper, we propose a method for determining the information about the interaction of components in a complex physical system by the Kolmogorov complexity spectra (hereafter, KC spectrum/spectra) amplitudes. This method, which we call the Kolmogorov complexity plane (KC plane), is based on the use of the Kolmogorov complexity (KC) (Kolmogorov 1965) and the KC spectrum (Mihailović et al. 2015). More specifically, the KC plane is imagined to have the following axes: (i) interactive amplitudes of the system components' complexity (x-axis) and (ii) interactive amplitudes of the system's overall complexity (y-axis).

Kolmogorov complexity

Kolmogorov complexity $K(x)$ is a well-known concept in algorithmic information theory (Kolmogorov 1965). It is generally incomputable, and the most famous and most widely used algorithm (LZA) for its approximation was developed by Lempel and Ziv (Lempel, Ziv 1976) and improved (known as the LZW algorithm) by (Welch 1984). For a given time series, LZA determines the minimal number of different patterns (Kaspar, Schuster 1987). When applied to a time series $\{x_i\}$, $i = 1,2,3, \dots, N$, LZA includes the following steps: 1. Creating a sequence $\{S_i\}$, $i = 1,2,3, \dots, N$ of the characters 0 and 1 by applying the rule $S_i = 0$ if $x_i < x_{tr}$ or 1 if $x_i > x_{tr}$, where x_{tr} is a threshold. The mean value of a time series is usually chosen as the

threshold. 2. Computing the minimum number of different patterns $c(N)$ in x_i. $c(N)$ is called the complexity counter that approaches an ultimate value as N gets closer to infinity, i. e. $c(N) = O(b(N))$ and $b(N) = \log_2 N$. 3. Computing the normalized information measure $C_k(N) = c(N)/b(N) = c(N)/\log_2 N$. $C_k(N)$ ranges between 0 and 1 for a nonlinear time series, but it can also be much greater than 1 (Kovalsky et al. 2018).

Kolmogorov complexity spectrum

The complexity of a system is hidden in its dynamics. The only information available about a physical state is found in time series; therefore, a time series is the only source for establishing the level of *complex physicality*. This term usually refers to the level of complexity and interconnectivity within a complex physical system. *Physical complexity* refers to the intricate and multifaceted nature of an object's or a system's physical characteristics. It encompasses various physical attributes and behaviors that contribute to the overall complexity. Two methods are available for obtaining the time series: measurement and simulation. Regarding the former, the exact states of an observed physical system are translated into a sequence of symbols. This process is described by a parameterized partition of the state space M_ε, consisting of cells of size ε that are sampled at each time sample point τ. A measurement sequence consists of the successive elements M_ε visited over time by the system's state. Using the instrument $\{M_\varepsilon, \varepsilon\}$, we get information as a sequence of states $\{x_i\}$. Here, we consider a possible way to calculate the level of complex physicality of the system, i. e. the complexity of the time series that represents that the system is passing through different states. Connecting complex physicality with Kolmogorov complexity, we can explore how the intricate, multifaceted nature of complex physical systems might be analyzed or described in terms of their informational content and computational complexity.

Def. 1 We call the time series $\{x_i\}$, $i = 1,2,3, \dots, N$ a normalized one (or a time series with normalized amplitude) after the transformation $x_i = (X_i - X_{min})/(X_{max} - X_{min})$, where $\{X_i\}$, $i = 1,2,3, \dots, N$ is a time series obtained either by a measurement procedure or as an output of a physical model, $X_{min} = min\{X_i\}$ and $X_{max} = max\{X_i\}$.

Remark. From Def. 1 it follows that all elements of the time series $\{x_i\}$ are in the interval [0,1].

Def. 2. If the LZA algorithm is applied N times to a time series $\{x_i\}$, using all the elements of $\{x_i\}$ as thresholds $\{x_{tr,i}\}$ forming the sequence $\{c_i\}$, $i = 1,2,3, \dots, N$ then we will call the sequence $\{c_i\}$ the Kolmogorov complexity spectrum of a time series $\{x_i\}$.

Remark. The time series $\{x_i\}$ is transformed into a string of finite symbols by comparison with a series of thresholds $\{x_{tr,i}\}$, $i = 1,2,3, \dots, N$, where each element is equal to the corresponding element in the time series , applying the LZA algorithm. The original time series samples are converted into a set of 0–1 sequence $\{S_i^{(k)}\}$, $i = 1,2,3, \dots, N$, $k = 1,2,3, \dots, N$ defined by comparison with a threshold $x_{tr,k}$,

$$S_i^{(k)} = \begin{cases} 0 & x_i < x_{tr,k} \\ 0 & x_i \geq x_{tr,k} \end{cases}. \quad (1)$$

After applying the LZA algorithm to each element of the series $\{S_i^{(k)}\}$, we get the KC *complexity spectrum* $\{c_i\}$, $i = 1,2,3, \dots, N$ (fig. 1). This spectrum was introduced by (Mihailović et al. 2015) to especially examine complex systems with high complexity, i. e. those that have many stochastic components. It can provide new insights into the complexity of physical and other complex systems, their time evolution and predictability.

To clarify the meaning of the KC spectrum $\{c_i\}$, we use the following example: the time series $\{x_i\}$ is obtained by $\{M_\varepsilon, \varepsilon\} = e^{-w\sigma}$, where σ is a random number uniformly distributed in the interval [0, 1], w is the amplitude, taking values in the interval [0, 1], and $\{x_i\}$ is sampled at each time sample point $\tau = 1$. Fig. 1a shows the KC spectra for $w = 1.0$, 0.75, 0.50 and 0.25, respectively. All of the spectra have a shape that is similar to the shape of the curve in Fig. 1b, which is merely one of many possibilities due to the fact that different systems have different complexity versus randomness plots, since there is no 'universal' complexity-entropy relationship (Feldman, Crutchfield 1998). Random numbers were generated with the intrinsic subroutines CALL SEED and CALL RANDOM NUMBER (arg) from the Microsoft Fortran Developer Studio library.

 https://www.doi.org/10.33910/2687-153X-2024-5-3-146-153

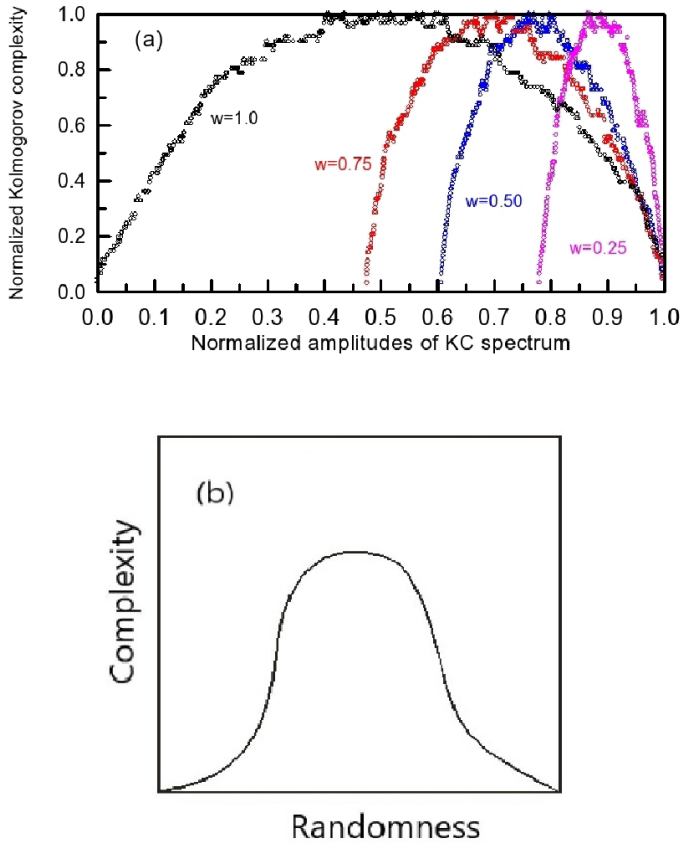

Fig. 1. (a) The normalized KC spectra $\{c_i\}$ of time series obtained by the instrument obtained $\{M_\varepsilon, \varepsilon\}$ with $\{M_\varepsilon, \varepsilon\} = e^{-w\sigma}$, where w is the amplitude factor, σ is the random number uniformly distributed in the interval [0,1], and sampling $\tau = 1$ time unit; (b) Complexity versus randomness plotted following physical intuition (Grassberger 2012)

Kolmogorov complexity plane of interacting amplitudes

A comparison of the two KC spectra is shown in Fig. 2b, which represents two merged two-dimensional graphs (with different meaning of axes): (1) KC master vs. individual components (both amplitudes are on x-axis and both complexities are on y-axis) and (2) a_M (the master amplitude) vs. a_I (individual amplitude), i. e. the KC plane. The black and red squares represent master (K_M) and individual spectra (K_I), which are calculated from the time series generated by a random generator (see the previous subsection), while the crosses indicate points in the KC plane. The quantities in these two planes were compared in the two-dimensional system (0, 1) using normalized time series. Since these quantities are on the same scale after normalization, we can assess relationships and patterns between the compared quantities without the influence of varying scales (Asesh 2022).

When we look at Fig. 2b, we see that the crosses in the (a_I, a_M) system are scattered. This is due to the dynamic relationship and interdependence between the 'master' variant and individual ones. Here, the 'master' variant characterizes the primary, overarching complexity that defines the core complexity. The greater overlapping of the KC spectra (K_I, K_M) determines the reduced scattering of points in the KC plane, approaching a linear distribution of the set of points, as shown in Fig. 2a. It can also be seen that there are two groups of points: one that belongs to the area under the K_M spectrum curve (the set S_m) and another that belongs to the area under the K_I spectrum curve (the set S_i). However, only points from the set S_p defined as

$$S_p = S_m \cap S_i \tag{2}$$

are candidates for comparison of the complexity of different sequences or systems (in this case, the entire complex physical system and its components). The amplitudes that belong to this set will conditionally

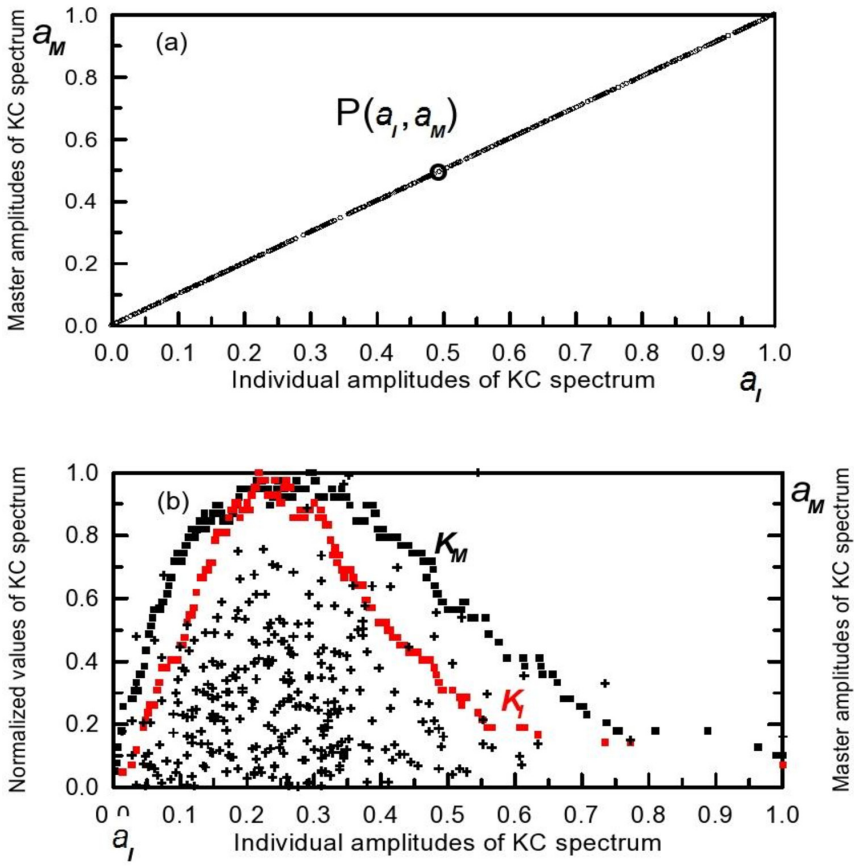

Fig. 2. (a) Towards the Kolmogrov complexity plane (KC plane); (b) The values of amplitudes of the master and individual KC spectra that are set along a_M and a_I axes (crosses), respectively. KC spectra of the entire system (K_M, black squares) and its component (K_I, red squares) were calculated from the time series generated by a random generator (see the previous subsection)

be called *interactive amplitudes*. Analyzing Fig. 2b, we can draw a crucial conclusion as follows: interplaying master and individual interactive components are most pronounced in the domains (0.05, 0.8) for master amplitudes and (0.05, 0.6) for the individual components. Perhaps more precisely stated, individual interactive amplitudes in the domain (0.17, 0.32) contribute most to the complexity of the overall system across the entire interval (0.05, 0.8) of master interactive amplitudes.

Numerical examples

Precipitation is a complex physical system par excellence. Precipitation and its formation are influenced by many factors and processes: temperature, humidity, pressure, atmospheric conditions, cloud formation, condensation of water vapor into droplets or ice crystals, falling of these particles to the ground as rain, snow, sleet, or hail, geography, topography, wind and air masses. So, the prediction of precipitation events by models of different scales is a hard task because of the difficulties in understanding these interconnected influencing factors. We use the KC plane of interacting amplitudes and two time series of precipitation: monthly precipitation simulated by a climate model and daily participation measured over twenty years (Fig. 3).

In the analysis of monthly time series, we use precipitation (the master amplitude) and temperature (individual amplitudes) for Novi Sad (45°15' N, 19°50' E) in Serbia, which were obtained from the EBU-POM model simulation under the A1B scenario during the period 2071–2100 (Djurdjević, Rajković 2012). Specifically, for this integration, the center of the atmospheric Eta model was at 41.5°N, 15°E, with ±19.9° boundaries in the east–west direction, ±13.0° boundaries in the north–south direction, 0.25° horizontal resolution and 32 vertical levels (with the first level at 20 m and the top level at 10 hPa). The ocean model featured 0.2 × 0.2° of horizontal resolution and 21 vertical levels. The size of the time series was N = 1560; the highest values of precipitation amount and temperature were 248.7 mm and 29.2°C,

 https://www.doi.org/10.33910/2687-153X-2024-5-3-146-153

respectively. In Fig. 3, the KC spectra of precipitation (black squares) and temperature (red squares), as well as points in the KC plane (crosses), are shown. The number of these points is 821 in the area that belongs to the area below both spectra and 739 points outside this area.

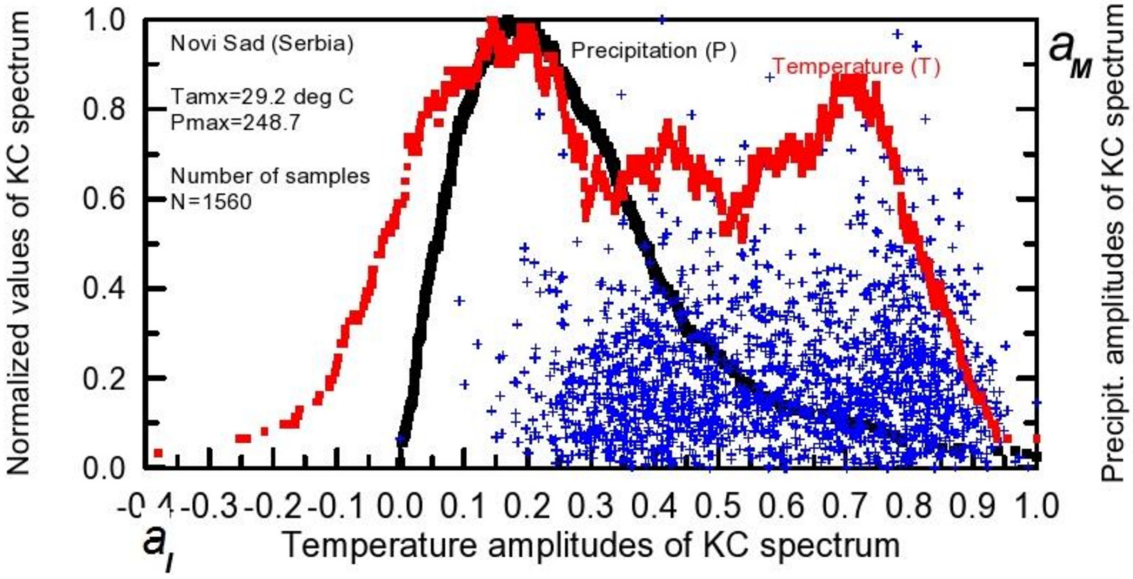

Fig. 3. KC spectra of the entire system (black squares) and its component (red squares). The values of amplitudes of the precipitation and temperature KC spectra are set along a_M and a_I axes (crosses), respectively. Monthly values of precipitation and temperature for Novi Sad (45°15' N, 19°50' E) were obtained from the EBU-POM model simulation under the A1B scenario during the period 2071–2100 (Djurdjević, Rajković, 2012)

Looking at the distribution of points in this area within the temperature amplitude interval (0.2, 0.6), it can be seen that the complexities are relatively low (0, 0.4). We can ask ourselves what quantitative conclusion we can draw from the facts presented in Fig. 3. We cannot say anything else except that the influence of interactive temperature amplitudes on precipitation complexity is observed (1) throughout the domain of these amplitudes and (2) in a narrow range of complexity (0, 0.4). Moreover, these findings seem to point towards a solution to the question of how elements of a complex physical system affect its overall complexity, which will be elaborated on later. Let us note that if the KC spectra of time series partially overlap, it could indicate that there are similarities or patterns present in the data at different levels of complexity. This could suggest that certain aspects of the data have a consistent level of complexity across different scales or resolutions. It may also indicate that there are recurring structures in the data that contribute to its overall complexity. There exist some possible interpretations of partially overlapping KC spectra for two or more time series, such as shared patterns, similar complexity profiles, overlapping generative mechanisms and non-random similarities. Some potential applications of this concept include time series clustering, anomaly detection and feature extraction (Fig. 4).

In this paper, we make feature extraction of the interactive amplitudes in the KC plane by detecting the points $(\boldsymbol{a}_I, \boldsymbol{a}_M)$ that belong to the area(s) below the overlapping KC spectra in that plane. Note that all compared time series were normalized with their highest values. This procedure allowed us to establish how the complexity of individual components of a complex physical system contributed to the overall complexity. This will be demonstrated using precipitation as a complex physical system (the overall complexity) and temperature and water vapor pressure (the complexity of components). Note that this comparison is only possible if all-time series have the same length. Daily values of precipitation, temperature and water vapor pressure for Banatski Karlovac (45°2' N, 21°1'E), averaged over the period 1986–2005, were taken from the Daily Reports of the Hydrometeorological Service of Serbia. Due to the length of the time series ($\boldsymbol{N}$ = 14610) in Fig. 4, points are not shown as in Fig. 3, which would make the graph unclear.

Fig. 4 shows the areas of influence of the complexity of components on the overall complexity: (1) red spectrum–green line–$\boldsymbol{a}_I$ axis–green line; (2) green line–blue spectrum–black spectrum; (3) blue spectrum–$\boldsymbol{a}_I$axis–green line; (4) green line–$\boldsymbol{a}_I$ axis–black spectrum; and (5) entire area above the curve of the black spectrum. Translating the position of points in these areas into the statement influence

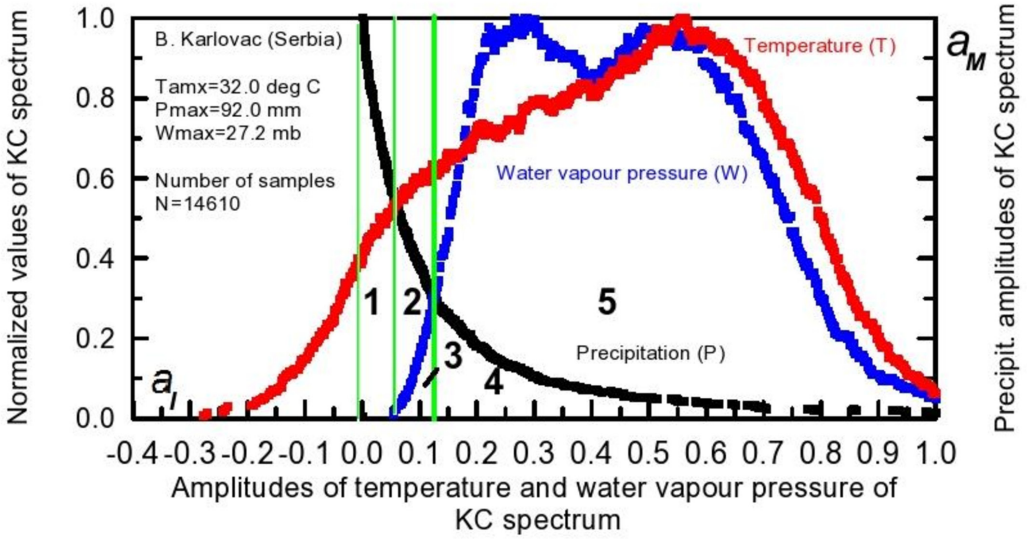

Fig. 4. KC spectra of the entire physical complex system (black squares) and its components (red and blue squares). The values of amplitudes of precipitation, temperature and KC spectra are set along the a_M and a_I axes. Areas of influence of complexity of components on the overall complexity: red spectrum–green line–a_I axis–green line (1); green line–blue spectrum–black spectrum (2); blue spectrum–a_I axis–green line (3); green line–a_I axis–black spectrum (4); and the entire area above the curve of the black spectrum (5) (for more explanation see the text). Daily values of precipitation, temperature and water vapor pressure for Banatski Karlovac (45°2' N, 21°1'E), averaged over the period 1986–2005, were taken from the Daily Reports of the Hydrometeorological Service of Serbia

of the complexity of individual components on the overall complexity, we can see (1) only the influence of temperature (0, 0.05); (2) only the influence of water vapor pressure; (3) no influence of temperature or water vapor pressure; (4) the influence of both components (temperature and water vapor pressure (0.12, 1)); and (5) no influence of the complexity of any individual component. It can be said that the KC plane allows us to determine the intervals of interacting amplitudes in which the contribution of the complexity of individual components to the overall complexity can be established. In other words, the contribution of component complexity to overall system complexity is not constant but varies with its interactive amplitudes. This means the interactivity of components with the system changes with component amplitude. This approach has important implications for (i) theory and modelling of complex systems (particularly in the segment that is related to interconnectivity of system components) and (ii) environmental and other physical complex system models having a huge practical application.

Conclusions

We considered the influence of complexity of individual components of a physical complex system on the overall complexity through the following steps: (i) we proposed Kolmogorov complexity plane of interactive amplitudes whose point coordinates (KC plane) were derived based on Kolmogorov complexity spectrum (KC spectrum); and (ii) we selected two time series encompassing the monthly time series of precipitation and temperature simulated by the EBU-POM climate model over the 1971–2100 period (Novi Sad, Serbia), and the measured daily time series of precipitation, temperature and humidity, averaged for the 1986–2005 period), for Banatski Karlovac (Serbia). All-time series were normalized using their highest values.

We calculated: (i) normalized KC spectra for all-time series; (ii) positions of points in the KC plane (interactive master amplitudes vs. interactive individual amplitudes); we made feature extraction of the interactive amplitudes in the KC plane by detecting the points lying in the areas which are below the overlapping KC spectra in that plane.

From the overlapping areas in the Kolmogorov plane, we determined the intervals of interacting amplitudes in which the contribution of complexity of individual components to overall complexity can be observed.

 https://www.doi.org/10.33910/2687-153X-2024-5-3-146-153

Conflict of Interest

The authors declare that there is no conflict of interest, either existing or potential.

Acknowledgment

The authors are grateful to Professor Darko Kapor and Master of Science Anja Mihailović for carefully reading the paper and providing useful comments.

References

Anderson, P. W. (1972) More is different: Broken symmetry and the nature of the hierarchical structure of science. *Science*, 177 (4047), 393–396. https://doi.org/10.1126/science.177.4047.393 (In English)

Asesh, A. (2022) Normalization and bias in time series data. In: C. Biele, J. Kacprzyk, W. Kopeć et al. (eds.). *Digital interaction and machine intelligence*. Cham: Springer Publ., pp. 88–97. https://doi.org/10.1007/978-3-031-11432-8_8 (In English)

Bedau, M. A. (1997) Weak emergence. *Noûs*, 31, 375–399. (In English)

De Wolf, T., Holvoet, T. (2005) Emergence versus self-organization: Different concepts but promising when combined. In: S. A. Brueckner, G. Di Marzo Serugendo, A. Karageorgos, R. Nagpal (eds.). *Engineering self-organising systems: Methodologies and applications*. Berlin; Heidelberg: Springer Publ., pp. 1–15. (In English)

Djurdjević, V., Rajković, B. (2012) Development of the EBU-POM coupled regional climate model and results from climate change experiments. In: D. T. Mihailović, B. Lalić (eds.). *Advances in environmental modeling and measurements*. New York: Nova Science Publ., pp. 23–32. (In English)

Estrada, E. (2023) What is a complex system, after all? *Foundations of Science*. https://doi.org/10.1007/s10699-023-09917-w (In English)

Feldman, D. P., Crutchfield, J. P. (1998) Measures of statistical complexity: Why? *Physics Letters A*, 238 (4–5), 244–252. https://doi.org/10.1016/S0375-9601(97)00855-4 (In English)

Gell-Mann, M., Lloyd, S. (1996) Information measures, effective complexity, and total information. *Complexity*, 2 (1), 44–52. https://doi.org/10.1002/(SICI)1099-0526(199609/10)2:1%3C44::AID-CPLX10%3E3.0.CO;2-X (In English)

Girvin, S. M., Yang, K. (2019) *Modern Condensed Matter Physics*. Cambridge: Cambridge University Press, 714 p. (In English)

Grassberger, P. (2012) *Randomness, information, and complexity*. Available at: https://arxiv.org/abs/1208.3459 (accessed 10.03.2024). (In English)

Hanel, R., Thurner, S. (2013) Generalized (c, d)-entropy and aging random walks. *Entropy*, 15 (12), 5324–5337. https://doi.org/10.3390/e15125324 (In English)

Kaspar, F., Schuster, H. G. (1987) Easily calculable measure for the complexity of spatiotemporal patterns. *Physical Review A*, 36 (2), 842–848. https://doi.org/10.1103/PhysRevA.36.842 (In English)

Kolmogorov, A. N. (1965) Tri podkhoda k opredeleniyu ponyatiya "kolichestvo informatsii" [Three approaches to the quantitative definition of information]. *Problemy Peredachi Informatsii*, 1 (1), 3–11. (In Russian)

Kovalsky, M. G., Hnilo, A. A., Agüero, M. B. (2018) Kolmogorov complexity of sequences of random numbers generated in Bell's experiments. *Physical Review A*, 98 (4), article 042131. https://doi.org/10.1103/PhysRevA.98.042131 (In English)

Lempel, A., Ziv, J. (1976) On the complexity of finite sequences. *IEEE Transactions on Information Theory*, 22 (1), 75–81. https://doi.org/10.1109/TIT.1976.1055501 (In English)

Mihailović, D. T., Mimić, G., Nikolić-Đorić, E., Arsenić, I. (2015) Novel measures based on the Kolmogorov complexity for use in complex system behavior studies and time series analysis. *Open Physics*, 13 (1), 1–14. https://doi.org/10.1515/phys-2015-0001 (In English)

Mihailović, D., Kapor, D., Crvenković, S., Mihailović, A. (2023) *Physics of complex systems: Discovery in the age of Gödel*. Boca Raton: CRC Press, 200 p. (In English)

The Nobel Prize in Physics 2021. (2021) The Nobel Prize. [Online]. Available at: https://www.nobelprize.org/prizes/physics/2021/summary/ (accessed 10.03.2024). (In English)

Thurner, S., Hanel, R., Klimek, P. (2018) *Introduction to the theory of complex systems*. Oxford: Oxford University Press, 448 p. (In English)

Welch, T. A. (1984) A technique for high-performance data compression. *Computer*, 17 (6), 8–19. https://doi.org/10.1109/MC.1984.1659158 (In English)

Theoretical physics.
Cosmology

UDC 524.8

EDN WWBQPT
https://www.doi.org/10.33910/2687-153X-2024-5-3-154-166

Black hole shadow: Experimental test of different models and shadow of dynamical Hayward black hole

V. D. Vertogradov [✉1, 2], A. V. Shakun [1], M. A. Zakharov [1]

[1] Herzen State Pedagogical University of Russia, 48 Moika Emb., Saint Petersburg 191186, Russia
[2] SPb branch of SAO RAS, 65 Pulkovskoe Highway, Saint Petersburg 196140, Russia

Authors

Vitalii D. Vertogradov, ORCID: 0000-0002-5096-7696, e-mail: vdvertogradov@gmail.com

Alina V. Shakun, ORCID: 0009-0007-4550-6549, e-mail: shakun1410@mail.ru

Mark A. Zakharov, ORCID: 0009-0003-1753-5239, e-mail: jozzeph17@gmail.com

For citation: Vertogradov, V. D., Shakun, A. V., Zakharov, M. A. (2024) Black hole shadow: Experimental test of different models and shadow of dynamical Hayward black hole. *Physics of Complex Systems*, 5 (3), 154–166. https://www.doi.org/10.33910/2687-153X-2024-5-3-154-166 EDN WWBQPT

Received 9 July 2024; reviewed 19 July 2024; accepted 19 July 2024.

Funding: The study did not receive any external funding.

Abstract. Recent observations of black hole shadows have revolutionized our ability to probe gravity in extreme environments. This manuscript presents a novel analytic model of the shadow of a dynamical Hayward black hole. We show that under some choice of mass and regularization functions, this spacetime admits a homothetic Killing vector, which allows the reduction of the second-order differential equations of motion to the first-order ones. After that, we introduce the coordinate transformation to conformally-static coordinates and introduce a new conserved quantity along null geodesics. We prove that in the dynamical case the regularization parameter always decreases the radius of a photon sphere. Inspired by the experimental data obtained by the Event Horizon Telescope Collaboration, we compare the obtained images of Sagittarius A^* with a black hole shadow in Reissner–Nordstrom, Bardeen and Hayward black holes, respectively.

Keywords: black hole, photon sphere, mass-dependent, shadow, dynamical Hayward black hole

Introduction

In 1915, Albert Einstein presented general relativity. One year later, Schwarzschild solved his equations for empty spherically-symmetric spacetime, and his solution became known as Schwarzschild metric. Later, it was understood that Schwarzschild spacetime describes a static spherically-symmetric black hole. However, a black hole distorts spacetime so strongly that even light cannot escape it. That is why one can learn about properties of a black hole through its influence on surrounding matter. For this reason, it becomes really important to study the properties of motion around these objects. Thorough investigation of light propagation revealed that light can move along an unstable circular orbit which forms a black spot on the observer's sky, which is known as a black hole shadow (Bardeen et al. 1972; Synge 1966;).

In 2019, the Event Horizon Telescope Collaboration published images of the supermassive black hole located in the center of galaxy $M87$ (Alberdi et al. 2019). Later, in 2022, they published images of a supermassive black hole, Sagittarius A^*, in our own galaxy — Milky Way (Akiyama et al. 2022). These observation data endowed a black hole with the status of a real astrophysical object and drew huge attention of the scientific community.

The idea that this shadow could be observed was brought forward in 2000 in a pioneering paper by Falcke et al. (Falcke et al. 2000). Tsupko et al. showed that a shadow can be used as a cosmological ruler (Tsupko et al. 2020). The problem of using the shadow as a cosmological ruler is discussed in the paper (Vagnozzi et al. 2020). The black hole shadow can be used to distinguish different black hole models and even to find differences between general relativity and alternative theories of gravity (Vagnozzi et al. 2023). The review of an analytical study of static black hole shadows is given in (Perlick, Tsupko 2022). The influence of plasma on the observed size of a black hole is considered in the paper (Perlick et al. 2015). New analytical methods of studying black hole shadows have been developed in papers (Vertogradov, Övgün 2024a; 2024b; Vertogradov et al. 2024). However, all these models describe the static black hole; the astrophysical black hole, however, changes its mass while absorbing and emitting matter. Thus, the real black hole should be described by dynamical spacetime. There is a numerical method of calculating a dynamical black hole shadow developed in (Koga et al. 2022; Mishra et al. 2019), but analytical models are scarce (Heydarzade, Vertogradov 2024; Solanki, Perlick 2022; Tsupko, Bisnovatyi-Kogan 2020). The problem with an analytical model is that there is only one conserved quantity in the spherically symmetric black hole spacetime. It is an angular momentum-per-mass L. So, one needs to seek extra symmetry to reduce the second-order differential equations of motion to the first one. Dynamical spacetime does not possess the timelike Killing vector $\frac{\partial}{\partial t}$, so one should look for conformal Killing vectors. If the spacetime admits the conformal Killing vector, then there is an extra conserved quantity along null geodesics. The shadow formation in Vaidya and charged Vaidya spacetime has been investigated in the papers (Heydarzade, Vertogradov 2024; Solanki, Perlick 2022). Vaidya solution (Vaidya 1951) is one of the exact dynamical solutions of the Einstein equations. It can be regarded as a dynamical generalization of the static Schwarzschild solution. The Vaidya spacetime is widely used in many astrophysical applications with strong gravitational fields. In general relativity, this spacetime assumed greater importance with the completion of the junction conditions at the surface of the star by Santos (Santos 1985). The horizon structure and surface gravity of this solution have been investigated in (Nielsen 2014, Nielsen, Yoon 2008). The Vaidya spacetime can be extended to include both null dust and null string fluids leading to the generalized Vaidya spacetime (Wang, Wu 1999). A detailed investigation of the properties of the generalized Vaidya spacetime can be found in (Glass, Krisch 1998; Glass, Krisch 1999; Husain 1996; Vertogradov 2024). Charged Vaidya spacetime (Bonnor, Vaidya 1970) has been widely investigated in gravitational collapse and naked singularity formation (Beesham, Ghosh 2003; Lake, Zannias 1991; Patil et al. 1999; Vertogradov 2022;). The conformal symmetry of the charged Vaidya spacetime and Hawking radiation have been considered in (Ibohal, Kapil 2010; Koh et al. 2024; Ojako et al. 2020; Vertogradov, Kudryavcev 2023). Surrounded Vaidya spacetimes with cosmological fields have been obtained in papers (Heydarzade, Darabi 2018a; Heydarzade, Darabi 2018b; Heydarzade, Darabi 2018c). The process of extracting energy from the charged Vaidya black hole has been considered in (Vertogradov 2023).

In this paper, we compare experimental images obtained by the Event Horizon Telescope Collaboration from Sagittarius A^* with well-known black hole models, i. e. the electrically charged black hole described by Reissner — Nordstrom spacetime and two regular black holes described by Bardeen and Hayward metrics. Then we show that there are several values of extra parameters under which a shadow corresponds to experimental data. We also present the shadow model of a dynamical Hayward regular black hole. We consider the linear mass and regularization functions because Hayward spacetime with these choices of functions admits a homothetic Killing vector. We introduce the coordinate transformation to the conformally static coordinates in which we introduce an extra conserved quantity and estimate the influence of the regularization parameter on the visible size of a shadow.

This paper is organized as follows: in Section 2 we briefly describe the method of black hole shadow calculation and numerically calculate the shadow for Reissner — Nordstrom, Bardeen and Hayward spacetimes. Then we compare the obtained shadow with the image of Sagittarius A^*. In Section 3 we analytically calculate the radius of the photon sphere in dynamical Hayward spacetime and estimate the influence of the regularization parameter on it. Section 4 discusses the obtained results.

The geometrized system of units $c = 1 = G$ will be used throughout the paper. We also use the signature $-+++$.

Shadow of spherically-symmetric black holes

Astrophysical black holes are supposed to be rotational. The shadow of these objects depends on the angle of observation. However, if an observer sees the shadow along the rotational axis, then the shadow

has the same form and properties as a static spherically-symmetric one. For this reason, we compare images obtained by the Event Horizon Telescope Collaboration with several well-known solutions of the Einstein field equations describing non-rotational black holes. Without loss of generality, the spherically symmetric spacetime can be written as

$$ds^2 = -fdt^2 + f^{-1}dr^2 + r^2 d\Omega^2, \tag{1}$$

where $f \equiv f(r)$ is the lapse function and $d\Omega^2 = d\theta^2 + \sin^2\theta d\varphi^2$ is the metric on the unit two-sphere. The spacetime (1) admits two constants of motion, i. e. energy-per-mass E and angular momentum-per-mass L which are given by the equatorial plane $\theta = \frac{\pi}{2}$

$$E = f\frac{dt}{d\lambda},$$
$$L = r^2\frac{d\varphi}{d\lambda}, \tag{2}$$

where λ is an affine parameter. By using the null geodesic condition $g_{ik}u^i u^k = 0$, one can write the radial component of the geodesic motion equation as

$$\left(\frac{dr}{d\lambda}\right)^2 + V_{eff} = 0,$$
$$V_{eff} = L^2\frac{f}{r^2} - E^2. \tag{3}$$

Here V_{eff} has effective potential. A black hole shadow is formed by a photon sphere, which is composed of unstable circle orbits. For a circle orbit, there are two conditions $\frac{dr}{d\lambda} = \frac{d^2r}{d\lambda^2} = 0$ which lead to

$$V_{eff}(r_{ph}) = 0,$$
$$V'_{eff}(r_{ph}) = 0, \tag{4}$$

where r_{ph} is the radius of a photon sphere and prime denotes the radial derivative. For Schwarzschild spacetime, i. e.

$$f(r) = 1 - \frac{2M}{r}, \tag{5}$$

the radius of a photon sphere $r_{ph} = 3M$. The radius of a shadow is defined from the first condition (4)

$$b \equiv \frac{L}{E} = \frac{r_{ph}}{\sqrt{f(r_{ph})}}, \tag{6}$$

where b is an impact parameter. For a Schwarzschild black hole, it has the value of $b = 3\sqrt{3}M$. The angular size ω_{sh} of a shadow is given by

$$\sin^2\omega_{sh} \approx \frac{b^2}{r_o}, \tag{7}$$

where r_0 is the distance between an observer and a black hole. The angular size ω_{sh} of a Schwarzschild black hole for a Sagittarius a^* is ~53μ as. However, the observational data shows that the real angular size of Sagittarius a^* is ~52μ as. This indicates that one should consider black hole models different from Schwarzschild ones. It is a well-known fact that the electrical charge of a black hole decreases its angular size. The metric that describes an electrically charged black hole is Reissner–Nordstrom spacetime

$$f(r) = 1 - \frac{2M}{r} + \frac{Q^2}{r^2}, \tag{8}$$

where Q is an electrical charge of a black hole with dimension of length. The radius of a photon sphere in this case is

 https://www.doi.org/10.33910/2687-153X-2024-5-3-154-166

$$r_{ph} = \frac{1}{2}\left(3M + \sqrt{9M^2 - 8Q^2}\right). \tag{9}$$

As one can see that if $Q \to 0$, then we obtain the radius of a photon sphere like in Schwarzschild spacetime $r_{ph} = 3M$. However, if one considers other spacetimes, like regular Bardeen (Bardeen 1968) and Hayward (Hayward 2006) ones, which are given by

$$f(r) = 1 - \frac{2Mr^2}{(r^2 + g^2)^{\frac{3}{2}}} \tag{10}$$

and

$$f(r) = 1 - \frac{2Mr^2}{r^3 + 2ML^2} \tag{11}$$

respectively, then one will see that it is impossible to find exact analytical expression for the radius of a photon sphere and angular size. However, by using the method developed in (Vertogradov, Övgün 2024a), one can estimate the influence of parameters g and L on the angular size of a black hole. To use this method, we write the lapse function in the form

$$f = \left(1 - \frac{2M}{r}\right)e^{\xi(r)}, \tag{12}$$

where ξ is a small arbitrary function. If $\xi'(3M) < 0$, then minimal geometrical deformation decreases the radius of a photon sphere, and if $\xi(3M) > 0$, then the angular size of a black hole shadow decreases. In the paper (Vertogradov, Övgün 2024b) it was shown that parameters g in Bardeen spacetime (10) and L in Hayward spacetime (11) decrease the angular size of a black hole shadow. It means we should find such values Q, g and L that the shadow size is ~52μ as.

Now let us look at the effectiveness of the presented models. Let us calculate the angular size of the shadow of the black holes M87* and Sgr A*.

Schwarzschild black hole

As it is known, the radius of the shadow of a black hole is

$$V_{eff}(r_{ph}) = 0 \to \frac{\mathcal{L}^2}{r_{ph}^2}A(r_{ph}) - E^2 = 0 \to \frac{b^2}{r_{ph}^2}A(r_{ph}) - 1 = 0. \tag{13}$$

Let us consider the shadow of a spherically symmetric Schwarzschild black hole. Then the metric has the form:

$$ds^2 = -\left(1 - \frac{2M}{r}\right)dt^2 + \left(1 - \frac{2M}{r}\right)dr^2 + r^2 d\Omega^2. \tag{14}$$

Substituting the value into the effective potential, we get

$$V_{eff} = \left(1 - \frac{2M}{r}\right)\frac{L^2}{r^2} - E^2. \tag{15}$$

When substituting the condition, we get:

$$\frac{dV_{eff}}{dr} = 0 \to A' - 2A = \frac{2M}{r} - 2 + \frac{4M}{r} = 0 \to r_{ph} = 3M. \tag{16}$$

Thus, substituting the radius into the condition and resolving with respect to the impact parameter, we get:

$$V_{eff} = 0 \to \left(1 - \frac{2M}{r}\right)\frac{L^2}{r^2} - E^2 = 0 \to$$
$$\left(1 - \frac{2M}{r}\right)\frac{b^2}{r^2} - 1 = 0 \to b_{cr} = 3\sqrt{3}M. \quad (17)$$

Experimental data have shown that the mass of SqrA* is equal to $4.3 \times 10^6 M_o$, and M87* — $3 \times 10^9 M_o$. Mass and charge are included in a geometrized system of units, that is, in a system in which G and c are equal to 1. Accordingly, they have a dimension in centimeters. To convert kilograms and pendants into centimeters, we need to use the following formula:

$$m = \frac{GM}{c^2}. \quad (18)$$

Substituting the values, we find that the mass of the black hole SgrA* corresponds to

$$M = 6 \times 10^{11} g, \quad (19)$$

and M87* —

$$M = 4 \times 10^{14} g. \quad (20)$$

Now let us convert r_0 to centimeters; then for SgrA* it will be equal to

$$r_0 = 26 \times 10^{21} cm, \quad (21)$$

and for M87* —

$$r_0 = 56 \times 10^{24} cm. \quad (22)$$

The Schwarzschild solution is not successful, since the values are somewhat overestimated, and it is impossible to use an additional parameter to reduce the diameter. Therefore, the Schwarzschild metric is good for research as an ideal model for qualitative effects, but it is not suitable for description, and other models need to be considered.

Reissner — Nordstrom black hole

The metric is spherically symmetric and static.

In the case of Reissner–Nordstrom, this is a known quantity that can be found when solving the second equation with respect to r_{ph}. We get the following expression:

$$r_{ph} = \frac{3}{2}\left(M + \sqrt{M^2 - \frac{8}{9}Q^2}\right). \quad (23)$$

The first condition implies that

$$V_{eff}(r_{ph}) = 0. \quad (24)$$

Then we express the impact parameter b:

$$b_{cr} = \sqrt{\frac{(3M + \sqrt{9M^2 - 8Q^2})^4}{24M^2 + 8M\sqrt{9M^2 - 8Q^2} + 48Q^2}}. \quad (25)$$

To correctly estimate the angular diameter, we use the expression

$$2\alpha = \frac{b}{r_0}, \quad (26)$$

where r_0 — distance to SqrA* and M87*.

 https://www.doi.org/10.33910/2687-153X-2024-5-3-154-166

Now let us substitute the masses and r_0 of M87* and SgrA* in the expression for the angular parameters. We assume that the q, the gravitational charge, is 0.01M, 0.1M, 0.5M, 0.75M, 0.99M and get the corresponding angular sizes.

The highest values are reached at 0.01M. To understand what 0.01M is for a charge and what is a charge in centimeters, we convert the charge into coulombs according to the following formula:

$$Q^2 = \frac{q^2 G}{4\pi\varepsilon_0 c^4}. \tag{27}$$

To do this, we will use the SI-system, in which the mass is in meters and the charge is in coulombs. Thus, the value has the form

$$Q = 7 \times 10^{25}. \tag{28}$$

The charge is gigantic and corresponds to a supermassive black hole of the order of millions of solar masses.

Hayward black hole

The metric describes a regular black hole. Similary to the Reissner–Nordstrom case, we obtain an expression for the radius of the photon sphere:

$$r^6 - 3Mr^5 + 4L^2Mr^3 + 4L^4M^2 = 0. \tag{29}$$

Numerically solving it and substituting the value, we express the impact parameter b:

$$b_{cr} = \sqrt{\frac{r^5 + 2r^2ML^2}{r^3 + 2ML^2 - 2Mr^2}}. \tag{30}$$

Consider the upper bound of the range of possible values of the regularization parameter L, at which an extreme black hole occurs. The mass of the black hole must be less than or equal to zero.

As we know, the metric describing Hayward is presented as follows:

$$f(r) = 1 - \frac{2Mr^2}{r^3 + 2ML^2}. \tag{31}$$

Let us bring it to a common denominator and take the derivative in r. As a result, we take a value greater than zero:

$$r = \frac{4M}{3}. \tag{32}$$

Substituting r into the expression for the metric and solving with respect to L, we get the boundary for an extreme black hole:

$$L \leq \frac{4M}{3\sqrt{3}}. \tag{33}$$

Since at a higher value there is no horizon, or the black hole itself, and the result in the form of a shadow of a black hole is also lost, we are interested in values ranging from 0 to $\frac{4m}{3\sqrt{3}}$. The impact parameter L allows us to get the most correct result, which can be seen with L equal to 0.01M.

Bardeen black hole

The Bardeen metric also describes regular black holes.

By analogy with the previous metrics, we get the expression for r_{ph}:

$$r^{10} + (5g^2 - 9M^2)r^8 + 10g^4r^6 + 10g^6r^4 + 5g^8r^2 + g^{10} = 0. \tag{34}$$

Based on its numerical solution, we obtain the impact parameter b:

$$b_{cr} = \sqrt{\frac{r^2(r^2+g^2)^{\frac{3}{2}}}{(r^2+g^2)^{\frac{3}{2}} - 2Mr^2}}, \tag{35}$$

g — the magnetic charge of the monopole characterizing the current model. Let us find its upper bound.

Bardeen's metric:

$$f(r) = 1 - \frac{2Mr^2}{(r^2+g^2)^{\frac{3}{2}}}. \tag{36}$$

We bring it to a common denominator and take the derivative of r in the same way as Hayward. We get two roots, and by solving one of them we come to the following value:

$$r = \sqrt{\frac{16M^2 - 9g^2}{9}}. \tag{37}$$

Substituting the result into the Bardeen metric, we find g:

$$g \leq \frac{4M}{3\sqrt{6}}. \tag{38}$$

Iterating through the values in the range from 0 to $\frac{4m}{3\sqrt{6}}$, we get the results.

Since the charge is small, as for Reissner–Nordstrom, they differ little from each other. Nonlinear electrodynamics was introduced to describe powerful electric fields.

Table 1. Experimental data

Schwarzschild	–	–	–
M87*	18	–	–
SgrA*	53	–	–
Reissner–Nordstrom	Q = 0.01m	Q = 0.1m	Q = 0.99m
M87*	17	16	6
SgrA*	53	52	19
Hayward	L = 0.01m	L = 0.1m	$L_{max} = \frac{4m}{3\sqrt{3}}$
M87*	17	17	16
SgrA*	52	52	48
Bardeen	G = 0.01m	G = 0.1m	$G_{max} = \frac{4m}{3\sqrt{6}}$
M87*	17	17	16
SgrA*	52	52	44

 https://www.doi.org/10.33910/2687-153X-2024-5-3-154-166

Shadow of a dynamical Hayward black hole

Properties of the Hayward metric

In the general case, the metric for a regular black hole is written as:

$$ds^2 = -F(r)dt^2 + \frac{dr^2}{F(r)} + r^2 d\Omega^2. \tag{39}$$

In the article (Hayward 2006) Hayward introduced $F(r)$ as $F(r) = (1 - \frac{2Mr^2}{r^3+2ML^2})$. Here, if the regularization parameter L tends to zero, Hayward spacetime becomes a Schwarzschild one. This L prevents scalar invariants from divergence at $r \to 0$. Hayward spacetime at $r \to 0$ has de Sitter core.

$$F(r) \sim 1 - \frac{M}{r}, r \to \infty$$
$$F(r) \sim 1 - \frac{r^2}{L^2}, r \to 0\ . \tag{40}$$

A black hole without singularity in the center is called a regular black hole, and the Hayward black hole is one of the examples of models of such black holes. Let us write down Hayward metric and define some characteristics:

$$ds^2 = -\left(1 - \frac{2Mr^2}{r^3 + 2ML^2}\right)dt^2 + \frac{dr^2}{\left(1 - \frac{2Mr^2}{r^3 + 2ML^2}\right)} + r^2 d\Omega^2. \tag{41}$$

First of all, we should show that the metric is really regular. For this purpose, we calculate Kretschmann scalar:

$$K = \frac{24}{L^4}\left(1 - \frac{r^3}{ML^2}\right). \tag{42}$$

From this, we can see that $r \to 0$, which corresponds to the center of a black hole, does not lead to a divergence of scalar invariants and the emergence of a singularity. Another important property of the metric is that a black hole has two horizons — the inner and the outer one.

Under some values of M and L this black hole becomes an extremal one, i. e. these two horizons merge. This means that the Hayward metric can describe an extreme black hole. Formation of an extreme black hole is possible under the following conditions: $M = \frac{3\sqrt{3}}{4}L$.

The shadow of a Hayward black hole

In order to describe a black hole shadow, one needs to find a photon sphere. For this purpose we need to find a solution at which photons move in a circular orbit in the black hole potential. The Lagrangian for the metric (41) has the following form:

$$\mathfrak{L} = \frac{1}{2}\left[-\left(1 - \frac{2Mr^2}{r^3 + 2ML^2}\right)\frac{dt^2}{d\lambda^2} + \left(1 - \frac{2Mr^2}{r^3 + 2ML^2}\right)\frac{dr^2}{d\lambda^2} + r^2\frac{d\Omega 2}{d\lambda^2}\right]. \tag{43}$$

Using this Lagrangian, we can find the effective potential V_{eff}:

$$V_{eff} = E^2 - \left(1 - \frac{2Mr^2}{r^3 + 2ML^2}\right)\frac{\mathcal{L}}{r^2}. \tag{44}$$

From (44) and the condition for the existence of circular orbits, we have an expression for the shadow of the Hayward black hole:

$$r^6 - 3Mr^5 + 4L^2Mr^3 + 4L^4M^2 = 0. \tag{45}$$

It is easy to see that if we put $L = 0$, the radius of a photon sphere becomes the Schwarzschild one $r_{ph} \to 3M$.

Dynamical shadow of the Hayward black hole

In the previous subsection, we described the static model. In the static case, the effects associated with accretion and radiation are not taken into account, which is well suited for a superficial study of the model and properties of the black hole. However, for a deeper understanding of this object, it is necessary to set a task closer to reality. The obtained experimental data are based on the fact that telescopes detect X-ray emission, which is caused by the friction of the plasma that forms the accretion disk, and the model has to be improved to take into account the effects associated with the accretion of matter.

We use the Eddington–Finkelstein coordinates $\{v, r, \theta, \varphi\}$, in which the Hayward spacetime takes the form:

$$ds^2 = -\left(1 - \frac{2M(v)r^2}{r^3 + 2M(v)L(v)^2}\right)dv^2 + 2dvdr + r^2 d\Omega^2. \tag{46}$$

Since the components of the metric tensor are time-dependent, a time-like Killing vector does not exist, and the solution becomes analytically difficult since the energy is not conserved. To simplify the task, we need to carry out conformal transformations. In the paper (Nielsen 2014) it was proven that the existence of a conformal Killing vector is possible with the following choice of mass and regularization functions:

$$\begin{aligned} M(V) &= \mu v, \\ L^2(v) &= \alpha\xi^2 v^2. \end{aligned} \tag{47}$$

By introducing these transformations into the metric, we obtain:

$$ds^2 = -\left(1 - \frac{2\mu v r^2}{r^3 + 2\mu\alpha\xi^2 v^3}\right) + 2dvdr + r^2\Omega^2. \tag{48}$$

We also make coordinate transformation:

$$\begin{aligned} v &= r_0 \exp\left(\frac{T}{r_0}\right), \\ r &= R exp\left(\frac{T}{r_0}\right). \end{aligned} \tag{49}$$

Then considering (48) and (49), we get:

$$\begin{aligned} ds^2 &= \exp\left(\frac{2T}{r_0}\right)ds_1^2, \\ ds_1^2 &= -\left(1 - \frac{2\mu r_0 R^2}{R^3 + 2\mu\alpha\xi^2 r_0^3} - \frac{2R}{r_0}\right)dT^2 + 2dTdR + R^2 d\varphi^2. \end{aligned} \tag{50}$$

Based on the obtained data we can write down the effective potential in the form:

$$V_{eff} = \left(1 - \frac{2\mu r_0 R^2}{R^3 + 2\mu\alpha\xi^2 r_0^3} - \frac{2R}{r_0}\right)\frac{L^2}{R^2} - E^2. \tag{51}$$

This expression has a complex analytical form. For simplicity, we note that we can perform the following substitutions:

$$\frac{2\mu r_0 R^2}{R^3 + 2\mu\alpha\xi^2 r_0^3} = \frac{2\mu r_0}{R} - \varepsilon(R). \tag{52}$$

This leads to the fact that the *F(R)* is reduced to the form:

 https://www.doi.org/10.33910/2687-153X-2024-5-3-154-166

$$1-\frac{2\mu r_0}{R}-\varepsilon(R)-\frac{2R}{r_0}. \tag{53}$$

And as we know (Heydarzade, Vertogradov 2024), $1-\frac{2\mu r_0}{R}-\frac{2R}{r_0}$ is F(R) for dynamic Vaidya spacetime. And we can describe the effective potential as the sum of two components, F(R) for Vaidya spacetime and $\varepsilon(R)$. Then we need to find $\varepsilon(R)$:

$$\begin{aligned}\varepsilon(R) &= -\frac{2\mu r_0 R^2}{R^3+2\mu\alpha\xi^2 r_0^3}+\frac{2\mu r_0}{R}\\ &= \frac{4\mu^2\alpha\xi^2 r_0^4}{R^4+\mu\alpha\xi^2 r_0^3 R}.\end{aligned} \tag{54}$$

From (53) and (54) we can find the effective potential V_{eff} as:

$$V_{eff}=\left(1-\frac{2\mu r_0}{R}-\frac{2R}{r_0}+\frac{4\mu^2\alpha\xi^2 r_0^4}{R^4+\mu\alpha\xi^2 r_0^3 R}\right)\frac{L^2}{R^2}-E^2. \tag{55}$$

It follows that the radius of the photonsphere can be represented as the sum of the radius of the Vaidya photonsphere and the radius of the function $\varepsilon(R)$:

$$R_{ph}=R_V+\alpha R_\varepsilon. \tag{56}$$

Since the radius of the photon sphere in the Vaidya case is already known, we only need to find R_ε. For this purpose we write down V_{eff}:

$$V_{eff}=b^2Q(R)\big(1+\alpha Q(R)\big)-1. \tag{57}$$

Functions Q(R) and G(R) are

$$\begin{aligned}Q(R)&=\frac{\left(1-\frac{2\mu r_0}{R}-\frac{2R}{r_0}\right)}{R^2},\\ G(R)&=\frac{4\mu^2\xi^2 r_0^4}{(R^4+\alpha\mu\xi^2 r_0^3 R)}\frac{1}{\left(1-\frac{2\mu r_0}{R}-\frac{2R}{r_0}\right)}.\end{aligned} \tag{58}$$

From (24) we find:

$$Q'(R)\big(1-\alpha G(R)\big)-\alpha Q(R)G'(R). \tag{59}$$

Assuming that α is very small, we write (59) as:

$$Q''(R_0)\alpha R_1-\alpha G'(R_0)Q(R_0)=0. \tag{60}$$

Hence it follows

$$R_\varepsilon=-\frac{G'(R_0)Q(R_0)}{Q''(R0)}. \tag{61}$$

In order to find R_ε, we need to calculate functions $Q''(R)$, $G'(R)Q(R)$. To simplify the calculations, let us assume that $1-\frac{2\mu r_0}{R}-\frac{2R}{r_0}=h(R)$. Then

$$\begin{aligned}Q(R) &= \frac{h(R)}{R^2},\\ G(R) &= \frac{\varepsilon(R)}{h(R)}.\end{aligned} \tag{62}$$

From this expression we can represent the equations in a general form:

$$\begin{aligned} Q'(R) &= \frac{h'(R) - 2h(R)}{R^3}, \\ Q''(R) &= \frac{h''(R)R - h'(R)}{R^3}, \\ G'(R) &= \frac{\varepsilon'(R)h(R) - h'(R)\varepsilon(R)}{h^2(R)}. \end{aligned} \tag{63}$$

Let us use the condition that $h'(R) - 2h(R) = 0$. Then we can make the following transformations:

$$\begin{aligned} G'(R) &= \frac{\varepsilon'(R) - \frac{2}{R}\varepsilon(R)}{h(R)}, \\ Q''(R) &= \frac{h''(R) - 2h(R)}{R^4}, \\ G'Q(R) &= \frac{\varepsilon'(R) - \frac{2}{R}\varepsilon(R)}{R^2}. \end{aligned} \tag{64}$$

Then substituting (61) into (64), we find:

$$R_1 = -\frac{R^2\varepsilon'(R) - 2R\varepsilon(R)}{h''(R)R^2 - h(R)}. \tag{65}$$

And from (64) and (65) we obtain:

$$R_1 = -\frac{12\mu^2\xi^2 r_0^5}{R^4}. \tag{66}$$

Since R_ε is negative, the photonsphere radius R_{ph} will be smaller than R_V. Thus, we can conclude that the regularization parameter reduces the shadow size, which should be taken into account when obtaining experimental data.

Conclusions

The investigation of black hole shadows can give us a better understanding of these mysterious objects. It is a well-established fact that the Schwarzschild metric is good at describing some effects of the black hole, but it does not describe the real astrophysical object. For this reason, one should seek for alternative black hole models and compare them with only accessible experimental data obtained by the Event Horizon Telescope Collaboration. However, even this knowledge allows one to reject several models. Recently, it was proven that a primary hair in hairy Schwarzschild and Reissner — Nordstrom spacetimes obtained by gravitational decoupling (Ovalle et al. 2021) always increases the radius of a photon sphere. It means that we can say that hairy a Schwarzschild black hole does is not suitable for describing the black hole in the center of our galaxy. The primary hair also increases the radius of a photon sphere in a charged version of this solution. However, it can still be a suitable model which demands even more charge than Reissner — Nordstrom, though. In this paper we showed that the Reissner — Nordstrom charged black hole and the regular Bardeen and Hayward black holes might suit as models for describing the supermassive black hole Sagittarius A^* in the center of our galaxy. However, the amount of electrical charge of ~10^26 C sounds unrealistic for a real astrophysical black hole. A real astrophysical black hole is surrounded by an accretion disc. This disc has an influence on the black hole metric, and if we assume constant accretion onto the black hole, then it should change its mass. This fact tells us that the spacetime around these objects should be dynamical. However, we encounter serious problems with constructing a black hole shadow for dynamical spacetimes because in general, it does not have enough constants of motion to reduce the second-order differential equations to the first one although the first steps in this direction have been made in the paper (Vertogradov, Övgün 2024a). Thus, we should seek for extra symmetries to introduce a new conserved quantity along null geodesics. This extra symmetry can be a consequence of the existence of a conformal Killing vector. We have found conformal Killing vector

 https://www.doi.org/10.33910/2687-153X-2024-5-3-154-166

for a Hayward regular black hole and introduced a coordinate transformation to conformably-static coordinates. This allowed us to calculate a shadow for dynamical Hayward spacetime. Although a full analytical description is not possible in this spacetime, we can estimate the influence of the extra parameter L on the size of a shadow. Analytically, we were able to prove that this regularization parameter L always decreases the radius of a photon sphere and can serve as a good model for describing the supermassive black hole Sagittarius A^*.

Conflict of Interest

The authors declare that there is no conflict of interest, either existing or potential.

Author Contributions

All the authors discussed the final work and took part in writing the article.

References

Akiyama, K., Alberdi, A., Alef, W. et al. (2022) First Sagittarius A* event horizon telescope results. I. The shadow of the supermassive black hole in the center of the Milky Way. *The Astrophysical Journal Letters*, 930 (2), article L12. https://doi.org/10.3847/2041-8213/ac6674 (In English)

Alberdi, A., Alef, W., Asada, K. et al. (2019) First M87 event horizon telescope results. I. The shadow of the supermassive black hole. *The Astrophysical Journal Letters*, 875, L1. https://doi.org/10.3847/2041-8213/ab0ec7 (In English)

Bardeen, J. (1968) Non-singular general relativistic gravitational collapse. *Proceedings of the 5th International Conference on Gravitation and the Theory of Relativity*, article 87. (In English)

Bardeen, J. M., Press, W. H., Teukolsky, S. A. (1972) Rotating black holes: Locally nonrotating frames, energy extraction, and scalar synchrotron radiation. *Astrophysical Journal*, 178, 347–370. (In English)

Beesham, A., Ghosh, S. G. (2003) Naked singularities in the charged Vaidya–de Sitter spacetime. *International Journal of Modern Physics D*, 12 (5), 801–809. https://doi.org/10.1142/S0218271803003220 (In English)

Bonnor, W. B., Vaidya, P. C. (1970) Spherically symmetric radiation of charge in Einstein-Maxwell theory. *General Relativity and Gravitation*, 1, 127–130. https://doi.org/10.1007/BF00756891 (In English)

Falcke, H., Melia, F., Agol, E. (2000) The shadow of the black hole at the galactic center. *AIP Conference Proceedings*, 522 (1), 317–320. https://doi.org/10.1063/1.1291730 (In English)

Glass, E. N., Krisch, J. P. (1998) Radiation and string atmosphere for relativistic stars. *Physical Review D*, 57 (10), article R5945. https://doi.org/10.1103/PhysRevD.57.R5945 (In English)

Glass, E. N., Krisch, J. P. (1999) Two-fluid atmosphere for relativistic stars. *Classical and Quantum Gravity*, 16 (4), 1175–1184. https://doi.org/10.1088/0264-9381/16/4/007 (In English)

Hayward, S. A. (2006) Formation and evaporation of nonsingular black holes. *Physical Review Letters*, 96 (3), article 031103. https://doi.org/10.1103/PhysRevLett.96.031103 (In English)

Heydarzade, Y., Darabi, F. (2018a) Surrounded Bonnor-Vaidya solution by cosmological fields. *The European Physical Journal C*, 78, article 1004. https://doi.org/10.1140/epjc/s10052-018-6465-x (In English)

Heydarzade, Y., Darabi, F. (2018b) Surrounded Vaidya black holes: Apparent horizon properties. *The European Physical Journal C*, 78, article 342. https://doi.org/10.1140/epjc/s10052-018-5842-9 (In English)

Heydarzade, Y., Darabi, F. (2018c) Surrounded Vaidya solution by cosmological fields. *The European Physical Journal C*, 78, article 582. https://doi.org/10.1140/epjc/s10052-018-6041-4 (In English)

Heydarzade, Y., Vertogradov, V. (2024) Dynamical photon spheres in charged black holes and naked singularities. *The European Physical Journal C*, 84 (6), 582. https://doi.org/10.1140/epjc/s10052-024-12945-w (In English)

Husain, V. (1996) Exact solutions for null fluid collapse. *Physical Review D*, 53 (4), article R1759. https://doi.org/10.1103/PhysRevD.53.R1759 (In English)

Ibohal, N., Kapil, L. (2010) Charged black holes in Vaidya backgrounds: Hawking's Radiation. *International Journal of Modern Physics D*, 19 (04), 437–464. https://doi.org/10.1142/S0218271810016518 (In English)

Koga, Y., Asaka, N., Kimura, M., Okabayashi, K. (2022) Dynamical photon sphere and time evolving shadow around black holes with temporal accretion. *Physical Review D*, 105 (10), article 104040. https://doi.org/10.1103/PhysRevD.105.104040 (In English)

Koh, S., Park, M., Sherif, A. M. (2024) Thermodynamics with conformal Killing vector in the charged Vaidya metric. *Journal of High Energy Physics*, 2024 (2), article 28. https://doi.org/10.1007/JHEP02(2024)028 (In English)

Lake, K., Zannias, T. (1991) Structure of singularities in the spherical gravitational collapse of a charged null fluid. *Physical Review D*, 43(6), article 1798. https://doi.org/10.1103/PhysRevD.43.1798 (In English)

Mishra, A. K., Chakraborty, S., Sarkar, S. (2019) Understanding photon sphere and black hole shadow in dynamically evolving spacetimes. *Physical Review D*, 99 (10), article 104080. https://doi.org/10.1103/PhysRevD.99.104080 (In English)

Nielsen, A. B. (2014). Revisiting vaidya horizons. *Galaxies*, 2 (1), 62–71. https://doi.org/10.3390/galaxies2010062 (In English)
Nielsen, A. B., Yoon, J. H. (2008) Dynamical surface gravity. *Classical and Quantum Gravity*, 25 (8), article 085010. https://doi.org/10.1088/0264-9381/25/8/085010 (In English)
Ojako, S., Goswami, R., Maharaj, S. D., Narain, R. (2020) Conformal symmetries in generalised Vaidya spacetimes. *Classical and Quantum Gravity*, 37 (5), article 055005. https://doi.org/10.1088/1361-6382/ab5e2d (In English)
Ovalle, J., Casadio, R., Contreras, E., Sotomayor, A. (2021) Hairy black holes by gravitational decoupling. *Physics of the Dark Universe*, 31, article 100744. https://doi.org/10.1016/j.dark.2020.100744 (In English)
Patil, K. D., Saraykar, R. V., Ghate, S. H. (1999) Strong curvature naked singularities in generalized Vaidya space-times. *Pramana*, 52, 553–559. https://doi.org/10.1007/BF02829863 (In English)
Perlick, V., Tsupko, O. Y. (2022) Calculating black hole shadows: Review of analytical studies. *Physics Reports*, 947, 1–39. https://doi.org/10.1016/j.physrep.2021.10.004 (In English)
Perlick, V., Tsupko, O. Y., Bisnovatyi-Kogan, G. S. (2015) Influence of a plasma on the shadow of a spherically symmetric black hole. *Physical Review D*, 92 (10), article 104031. https://doi.org/10.1103/PhysRevD.92.104031 (In English)
Santos, N. O. (1985) Non-adiabatic radiating collapse. *Monthly Notices of the Royal Astronomical Society*, 216 (2), 403–410. https://doi.org/10.1093/mnras/216.2.403 (In English)
Solanki, J., Perlick, V. (2022) Photon sphere and shadow of a time-dependent black hole described by a Vaidya metric. *Physical Review D*, 105 (6), article 064056. https://doi.org/10.1103/PhysRevD.105.064056 (In English)
Synge, J. L. (1966) The escape of photons from gravitationally intense stars. *Monthly Notices of the Royal Astronomical Society*, 131 (3), 463–466. https://doi.org/10.1093/mnras/131.3.463 (In English)
Tsupko, O. Y., Bisnovatyi-Kogan, G. S. (2020) First analytical calculation of black hole shadow in McVittie metric. *International Journal of Modern Physics D*, 29 (09), article 2050062. https://doi.org/10.1142/S0218271820500625 (In English)
Tsupko, O. Y., Fan, Z., Bisnovatyi-Kogan, G. S. (2020) Black hole shadow as a standard ruler in cosmology. *Classical and Quantum Gravity*, 37 (6), article 065016. https://doi.org/10.1088/1361-6382/ab6f7d (In English)
Vagnozzi, S., Bambi, C., Visinelli, L. (2020) Concerns regarding the use of black hole shadows as standard rulers. *Classical and Quantum Gravity*, 37 (8), article 087001. https://doi.org/10.1088/1361-6382/ab7965 (In English)
Vagnozzi, S., Roy, R., Tsai, Y. D. et al. (2023) Horizon-scale tests of gravity theories and fundamental physics from the Event Horizon Telescope image of Sagittarius A. *Classical and Quantum Gravity*, 40 (16), article 165007. https://doi.org/10.1088/1361-6382/acd97b (In English)
Vaidya, P. C. (1951). Nonstatic solutions of Einstein's field equations for spheres of fluids radiating energy. *Physical Review*, 83 (1), 10–17. https://doi.org/10.1103/PhysRev.83.10 (In English)
Vertogradov, V. (2022) The structure of the generalized Vaidya space–time containing the eternal naked singularity. *International Journal of Modern Physics A*, 37 (28n29), article 2250185. https://doi.org/10.1142/S0217751X22501858 (In English)
Vertogradov, V. (2023) Extraction energy from charged Vaidya black hole via the Penrose process. *Communications in Theoretical Physics*, 75 (4), article 045404. https://doi.org/10.1088/1572-9494/acc018 (In English)
Vertogradov, V. (2024) The generalized Vaidya spacetime with polytropic equation of state. *General Relativity and Gravitation*, 56 (5), article 59. https://doi.org/10.1007/s10714-024-03244-6 (In English)
Vertogradov, V., Kudryavcev, D. (2023) Generalized Vaidya spacetime: Horizons, conformal symmetries, surface gravity and diagonalization. *Modern Physics Letters A*, 38 (24n25), article 2350119. https://doi.org/10.1142/S0217732323501195 (In English)
Vertogradov, V., Övgün, A. (2024a) Analyzing the influence of geometrical deformation on photon sphere and shadow radius: A new analytical approach—Spherically symmetric spacetimes. *Physics of the Dark Universe*, 45, article 101541. https://doi.org/10.1016/j.dark.2024.101541 (In English)
Vertogradov, V., Övgün, A. (2024b) General approach on shadow radius and photon spheres in asymptotically flat spacetimes and the impact of mass-dependent variations. *Physics Letters B*, 854, article 138758. https://doi.org/10.1016/j.physletb.2024.138758 (In English)
Vertogradov, V., Övgün, A., Pantig, R. C. (2024) Analyzing the influence of geometrical deformation on photon sphere and shadow radius: A new analytical approach-stationary, and axisymmetric spacetime. *arXiv*, 2405, article 05077. https://doi.org/10.48550/arXiv.2405.05077 (In English)
Wang, A., Wu, Y. (1999) Letter: Generalized vaidya solutions. *General Relativity and Gravitation*, 31, 107–114. https://doi.org/10.1023/A:1018819521971 (In English)

Summaries in Russian / Информация о статьях на русском языке

Физика конденсированного состояния

ИССЛЕДОВАНИЕ СТОЙКОСТИ ПОКРЫТИЙ ПОРОШКА СТАЛИ К АТМОСФЕРНОЙ КОРРОЗИИ

Иван Викторович Шакиров, Антон Сергеевич Жуков, Виталий Вячеславович Бобырь, Павел Алексеевич Кузнецов

Аннотация. Существует проблема хранения основного материала в условиях применения технологий лазерного синтеза — металлопорошковых композиций сталей и сплавов, которые обладают низкой коррозионной стойкостью. Данное исследование направлено на изучение устойчивости покрытий, нанесенных методом химико-термической обработки (ХТО) на поверхность порошка стали, которая обладает низкой стойкостью к атмосферной коррозии. Проведены длительные испытания порошковых проб с различным составом покрытий в условиях естественной атмосферной влажности и температуры окружающей среды Северо-Западного федерального округа РФ в течение двух лет. Оценивался химический состав образцов до и после испытания. Определение химического состава и морфологии частиц производилось методом рентгеноструктурного микроанализа (РСМА) с использование растрового электронного микроскопа (РЭМ). Показано, что покрытия, нанесенные методом ХТО, не создают сплошной защиты и ускоряют коррозионные процессы по сравнению с термообработанным порошком исходной стали.

Ключевые слова: аддитивные технологии, селективное лазерное сплавление, прямое лазерное выращивание, металлопорошковые композиции, защита от коррозии, химико-термическая обработка, йодотранспортный метод

Для цитирования: Shakirov, I. V., Zhukov, A. S., Bobyr', V. V., Kuznetsov, P. A. (2024) Research of the protective ability of coatings on steel powder against atmospheric corrosion. *Physics of Complex Systems*, 5 (3), 111–123. https://www.doi.org/10.33910/2687-153X-2024-5-3-111-123 EDN JDEKGG

ВЛИЯНИЕ ИОНИЗИРУЮЩЕГО ОБЛУЧЕНИЯ И ВРЕМЕНИ ТРАВЛЕНИЯ НА НИЗКОТЕМПЕРАТУРНУЮ РЕЛАКСАЦИЮ В ПОЛИВИНИЛИДЕНФТОРИДЕ

Елена Алексеевна Волгина, Дмитрий Эдуардович Темнов, Ульяна Владимировна Пинаева

Аннотация. В рамках настоящего исследования изучено релаксационное поведение полукристаллического полимера поливинилиденфторида (ПВДФ) с использованием метода термостимулированной деполяризации (ТСД). Экспериментальные измерения были выполнены на тонких пленках ПВДФ, подвергнутых облучению тяжелыми ионами Ne^{4+}, Xe^{26+} и Bi^{52+} с энергиями около 1,2 МэВ/нуклон для Ne^{4+} и Xe^{26+} и примерно 3,1 МэВ/нуклон для Bi^{52+}. Анализ полученных спектров ТСД выявил наличие трех основных релаксационных процессов при температурах около –45 °C, 20 °C и 40 °C. Установлено, что последующее химическое травление пленок приводит к возникновению нового релаксационного процесса при температуре около –10 °C, что может быть связано с появлением релаксаторов нового типа на поверхности треков.

Ключевые слова: поливинилиденфторид, термоактивационная спектроскопия, термостимулированная деполяризация, трековые мембраны, быстрые тяжелые ионы

Для цитирования: Volgina, E. A., Temnov, D. E., Pinaeva, U. V. (2024) The effect of ionizing radiation and etching time on low-temperature relaxation in polyvinylidene fluoride. *Physics of Complex Systems*, 5 (3), 124–128. https://www.doi.org/10.33910/2687-153X-2024-5-3-124-128 EDN LZFLTK

РАСПАД МЕТАСТАБИЛЬНЫХ АТОМОВ В ПОСЛЕСВЕЧЕНИИ ОДНОЭЛЕКТРОДНОГО ПРОБОЯ

Владислав Витальевич Залетов, Александр Игоревич Шишпанов, Юрий Зиновьевич Ионих

Аннотация. Проведены экспериментальные исследования волн ионизации, которые предваряют пробой в длинных разрядных трубках в неоне при низком давлении. Волны ионизации возникали при подаче прямоугольных импульсов напряжения на высоковольтный электрод разрядной трубки. Измерены концентрации атомов неона на метастабильном уровне $1s_5(^3P_2)$,

возникших после прохождения волны ионизации и окончания пробоя. Определены характерные времена распада этих состояний и элементарные процессы, ответственные за гибель метастабильных атомов в наиболее значительной степени.

Ключевые слова: газовый разряд, пробой, волна ионизации, плазма, послесвечение, неон, метастабильные атомы, элементарные процессы

Для цитирования: Zaletov, V. V., Shishpanov, A. I., Ionikh, Yu. Z. (2024) Decay of metastable atoms in the afterglow of single-electrode breakdown. *Physics of Complex Systems*, 5 (3), 129–134. https://www.doi.org/10.33910/2687-153X-2024-5-3-129-134 EDN JQUJTT

Теоретическая физика

КВАЗИЭНЕРГИЯ ХАОТИЧЕСКИХ СОСТОЯНИЙ В ЗАДАЧАХ НЕЛИНЕЙНОЙ ДИНАМИКИ. ВЫРОЖДЕНИЕ СОСТОЯНИЙ, ОБУСЛОВЛЕННОЕ СИММЕТРИЕЙ СИСТЕМЫ

Александр Викторович Ляпцев

Аннотация. Рассматриваются хаотические состояния в системе связанных осцилляторов Дуффинга. Вводится понятие «квазиэнергия системы», аналогичное понятию «квазиэнергия квантовомеханической системы», находящейся под воздействием внешнего периодического поля. Показано, что в отсутствии связи между осцилляторами в рассматриваемой системе при изменении внешнего воздействия реализуются хаотические состояния с одним значением квазиэнергии, но разными значениями момента импульса. Этот факт можно интерпретировать как существование вырожденных хаотических состояний системы. Численный эксперимент показывает, что учет взаимодействия между осцилляторами приводит к расщеплению квазиэнергии, аналогичному расщеплению уровня квазиэнергии в квантовомеханической системе.

Ключевые слова: нелинейная динамика, хаотические состояния, квазиэнергия, вырожденные состояния, численный эксперимент

Для цитирования: Liaptsev, A. V. (2024) Quasienergy of chaotic states in problems of nonlinear dynamics. Degeneration of states due to the symmetry of the system. *Physics of Complex Systems*, 5 (3), 135–145. https://www.doi.org/10.33910/2687-153X-2024-5-3-135-145 EDN FNIIBG

ИНФОРМАЦИЯ О СЛОЖНЫХ ФИЗИЧЕСКИХ СИСТЕМАХ: ПЛОСКОСТЬ ВЗАИМОДЕЙСТВУЮЩИХ АМПЛИТУД КОЛМОГОРОВСКОЙ СЛОЖНОСТИ

Драгутин Михайлович, Виджей Сингх

Аннотация. Одна из основных трудностей при изучении сложных физических систем заключается в определении вклада сложностей отдельных компонентов в сложность системы в целом. В целях изучения данной проблемы на основе колмогоровской сложности нами предложена плоскость колмогоровской сложности. В ходе настоящего исследования плоскость колмогоровской сложности и колмогоровская сложность были применены в отношении ежедневных (измеренных) и ежемесячных (воспроизведенных при помощи климатической модели) показателей осадков, образующих сложную физическую систему, а также в отношении температуры и давления водяного пара, выступающих в роли отдельных компонентов системы. На основе плоскости колмогоровской сложности были определены интервалы взаимодействующих амплитуд, в которых наблюдались вклады сложностей компонентов в общую сложность системы.

Ключевые слова: сложные физические системы, колмогоровская сложность, спектр колмогоровской сложности, плоскость колмогоровской сложности, общая сложность, сложность компонентов

Для цитирования: Mihailović, D. T., Singh, V. P. (2024) Information in complex physical systems: Kolmogorov complexity plane of interacting amplitudes. *Physics of Complex Systems*, 5 (3), 146–153. https://www.doi.org/10.33910/2687-153X-2024-5-3-146-153 EDN WTEGLX

ТЕНЬ ЧЕРНОЙ ДЫРЫ: ЭКСПЕРИМЕНТАЛЬНАЯ ПРОВЕРКА РАЗЛИЧНЫХ МОДЕЛЕЙ И ТЕНИ ЧЕРНОЙ ДЫРЫ ХЕЙВОРДА

Виталий Дмитриевич Вертоградов, Алина Вячеславовна Шакун, Марк Алексеевич Захаров

Аннотация. Недавние наблюдения теней черных дыр привнесли революционный взгляд на нашу способность исследовать гравитацию в экстремальных средах. В данной работе представлена

новая аналитическая модель тени динамической черной дыры Хейворда. В статье показано, что при некотором выборе массы и регуляризационных функций это пространство-время допускает гомотетический вектор Киллинга, что позволяет свести дифференциальные уравнения движения второго порядка к уравнениям первого порядка. После этого вводится преобразование координат к конформно-статическим координатам и новая сохраняемая величина вдоль нулевых геодезических. По результатам решений сделаны выводы, что в динамическом случае параметр регуляризации всегда уменьшает радиус фотонной сферы. На основе экспериментальных данных, полученных коллаборацией *The Event Horizon Telescope Collaboration*, сравнены полученные изображения Стрельца A^* с тенью черной дыры Рейсснера — Нордстрема, Бардина и Хейворда соответственно.

Ключевые слова: черная дыра, фотонная сфера, зависимость от массы, тень, динамическая черная дыра Хейворда

Для цитирования: Vertogradov, V. D., Shakun, A. V., Zakharov, M. A. (2024) Black hole shadow: Experimental test of different models and shadow of dynamical Hayward black hole. *Physics of Complex Systems*, 5 (3), 154–166. https://www.doi.org/10.33910/2687-153X-2024-5-3-154-166 EDN WWBQPT